

Experimental Investigations on Longitudinal Dispersive Mixing in Heterogeneous Aquifers

Von der Fakultät Bau- und Umweltingenieurwissenschaften der Universität Stuttgart zur
Erlangung der Würde eines Doktors der Ingenieurwissenschaften (Dr.-Ing.) genehmigte
Abhandlung

Vorgelegt von
Surabhin Chackiath Jose
aus Indien

Hauptberichter: Prof. Dr.-Ing. Rainer Helmig
Mitberichter: PD. Dr.-Ing. Olaf A. Cirpka
Prof. Dr. Peter Grathwohl

Tag der mündlichen Prüfung: 20. Oktober 2004

Institut für Wasserbau der Universität Stuttgart

2005

D93 Experimental Investigations on Longitudinal Dispersive Mixing in Heterogeneous Aquifers

Titelaufnahme der Deutschen Bibliothek

Jose, Surabhin Chackiath:

Experimental Investigations on Longitudinal Dispersive Mixing in Heterogeneous Aquifers / von Surabhin Chackiath Jose. Institut für Wasserbau, Universität Stuttgart. – Stuttgart: Inst. für Wasserbau, 2005

(Mitteilungen / Institut für Wasserbau, Universität Stuttgart; H. 136)
Zugl.: Stuttgart, Univ., Diss., 2005
ISBN 3-9337 61-39-5

Gegen Vervielfältigung und Übersetzung bestehen keine Einwände, es wird lediglich um Quellengabe gebeten.

Herausgegeben 2005 vom Eigenverlag des Instituts für Wasserbau
Druck: Sprint-Druck, Stuttgart

ACKNOWLEDGMENTS

This doctoral thesis is not just the result of my disciplined and consistent hard work, but an evidence of generous and unlimited support of many. It is a very difficult task to name each and every person who has helped me during my research years. But there are a few who deserve special attention.

First of all I thank *Deutsche Forschungsgemeinschaft (DFG)*, which funded this research by the *Emmy Noether program* under the grants *Ci 26/3-2 to Ci 26/3-4*. I am extremely grateful to the competent guidance of PD. Dr.-Ing. Olaf A. Cirpka for teaching me the first lessons of conducting research on an international level. I sincerely acknowledge the extra efforts taken by Prof. Dr.-Ing. Rainer Helmig and Prof. Dr. Peter Grathwohl for sincerely investing their time to assist and support me in my research.

It would have been difficult, if not impossible, for me to complete this experimental research without the sincere assistance I received from the mechanical workshop team led by Jürgen Laich and Henning Eickhoff; the constant support I experienced from Hubert Hermes with regard to the fluorometers; the immense help received from Oliver Trötschler, Thomas Haslwimmer and Johannes Schnieders; kind gestures of Gaby and Tanja from the chemistry lab; the sincere support received from Wolfgang Rempp, Steffen Hägele, and Gerhard Schmid. I am thankful to the constructive criticism I have enjoyed from my working group members, Wolfgang, Arif, Waltraud and Qingsong, who have enabled me to improve the research and its presentation. Also my sincere thanks to Arshad, Khawar, Jackelyn, Sachin, Kamal, and Johir, who were my hiwis and provided a very trustworthy assistance. I thankfully remember *BASF AG, Ludwigshafen*, who provided, free of cost, the complete amount of nonionic surfactant used in this research.

No words could express my gratitude to my parents, and my brother and his family, who have been consistently supporting me with their well wishes and prayers. I extend my sincere thanks to Dr. George Francis and family, who gave me valuable guidance, and filled the gap of a responsible guardian in Germany. I sincerely appreciate and thank Vineet Kapoor and family for their immense help and constructive discussions. I whole-heartedly thank George Jacoub, my long-time friend, who always provided me a helping hand, without hesitation, at hours of need.

ABSTRACT

Reactive mixing of compounds in porous media is a topic of current research interest because accurate estimation of reaction rates are crucial in planning aquifer remediation methods. It is suggested that relative parameters for dilution are better quantities to estimate reaction rates than the generally used classical macrodispersion coefficients. Most of the concepts developed in the field of reactive mixing are based on theoretical and numerical studies, and have not been experimentally tested. In this thesis, reactive mixing experiments are carried out in two different setups and the applicability of some of the existing numerical and theoretical studies to the observed data is tested. Two types of experimental setups - a homogeneously packed one-dimensional column setup and a heterogeneously packed two-dimensional sandbox setup - are used in the study. The column is 2m long with an inner diameter of 10cm, while the sandbox has dimensions 14m×0.5m×0.13m. Silica sand is used to fill both setups. The heterogeneity in the sandbox resembles the sedimentation pattern in nature. A conservative test and a reactive test each is conducted in both setups. Fluorescein is used as both the conservative and the reactive tracer.

Dilution coefficients are estimated from the temporal moments of the conservative breakthrough curves obtained within in the porous media. Fiber optic fluorometry is used as the point measurement system. The measurement tip of the optic fiber probes has a diameter of 2.5mm. Reactive mixing in the porous media is predicted from the dilution coefficients estimated from the conservative tests, and is compared with the actual reactive mixing from the reactive tests.

I conclude that point-like measurements provide reliable information of dilution and mixing in porous media, and therefore are effective enough in predicting product formation, provided sorption parameters are effectively quantified. I found that regions with large contrast in hydraulic conductivity give opportunity to enhanced mixing. Considering the typical length scales of the heterogeneities, the experimental findings are qualitatively in agreement with the linear stochastic theory.

ZUSAMMENFASSUNG

Hintergrund und Motivation

Die Durchmischung miteinander reagierender gelöster Stoffe in porösen Medien ist ein wichtiges Thema der gegenwärtigen Grundwasserforschung (*Molz und Widdowson, 1988; Kitanidis, 1994; Kapoor and Kitanidis, 1998; Oya and Valocchi, 1998; Cirpka and Kitanidis, 2000a, 2000b, Cirpka, 2002*). Es ist notwendig, die Durchmischung reaktiver Substanzen möglichst genau vorherzusagen, um Verfahren zur Sanierung kontaminierter Grundwasserleiter auslegen zu können. Dies betrifft insbesondere die aktive biotechnische in-situ Sanierung und die Bewertung des natürlichen Abbaus, weil hier die mangelnde Durchmischung der beteiligten Stoffe den limitierenden Faktor darstellen kann.

Bis in die frühen 90-er Jahre wurde der klassische Makrodispersionskoeffizient D_{mac} in Simulationsmodellen zum reaktiven Transport als Parameter für die Durchmischung verwendet. Der Prozess der Makrodispersion umfasst sowohl die Spreitung der Stoffwolke, das heißt die zunehmende Unregelmäßigkeit ihrer Form, als auch die Verdünnung der in der Wolke enthaltenen Stoffe. In Berechnungen, die D_{mac} als Durchmischungskoeffizient für heterogene Grundwasserleiter verwendeten, wurden die Reaktionsraten überschätzt (*Molz und Widdowson, 1988; Ginn et al., 1995; Miralles-Wilhelm et al., 1997; Cirpka et al., 1999*). In der Praxis würde dies zu einer unvollständigen Sanierung kontaminierter Standorte führen, da die Zeit für die Sanierung unterschätzt wird. Es lässt sich zeigen, dass in Abwesenheit von Phasenübergangsprozessen die Verdünnung der Stoffe die eigentliche Ursache der Durchmischung darstellt, und dass die Verdünnung durch den lokalen Dispersionskoeffizienten der Porenskala parametrisiert werden kann. Die räumliche Variabilität der Grundwasserleiter verstärkt die Verdünnung der Stoffwolken.

Kitanidis (1994) veranschaulichte die Verdünnung durch die Abnahme der Maximalkonzentration und führte einen Verdünnungsindex ein, der die Zunahme des effektiven Volumens beschreibt, den die Masse des gelösten Stoffes einnimmt. Da die Verdünnung der Prozess ist, der zur Durchmischung führt, waren *Kitanidis (1994)* und *Kapoor et al. (1997)* der Meinung, dass Parameter, die die Verdünnung beschreiben, eine bessere Schätzung der Durchmischung ergeben als Makrodispersionskoeffizienten, die kumulativ die Verdünnung und Spreitung der Fahne beschreiben.

Cirpka und Kitanidis, (2000a) führten numerische Studien durch, in denen Koeffizienten der Durchmischung und Verdünnung aus punktiert gemessenen

Durchbruchskurven eines konservativen Tracers abgeleitet wurden. Hierzu verwendeten sie die Methode der zeitlichen Momente. Die numerischen Studien von *Cirpka und Kitanidis (2000b)* ergaben, dass der sogenannte effektive Dispersionskoeffizient, d.h. der in einem Querschnitt gemittelte Wert des lokal geschätzten Verdünnungskoeffizientens, die Durchmischung reaktiver Stoffe viel genauer beschreibt als der klassische Makrodispersionskoeffizient. *Cirpka (2002)* zeigte, dass die stochastisch-analytischen Lösungen von *Dentz et al. (2000a)* und *Fiori und Dagan (2000)* für den effektiven Längsdispersionkoeffizienten für eine punkthafte Stoffeinleitung verwendet werden können, um die reaktive Durchmischung gelöster Stoffe in statistisch stationären Strömungsfeldern zu parametrisieren.

Neben den aufgeführten Untersuchungen wurden von anderen Arbeitsgruppen weitere theoretische und numerische Studien durchgeführt.

Ziele und Aufgabenstellung

Das Hauptziel der Arbeit besteht darin, die theoretisch-numerischen Ansätze von *Cirpka und Kitanidis (2000a)* experimentell zu überprüfen. Die Untersuchungen wurden in einem heterogen gefüllten Grundwasserversuchsstand durchgeführt, der Sedimentationsmuster aufweist, wie sie auch in natürlichen Sedimenten auftreten. Ich verwendete die experimentellen Daten, um die Anwendbarkeit der genannten theoretischen Konzepte auf reale Systeme mit natürlichem Sedimentationsmuster zu überprüfen. Meine Arbeit soll folgende Fragen beantworten:

- Liefern punktförmige Konzentrationsmessungen zuverlässige Aussagen zu Verdünnung und Durchmischung?
- Können (semi)-analytische stochastische Ergebnisse zur effektiven Dispersion und Durchmischung auf reale Daten angewendet werden?

Die Studie beschränkt sich auf Fälle, in denen die makroskopische Durchmischung in Längsrichtung erfolgt. Um diese Ziele zu erreichen, mussten folgende Teilaufgaben bearbeitet werden:

- Entwicklung eines Systems zur punkthafte Messung von Konzentrationen,
- Auswahl passender konservativer und reaktiver Tracer,
- Versuche zur reaktiven Durchmischung in einer homogen gefüllten Säule,
- Experimente in einem heterogen gefüllten Grundwasserversuchsstand,
- Interpretation der Ergebnisse und Vergleich mit theoretischen Ansätzen.

Übersicht über die Dissertationsschrift

- *Kapitel 1* beschreibt den Hintergrund und die Motivation der Arbeit und legt die Ziele und Aufgaben fest.
- *Kapitel 2* liefert den theoretischen Hintergrund, der für das Grundverständnis der untersuchten Prozesse unerlässlich ist.
- *Kapitel 3* enthält eine Zusammenfassung aller für diese Studie relevanten und/oder vergleichbaren veröffentlichten Laborversuche.
- *Kapitel 4* enthält einen Überblick der in den Versuchen eingesetzten Materialien und Methoden.
 - Für die *punktartige in-situ Messung der Konzentration* verwendete ich die am Institut für Wasserbau entwickelte Lichtleiterfluorometrie. Die wichtigste Anpassung der vorhandenen faseroptischen Messtechnik bestand darin, den Messdurchmesser der ursprünglichen faseroptischen Sonde von 4.4mm auf 2.5mm zu reduzieren. Das verringerte Messvolumen erlaubt es, die gemessene Fluoreszenzintensität als Punktwert zu interpretieren.
 - Als *konservativen* und *reaktiver Tracer* verwendete ich Fluorescein (Uranin), das für Experimente in Quarzsanden häufig als konservative Tracer eingesetzt wird (*Smart and Laidlaw, 1977; Kasnavia et al., 1999*). Die Fluoreszenzintensität von Fluorescein hängt vom pH ab, mit maximalen Werten im alkalischen Bereich und minimalen Werten im sauren. Diese Eigenschaft war ausschlaggebend, um Fluorescein als reaktiven Tracer einsetzen zu können. Fluorescein wurde als reaktiver Tracer in Turbulenzuntersuchungen eingesetzt (*Koochesfahani und Dimotakis, 1986*). In der vorliegenden Arbeit wurde das System erstmals in porösen Medien eingesetzt. Um die Sorption von Fluorescein an Quarz bei niedrigem pH zu unterbinden, wurde den Lösungen das von der BASF hergestellte nicht-ionische Tensid Lutensol GD70 beigelegt. Zur Gewährleistung der Vergleichbarkeit wurde das Tensid sowohl in den konservativen als auch in den reaktiven Tests eingesetzt.
 - Die *eindimensionalen Versuche* wurden in einer zwei Meter langen PVC Säule mit einem Innendurchmesser von 10cm und einer Füllung mit Grobsand (Durchmesser 1-2.5mm) durchgeführt. Der *zweidimensionale Grundwasser-versuchsstand* hat eine Größe von 14m×0.5m×0.13m und ist *heterogen mit 4 Sandgemischen* gefüllt, die eine Korngröße zwischen 0mm und 3mm und

einen Durchlässigkeitsbeiwert zwischen $5.61 \times 10^{-4} \text{ m/s}$ und $1.67 \times 10^{-2} \text{ m/s}$ aufweisen. Die heterogene Füllung im Sandkasten weist naturähnliche Sedimentationsmuster auf, weil die Befüllung durch Sedimentation in stehendes Wasser erfolgte. Im Gegensatz hierzu wurden die in der Literatur aufgeführten Experimente üblicherweise mit Sandfüllungen durchgeführt, die eine fest definierte Struktur von in sich homogenen Blöcken aufwiesen. Die Säulenexperimente führte ich vor den Versuchen im zweidimensionalen, heterogen befüllten Grundwasserversuchsstand durch, um die Messtechnik und den Versuchsansatz zu überprüfen.

- *Kapitel 5* beschreibt die im Rahmen der Arbeit geführten Experimente und die Vorgehensweise für die Analyse der Messergebnisse.
- Je ein *konservativer* und ein *reaktiver Tracertest* wurden in der Säule und im Grundwasserversuchsstand unter konstanten Strömungsbedingungen durchgeführt. In den konservativen Tests verdrängt eine alkalische Tensidlösung mit Tracer eine alkalische Tensidlösung ohne Tracer, während in einem reaktiven Test eine alkalische Tensidlösung ohne Tracer eine saure Tensidlösung mit Tracer verdrängt. Um das Anwachsen von Bakterien zu verhindern, die das Tensid abbauen, wurde der alkalischen Tensidlösung 0.1 mmol/l Natriumazid (NaN_3) zugegeben.
 - In *Batchversuchen* ermittelte ich den pH-Wert als Funktion des Mischungsverhältnisses der eingesetzten Lösungen sowie die Beziehung zwischen dem pH-Wert und der relativen Fluoreszenzintensität. Diese Beziehungen verwendete ich, um aus den konservativen Tracerdaten das reaktive Durchbruchverhalten vorherzusagen.
 - Aus der mittleren Ankunftszeit und der Varianz der lokal ermittelten Durchbruchkurven errechnete ich *apparente effektive Dispersionskoeffizienten*, die die Verdünnung konservativer und Durchmischung reaktiver Stoffe parametrisieren. Ich verwendete diese Koeffizienten, um den durchmischungskontrollierten reaktiven Transport im selben porösen Medium vorherzusagen und verglich diese Prognosen mit den gemessenen Durchbruchkurven der reaktiven Tracertests. Die apparenten effektiven Dispersionskoeffizienten des zweidimensionalen Grundwasserversuchsstands wurden darüber hinaus mit den analytischen Lösungen der

linearen stochastischen Theorie verglichen, um die Anwendbarkeit dieser Ansätze zu überprüfen.

- *Kapitel 6* fasst die Ergebnisse der konservativen Tracertests in der homogenen Säule und dem heterogenen zweidimensionalen Versuchsstand zusammen. Aus den Messdaten leitete ich die Koeffizienten für die Verdünnung und Durchmischung ab. Die Messergebnisse des heterogen befüllten Grundwasserversuchsstands wurden qualitativ mit den Ergebnissen der numerischen Studie von *Cirpka und Kitanidis, (2000a)* verglichen. Eine modifizierte Version der von *Dentz et al., (2000a)* und *Fiori und Dagan, (2000)* abgeleiteten Spektrallösungen für die effektive Dispersion und die Makrodispersion wurde auf die Messdaten angewendet.
- *Kapitel 7* liefert einen Vergleich zwischen den tatsächlichen reaktiven Durchbruchkurven und den Kurven, die auf der Grundlage der konservativen Tests vorhergesagt wurden. Hier erörtere ich, wie gut die konservativen Daten verwendet werden können, um die reaktive Durchmischung vorauszusagen.
- *Kapitel 8* fasst die Befunde dieser Studie zusammen und liefert einen Ausblick für weitere Forschungsmöglichkeiten.

Ergebnisse und Schlussfolgerungen

- Die Ergebnisse der konservativen Tests im heterogenen Grundwasserversuchsstand zeigten eine gute qualitative Übereinstimmung mit den numerischen Studien von *Cirpka and Kitanidis, (2000a)*.
- Die Differenz zwischen dem klassischen Makrodispersionskoeffizienten D_{mac} und dem effektiven Dispersionskoeffizienten D_{eff} bei den konservativen Tests im Grundwasserversuchsstand begrenzte sich auf einen Faktor von etwa 1.5, was im Vergleich zu einigen theoretischen Studien nicht sehr groß ist (*Kitanidis, 1994; Dentz et al., 2000a*). Dies ergibt sich aus der geringen Mächtigkeit der eingebrachten Sandlinsen im Versuchsstand.
- Für die Praxis folgt hieraus, dass die dispersive Längsdurchmischung in Grundwasserleitern mit Sandlinsen vergleichbarer Dicke zwar signifikant unvollständig ist, aber bei weitem nicht so ausgeprägt wie für virtuelle, isotrope Grundwasser vorhergesagt.
- Im homogenen Säulenversuch lagen die lokal ermittelten apparenten Dispersionskoeffizienten zwischen 2mm und 13mm mit Medianen innerhalb einer Messebene von 3mm, was in etwa dem größten Korndurchmesser entspricht. Die an einzelnen Sonden

im heterogenen Grundwasserversuchsstand ermittelten apparenten lokalen Dispersionskoeffizienten lagen zwischen 5.5mm und 860mm.

- Zonen mit großen Unterschieden im Durchlässigkeitsbeiwert bewirkten eine verstärkte Durchmischung.
- Die Lösung erster Ordnung für die effektive Dispersion nach der linearen stochastischen Theorie (*Dentz et al., 2000a; Fiori and Dagan, 2000*) ließ sich an die Messdaten des konservativen Experiments im Grundwasserversuchsstand anpassen (siehe Abbildung 1). Die ermittelten Koeffizienten liegen im Bereich erwarteter Werte. Es verbleibt jedoch eine hohe Variabilität der Messdaten, die auf den kleinen Querschnitt des Versuchsstand zurückzuführen ist. Vor allem die ermittelte lokale Querdispersivität von 0.23mm liegt innerhalb der Bandbreite von Werten, die für die eingesetzten Sande in anderen Studien ermittelt wurde (*Cirpka et al., 2004*). *Hieraus schließe ich, dass die lineare stochastische Theorie für die effektive Dispersion grundsätzlich auf reale Daten anwendbar ist.*

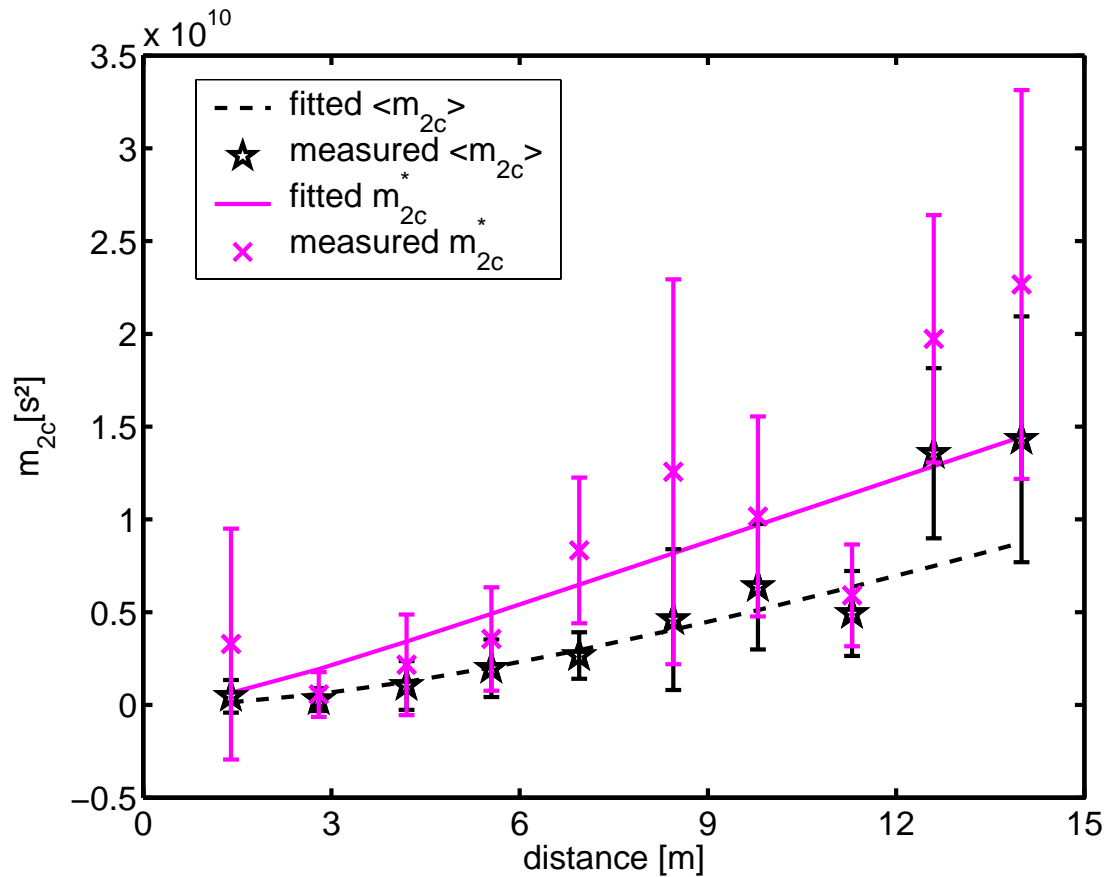


Abbildung 1 Zweite zeitliche Zentralmomente als Funktion des Fließweges. Vergleich zwischen gefitteten Ergebnissen aus der linearen stochastischen Theorie und gemessenen Daten. Durchgezogene Linie: gefittete $m_{2c}^*(x_1)$; gepunktete Linie: gefittete $\langle m_{2c}(\mathbf{x}) \rangle$; Kreuze: gemessene $m_{2c}^*(x_1)$; Sterne: gemessene $\langle m_{2c}(\mathbf{x}) \rangle$.

- Die reaktive Durchmischung kann in der homogenen Bodensäule für kleine Entfernungen unter Verwendung der konservativen Daten gut vorhergesagt werden. Bei größeren Fließstrecken zeigt sich eine klare Tendenz zur Überschätzung der gesamten Produktmasse. Ein Modell der reaktiven Durchmischung, das die lineare Retardation beider Fronten berücksichtigt, kann die reaktiven Durchbruchkurven gut erklären (siehe Abbildung 2). *Unter Voraussetzung, dass Sorptionsparameter ausreichend genau quantifiziert werden, lässt sich die Durchmischung reaktiver Stoffe und die daraus folgenden Reaktionsraten gut aus den punktiert gemessenen Durchbruchkurven konservativer Tracer vorhersagen.*

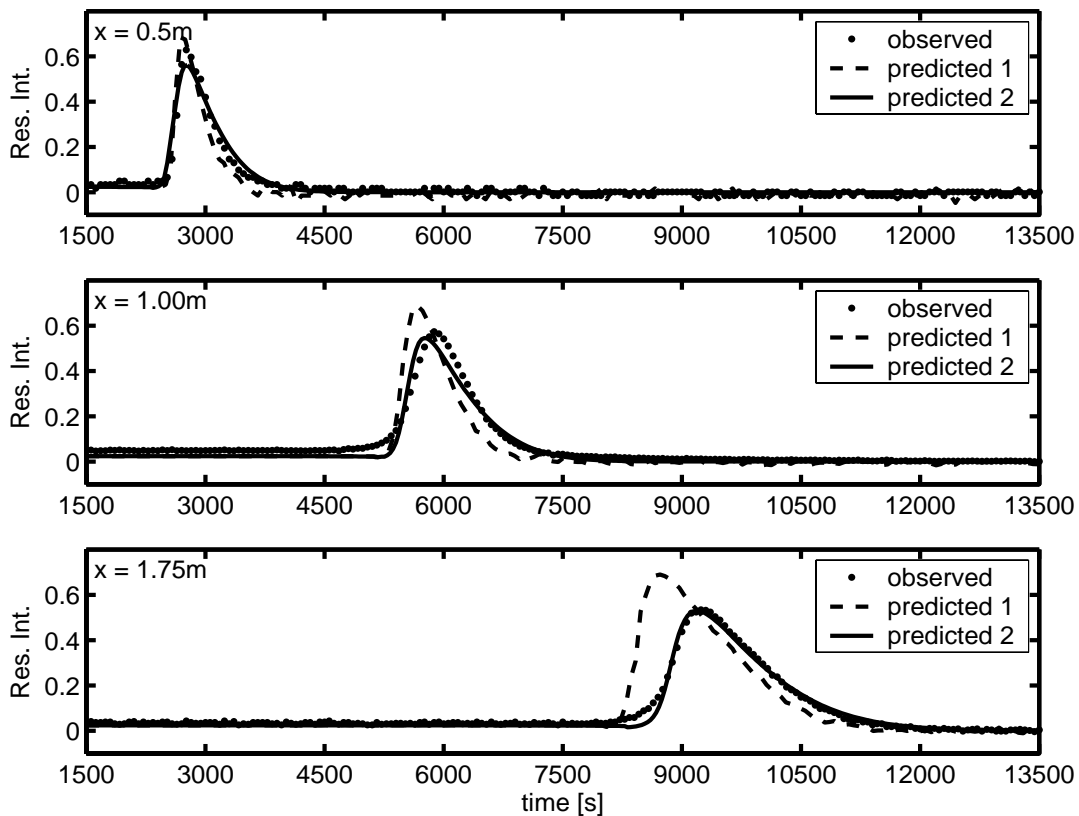


Abbildung 2 Resultierende Fluoreszenzintensität der beobachteten und der verschiedenen vorhergesagten reaktiven Durchbruchskurven für drei verschiedene Messpositionen in der Säule. ‚Predicted1‘ ist die Vorhersage ohne Berücksichtigung der Tracersorption und ‚Predicted2‘ unter Berücksichtigung linearer Tracersorption.

- Die beobachteten reaktiven Durchbruchskurven im großskaligen Grundwasser-versuchsstand weisen zum Teil höhere Konzentrationen auf als aus den konservativen Daten vorhergesagt; auch sind die Fronten zum Teil weiter. Die Abweichungen sind auf Sorptionseffekte zurückzuführen, die im großskaligen Experimente stärker wirken als in der Säule, weil die Aufenthaltszeiten größer sind, und weil zum Teil feinkörnigere Sande eingesetzt wurden.
- Wegen den unbekanntem chemischen Eigenschaften der in der Studie verwendeten nicht-ionischen Tenside ist es schwierig, wenn nicht unmöglich, die Prozesse, die das beobachtete Verhalten bestimmen, zu quantifizieren. Die genaue Zusammensetzung des Tensids ist ein Betriebsgeheimnis des Herstellers.

Bedeutung und neue Aspekte der Arbeit

- Ich konnte zeigen, dass einige theoretische Konzepte in Bezug auf die Durchmischung reaktiver Substanzen auf experimentelle Daten angewendet werden können.
- Fluorescein wurde zum ersten Mal bei Versuchen in porösen Medien als ein *reaktiver Tracer* verwendet.
- Nach bestem Wissen stellt die Studie die erste experimentelle Untersuchung zur reaktiven Durchmischung in Sandkörpern auf großem Skalen (2m und 14m) dar. Die bisher veröffentlichten reaktiven Tests hatten eine Länge von weniger als 40cm; und es wurden Glaskugeln statt Sand verwendet (*Raje and Kapoor, 2000; Gramling et al., 2002*).
- Die heterogene Füllung im Grundwasserversuchsstand wies ein naturähnliches Sedimentationsmuster auf anstelle von fest definierten, in sich homogenen Blöcken, wie sie in vergleichbaren Experimenten verwendet wurden.
- Die Messdaten der konservativen Tracertests im Grundwasserversuchsstand werden in der Doktorarbeit von Wolfgang Nowak verwendet, um die Verteilung der Durchlässigkeit im Versuchsstand mittels geostatistischer inverser Modellierung zu identifizieren (*Nowak, 2004*).
- Die Ergebnisse meiner Arbeit tragen zu einem besseren Verständnis bestehender theoretische Konzepte bei und identifizieren weitere Forschungsmöglichkeiten.

Aussicht

Die Untersuchungen zur reaktiven Durchmischung sowohl in der homogenen Bodensäule als auch im heterogen befüllten Grundwasserversuchsstand zeigen, dass bei längeren Fließdistanzen sogar schwache Sorption für die Durchmischung sehr wichtig ist. Dieser experimentelle Befund ist in vollem Einklang mit theoretischen Studien, die vorhersagen, dass Sorptionsunterschiede, ganz gleich wie schwach, im asymptotischen Limit die Längsdurchmischung von Stoffwolken dominieren (*Oya and Valocchi, 1998*). Die Ergebnisse weisen auf, wie schwierig die Vorhersage des reaktiven Transports in realen Fallsituationen sein kann. Weitere Forschung ist deshalb notwendig, um alle wesentlichen Prozesse, die bei den verschiedenen Typen der reaktiven Durchmischung eine Rolle spielen, systematisch zu quantifizieren.

Die verwendeten experimentellen Methoden sollten verbessert werden, um die Sorption der reaktiven Tracer vollständig zu unterbinden und dadurch zusätzliche Information zu den Ergebnissen dieser Studie zu gewinnen. Wie bereits erwähnt wurde, sind nur sehr wenige

theoretische und numerische Studien zur Durchmischung und Reaktion experimentell verifiziert oder auf ihrer Anwendbarkeit auf realen Daten überprüft worden. Es ist jedoch notwendig, dass die theoretischen Ergebnisse experimentell untermauert werden. Der Vergleich zwischen Theorie und Experimente dient der Verbesserung der vorhandenen Konzepte oder die Entwicklung neuer theoretischer Ansätze. Letztendlich trägt die systematische Forschung in diesem Bereich zur Entwicklung verbesserter Sanierungsstrategien bei.

TABLE OF CONTENTS

ACKNOWLEDGMENTS	i
ABSTRACT	iii
ZUSAMMENFASSUNG	v
Hintergrund und Motivation	v
Ziele und Aufgabenstellung	vi
Übersicht über die Dissertationsschrift	vii
Ergebnisse und Schlussfolgerungen	ix
Bedeutung und neue Aspekte der Arbeit	xiii
Aussicht	xiii
TABLE OF CONTENTS	xv
LIST OF FIGURES	xix
LIST OF TABLES	xxiii
LIST OF ABBREVIATIONS AND SYMBOLS	xxv
1 INTRODUCTION	1
1.1 Background and Motivation	1
1.2 Objectives	2
1.3 Tasks	2
1.4 General Framework of the Experiments	3
1.5 Thesis Structure	3
2 THEORETICAL BACKGROUND	5
2.1 Basic Concepts and Conservation Principles in Porous Media	5
2.1.1 Continuum hypothesis and REV	5
2.1.2 Flow in porous media	5
2.1.3 Solute transport in porous media	7
2.2 Scale Effects of Dispersion	10
2.2.1 Classification of dispersion	10
2.2.2 Characteristic times	12
2.2.3 Peclet numbers	13
2.3 Solute Transport Modeling	14
2.3.1 Deterministic models	14
2.3.2 Stochastic models	14
2.3.3 Statistical moments	15

2.4	Reactive Transport in Heterogeneous Porous Media	17
2.4.1	Chemical reactions in porous media	17
2.4.2	Retardation	18
2.4.3	Processes influencing mixing	19
2.4.4	Dispersion-controlled reactive mixing	20
2.5	Approaches in Quantifying Dilution	21
2.5.1	Quantifying mixing using macrodispersion	21
2.5.2	Other parameters to quantify mixing	22
2.5.3	Quantifying dilution using local temporal moments	26
2.6	System Considered in the Thesis	30
2.6.1	Conservative tracer test	30
2.6.2	Reactive tracer test	31
3	REVIEW OF LABORATORY TRACER TESTS TO DETERMINE SOLUTE TRANSPORT IN POROUS MEDIA	33
3.1	Laboratory Methods to Determine Flow and Transport Properties in Porous Media	33
3.2	Tracer Experiments in Homogeneous and Heterogeneous Porous Media	34
3.3	Experiments Comparable to the Undertaken Research	39
4	MATERIALS AND EXPERIMENTAL SETUPS	41
4.1	Point Measurement System	41
4.1.1	Fluorometer	41
4.1.2	Optic fiber	43
4.1.3	Data acquisition system	46
4.2	Tracer	46
4.2.1	Requirements	46
4.2.2	Selected tracer: fluorescein	46
4.2.3	Overcoming fluorescein sorption	50
4.2.4	Lutensol GD 70	56
4.2.5	General experimental framework	56
4.3	Experimental Setups	56
4.3.1	One-dimensional column setup	56
4.3.2	Sandbox setup	66
5	EXPERIMENT TYPES AND PROCESSING OF MEASURED DATA	72
5.1	Batch Tests	72

5.1.1	Fluorescence intensity and tracer concentration	72
5.1.2	Fluorescence intensity and solution pH	73
5.1.3	Solution pH and mixing ratio	75
5.2	Conservative Tracer Tests	78
5.2.1	Homogeneously packed porous medium (column)	78
5.2.2	Heterogeneously packed porous medium (sandbox)	82
5.3	Reactive Tracer Tests	86
5.3.1	Homogeneously packed column	86
5.3.2	Heterogeneously packed sandbox	88
6	CHARACTERIZATION OF DILUTION AND MIXING IN POROUS MEDIA	89
6.1	Homogeneous Porous Medium (Column Experiment)	89
6.1.1	First moments and apparent velocities	92
6.1.2	Second central moments and apparent dispersivities	94
6.1.3	Apparent parameters at the outflow boundary	99
6.2	Heterogeneous Porous Medium (Sandbox Experiment)	100
6.2.1	First moments and apparent velocities	100
6.2.2	Second central moments and apparent dispersivities	104
6.2.3	Apparent parameters at the outflow boundary	109
6.2.4	Comparison with results of linear stochastic theory	110
6.3	Conclusions	114
6.3.1	Homogeneous porous medium	114
6.3.2	Heterogeneous porous medium	115
7	PREDICTION OF MIXING-CONTROLLED REACTIVE TRANSPORT IN POROUS MEDIA FROM CONSERVATIVE TRACER TEST DATA	116
7.1	Methodology to Predict Reactive Mixing from Conservative Tracer Test Data	116
7.2	Reactive Tracer Test in the Homogeneously Packed Column	118
7.3	Reactive Tracer Test in the Heterogeneously-packed Sandbox	129
7.4	Concluding Remarks	134
8	FINAL REMARKS	136
8.1	Summary and Conclusions	136
8.2	Future Prospects	139
	REFERENCES	141
	Listed Firms/Institutes	150

LIST OF FIGURES

Fig 2.1	Classification of chemical reactions in porous media (Rubin, 1983)	18
Fig 2.2	Reactive mixing of compounds.....	20
Fig 2.3	Measuring plume concentrations at a control plane.....	21
Fig 2.4	Measuring plume concentrations at several points across a control plane	27
Fig 4.1	Sketch of fiber optic fluorometer (source: www.hermess.de)	42
Fig 4.2	Fluorometer	42
Fig 4.3	Duplex polymer optic fiber cable.....	43
Fig 4.4	Measurement volume of standard and modified duplex cables. Note that the modified duplex cable has large measurement volume.	44
Fig 4.5	Modification of duplex polymer cables to probes a) original duplex polymer optic fiber cable. b) cable insulation stripped for 6 cm. c) individual fibers joined by heat shrinkable tube. d) the joint between the cable insulation and shrunk tube closed by another heat shrinkable tube. e) one more heat shrinkable tube put on the top of the tube closing the joint between the insulation and shrunk tube.....	45
Fig 4.6	Structure of fluorescein (source: www.probes.com).....	47
Fig 4.7	Absorption and emission spectra of fluorescein in pH 9.0 buffer (www.probes.com).....	48
Fig 4.8	pH dependency of fluorescein intensity (for test solutions prepared in deionized water)	49
Fig 4.9	Fluorescein sorption at acidic pHs (The circles represent sand grains and the region between them denotes the fluid medium).	50
Fig 4.10	Sorption observed at pH2.....	52
Fig 4.11	Sorption isotherm at pH3	52
Fig 4.12	Non-ionic surfactants and tracer molecules in acid medium	53
Fig 4.13	Comparison – BTCs in Lutensol GD70 and in deionised water	55
Fig 4.14	One-dimensional PVC column.....	58
Fig 4.15	Arrangement of fiber optic probes at column cross-sections – Plan view.....	59
Fig 4.16	Design of the column ends	59
Fig 4.17	Design of the column caps	60
Fig 4.18	Grain-size distribution of the silica sand (Dorosilit Nr.5).....	61
Fig 4.19	Design of the filling-tube	62

Fig 4.20	Funnel used for column packing	62
Fig 4.21	Container for holding the sand	63
Fig 4.22	The complete set-up for column packing	64
Fig 4.23	The one-dimensional experimental setup	65
Fig 4.24	A general view of the sandbox (not to scale)	66
Fig 4.25	Inlet chamber of the sand box	67
Fig 4.26	Position of the piezometers and the probes at the domain of the sandbox.....	67
Fig 4.27	Outlet flow chamber of the model sandbox	68
Fig 4.28	A flow through cell	68
Fig 4.29	Hydraulic switchboard	69
Fig 4.30	Heterogeneous filling in the sandbox	70
Fig 4.31	Confining layer and cover of the box.....	71
Fig 5.1	Fluorescence intensity of fluorescein as function of tracer concentration	73
Fig 5.2	Relative fluorescence intensity as function of solution pH.....	74
Fig 5.3	Titration curve between pH4 surfactant solution and pH10 surfactant solution.....	75
Fig 5.4	Titration curves between pH3 surfactant solution and pH10 surfactant solution. ...	76
Fig 5.5	Measured and simulated titration curves between pH3 surfactant solution and pH10 surfactant solution.	77
Fig 5.6	General framework of the conservative and reactive tests.....	78
Fig 5.7	Column experiment setup.....	80
Fig 5.8	Sandbox experiment setup	83
Fig 6.1	Locally determined values and arithmetic mean of first temporal moments m_1	93
Fig 6.2	Probe-related apparent velocities $v_a(\mathbf{x})$, apparent effective velocity $v^e(x_1)$, and apparent macroscopic velocity $v^*(x_1)$ as function of travel distance.....	94
Fig 6.3	Locally determined second central temporal moments $m_{2c}(\mathbf{x})$, arithmetic mean within each measurement section $\langle m_{2c}(\mathbf{x}) \rangle$, and second central temporal moment of the cross-sectional averaged concentration $m_{2c}^*(x_1)$ as function of travel distance.	96
Fig 6.4	Locally determined apparent dispersion coefficient $D_a(\mathbf{x})$, apparent effective dispersion coefficient $D^e(x_1)$, and apparent macroscopic dispersion coefficient $D^*(x_1)$ as a function of travel distance.....	97

Fig 6.5	Locally determined apparent longitudinal dispersivity $\alpha_a(\mathbf{x})$, and apparent effective dispersivity $\alpha^e(x_1)$ as a function of distance.....	98
Fig 6.7	Normalized first temporal moments and the various apparent velocities at each measurement plane as a function of travel distance in the sandbox. (top) locally determined values and arithmetic mean of first moments m_1 . (bottom) probe-related apparent velocities $v_a(x)$, apparent effective velocity $v^e(x_1)$, and apparent macroscopic velocity $v^*(x_1)$ as function of travel distance.	103
Fig 6.8	Normalized second central temporal moments and the various apparent dispersion coefficients at each measurement plane as a function of travel distance in the sandbox. (top): locally determined values $m_{2c}(\mathbf{x})$, arithmetic mean within each measurement plane $\langle m_{2c}(\mathbf{x}) \rangle$ and second central moment of the cross-sectional averaged concentration $m_{2c}^*(x_1)$ as a function of travel distance, (bottom) locally determined values $D_a(\mathbf{x})$, apparent effective dispersion coefficient $D^e(x_1)$, apparent macrodispersion coefficient $D^*(x_1)$ as a function of travel distance.....	105
Fig 6.9	Distribution of apparent dispersivities in the sandbox. (top) two-dimensional distribution of apparent dispersivities in the sandbox. (bottom) locally determined apparent dispersivity α_a and apparent effective dispersivity α^e as a function of travel distance.....	107
Fig 6.10	Detailed distributions in the section between 10m and 14m. (top): apparent dispersion coefficients; (middle): travel time; (bottom): sedimentation pattern in the sandbox.	108
Fig 6.11	Second central moments as function of travel distance. Comparison between fitted results of linear stochastic theory and measured data. Solid line: fitted $m_{2c}^*(x_1)$; dashed line: fitted $\langle m_{2c}(\mathbf{x}) \rangle$; crosses: measured $m_{2c}^*(x_1)$; stars: measured $\langle m_{2c}(\mathbf{x}) \rangle$	114
Fig 7.1	Cross-section averaged zeroth temporal moments for the different measurement sections in the column. Prediction 1 denotes to prediction without considering tracer sorption, and prediction 2 corresponds to one considering linear sorption of tracer.	121
Fig 7.2	Resultant fluorescence intensity of the observed and the predicted (without considering tracer sorption) reactive breakthrough curves for three different measurement locations in the column.	122

Fig 7.3	Resultant fluorescence intensity of the observed and the various predicted reactive breakthrough curves for three different measurement locations in the column. ‘predicted 1’ corresponds to the prediction without considering tracer sorption and ‘predicted 2’ corresponds to that considering linear tracer sorption.....	126
Fig 7.4	Observed and predicted reactive breakthrough curves at different measurement lengths in the sandbox.....	130
Fig 7.5	Resultant fluorescence intensity of the observed and the various predicted reactive breakthrough curves for three different measurement locations in the sandbox. ‘predicted 1’ corresponds to prediction without considering sorption, and ‘predicted 2’ corresponds to prediction using AQUASIM considering sorption.....	132
Fig 7.6	Changes that occur to the originally considered advancing and receding front as a consequence of using the sorption parameters mentioned in this study. The measurement location is at 8.45m (same as the centre plot in Fig 7.5).....	133

LIST OF TABLES

Table 2.1	Analytical expressions for the most common sorption models.....	19
Table 2.2	Physical meaning of local and integrated temporal moments (Cirpka and Kitanidis, 2000a).....	29
Table 3.1	Relevant information on some tracer experiments in homogeneous porous media.	35
Table 3.2	Relevant information on some tracer experiments in heterogeneous porous media	37
Table 4.1	Properties of Fluorescein.....	48
Table 4.2	Properties of Lutensol GD 70.....	56
Table 4.3	Grain sizes and hydraulic conductivity of the sand types used in the sandbox ...	70
Table 5.1	Steps involved in the preparation of conservative test solution.....	79
Table 5.2	Steps involved in preparing solutions for the reactive test.....	87
Table 6.1	Parameters of interest calculated from the conservative breakthrough curves ...	90
Table 6.2	Accuracy and variability of quantities of interest (Column test)	99
Table 6.3	Grain size and hydraulic conductivity of sand types.....	109
Table 6.4	Accuracy and variability of quantities of interest (Sandbox test)	109
Table 6.5	Fitted parameters of linear stochastic theory.....	112
Table 7.1	Relevant moments of the observed and the predicted reactive breakthrough curves and their relative differences.....	120
Table 7.2	Characteristic times for the pore and column scales in this study compared to other published works.	128
Table 7.3	Values of fitted parameters for some reactive breakthroughs predicted using AQUASIM, considering sorption	132

LIST OF ABBREVIATIONS AND SYMBOLS

In this section, commonly used symbols, their definitions, and dimensions are given.

Abbreviations:

BTC	Breakthroughcurve
PVC	Polyvinylchloride
REV	Representative elementary volume
ZPC	Zero point charge

Dimensions

L	Length
M	Mass
T	Time

Variable	Physical Meaning	Dimension
α_{ij}	Local dispersivity	[L]
α^*_{ij}	Macrodispersivity	[L]
α_a	apparent dispersivity	[L]
α_L	Longitudinal transverse dispersivity	[L]
$\alpha_{T,h}$	Horizontal transverse dispersivity	[L]
$\alpha_{T,v}$	Vertical transverse dispersivity	[L]
δ_{ij}	Kronecker delta	[-]
γ	Kinetic coefficient of bimolecular reaction	[T ⁻¹]
λ	Correlation length of the aquifer heterogeneities	[L]
μ_0	Zeroth spatial moment	[L]
μ_i	First spatial moment	[L ²]
μ_{ij}	Second non-central spatial moment	[L ³]
μ_{ij}^c	Second central spatial moment	[L ³]
ϕ	inner diameter	[L]
ρ_w	Mass density of water	[M/L ³]
ρ_b	Bulk density of the aquifer	[M/L ³]

τ_a	Characteristic advective time	[T]
τ_d	Characteristic dispersive time	[T]
τ_{DT}	Dispersion time scale	[T]
A	Cross-sectional area	[L ²]
c	Solute concentration	[M/L ³]
\bar{c}	Average concentration of solute	[M/L ³]
c_{in}	Inflow solute concentration	[M/L ³]
c_s	Mass of solute sorbed per unit weight of dry solid	[M/M]
d_{50}	Mean grain diameter	[L]
D	Hydrodynamic dispersion tensor	[L ² /T]
D_{mech}	Mechanical dispersion tensor	[L ² /T]
D[*]	Macrodispersion coefficient	[L ² /T]
D_a	Apparent dispersion coefficient	[L ² /T]
D^{ens}	Ensemble dispersion coefficient	[L ² /T]
D_a	Apparent dispersion coefficient	[L ² /T]
D_d	Diffusion coefficient	[L ² /T]
D^e	Effective dispersion coefficient	[L ² /T]
D_L	Longitudinal dispersion coefficient	[L ² /T]
D_{T,h}	Transverse horizontal dispersion coefficient	[L ² /T]
D_{T,v}	Transverse vertical dispersion coefficient	[L ² /T]
E	Dilution index	[L ³]
F	Total mass flux	[M/LT ²]
F_a	Advective mass flux	[M/LT ²]
F_d	Diffusive flux of solute mass per unit area per unit time	[M/LT ²]
h	Separation vector	[L]
h	Hydraulic head	[L]
I	Identity matrix	[-]
I	Fluorescence Intensity	[-]
I_{rel}	Relative fluorescence intensity	[-]
I_{res}	Resultant fluorescence intensity	[-]
k	Rate of transformation	[T ⁻¹]

K_d	Solute distribution coefficient		$[L^3/M]$
K	Hydraulic conductivity		$[L/T]$
l	Correlation length		$[L]$
$\langle m_{2c} \rangle$	Cross-sectional average of second central temporal		
		moment	$[T^3]$
M	Reactor ratio		$[-]$
n_e	Effective porosity		$[-]$
Pe	Peclet number		$[-]$
Pe_g	Grain-scale Peclet number		$[-]$
Pe_f	Field-scale Peclet number		$[-]$
Pe_{mix}	Mixed-scale Peclet number		$[-]$
q	Darcy flux or specific discharge		$[L/T]$
Q	Volumetric discharge		$[L^3/T]$
r	transformation rate		$[T^{-1}]$
R	Retardation factor		$[-]$
s	Volumetric source/sink		$[L^3]$
s_m	Segregation intensity		$[-]$
S_0	Specific storage coefficient		$[-]$
t	Time		$[T]$
v	Seepage velocity		$[L/T]$
\bar{v}	Mean seepage velocity		$[L/T]$
v_a	Apparent seepage velocity		$[L/T]$
$V_{p,e}$	Interconnected pore volume		$[L^3]$
V_{total}	Total pore volume		$[L^3]$
X	Mixing ratio		$[-]$

1 INTRODUCTION

1.1 Background and Motivation

Among the available freshwater resources, groundwater constitutes the most important one. It is also one of the widely used freshwater resources mainly because of its large availability and high water quality. But with the advancement of intensive cultivation and industrialisation, a large number of groundwater aquifers became contaminated. This poses a great threat to humans who use groundwater as their primary source for drinking water needs.

Since the past few decades, remediation of contaminated aquifers and cleaning of polluted groundwater has gained importance. Therefore, much research is being conducted in this area resulting in the development of novel ideas. Some of the remediation methods, like bioremediation and natural attenuation, involve reaction between different compounds, and therefore an accurate estimate of their reaction rates is required to plan and design such remediation strategies. Hence, a considerable number of studies have been performed to understand the processes involving reactive mixing in heterogeneous porous media (*MacQuarrie and Sudicky, 1990; Ginn et al., 1995; Kapoor et al., 1997; Miralles-Wilhelm et al., 1997; Oya and Vallochi, 1998; Cirpka et al., 1999*). Studies have suggested that the dilution due to local-scale dispersion is the process that actually causes mixing, which culminates in the reaction between compounds. Dilution of a compound is enhanced by the spreading of the solutes induced by the aquifer heterogeneities. *Kitanidis (1994)* defined dilution as the decrease of the actual concentration peak as the mass is distributed over a larger volume.

Until the early 1990's, the macroscopic dispersion coefficient D^* has been used as a relative parameter for mixing. Macrodispersion actually is a quantity that describes the spreading of the plume at field scales. Reaction rates estimated from mixing calculated using D^* , resulted in their overprediction in heterogeneous aquifers (*Molz and Widdowson, 1988; Ginn et al., 1995; Miralles-Wilhelm et al., 1997; Cirpka et al., 1999*). This could lead to ineffective clean-up of the contaminated sites as the time for remediation is underestimated.

Therefore, it is necessary to substitute a better quantity, which accurately estimates the mixing, to predict the reaction rates. Since dilution is the process that leads to mixing, *Kitanidis (1994)* and *Kapoor et al., (1997)* suggested that quantities describing dilution would be a better estimate for mixing instead of macrodispersion, which includes both dilution and spreading of the plume.

Following these suggestions, numerical studies have been done by *Cirpka and Kitanidis (2000a)*, where parameters of mixing and dilution are derived from locally obtained breakthrough curves (BTCs) of a conservative tracer using the method of temporal moments. According to the latter authors, the effective dispersion coefficient D^e , which is the cross-sectional average of the locally estimated dilution coefficients, accurately estimates the mixing in that cross-section in contrast to the macrodispersion coefficients. In a contemporary study, *Cirpka and Kitanidis (2000b)* developed a numerical method to estimate reactive mixing from the dilution coefficients calculated from the conservative tests. *Dentz et al. (2000a)* and *Fiori and Dagan (2000)* have derived first-order spectral expressions for effective dispersion of point-related plumes in stationary flow fields and gave closed-form approximations for simple cases.

In addition to the above mentioned studies, much more studies have been conducted in this regard and they are explained in detail in *chapter 2*. But most of these studies are of a theoretical nature, or rely on numerical simulations.

1.2 Objectives

The objective of my thesis research is to conduct actual experiments as suggested by *Cirpka and Kitanidis (2000a)*, but with natural sedimentation pattern instead of a well-structured pattern. The data obtained from the experiments are used to verify the applicability of the theoretical concepts to real systems with natural sedimentation pattern. My research should provide answers for the following questions:

- Do point-like measurements of concentrations provide reliable information of dilution and mixing?
- Are (semi)-analytical results for effective dispersion and mixing from stochastic theory applicable to real data?

The study is restricted to cases in which mixing on the macro-scale is oriented in the longitudinal direction.

1.3 Tasks

In order to successfully achieve the objectives, following tasks have to be completed.

1. Development of a point measurement system
2. Selection of suitable conservative and reactive tracers
3. Experiments in a homogeneously packed column
4. Experiments in a heterogeneously packed sand-box

5. Interpretation of the results in accordance with the objectives

1.4 General Framework of the Experiments

In general, the experiments conducted within the framework of this research may be classified into conservative and reactive tracer tests.

In a conservative tracer test, the dilution of a conservative tracer is quantified by several point measurements of tracer concentration in the porous media. In the next step, the reactive mixing at the measurement locations is predicted from the conservative tracer data. The predicted reactive mixing is then compared to reactive mixing data, obtained for the respective porous media, from the reactive tracer tests.

1.5 Thesis Structure

This section provides you with a very brief description on what to expect in each chapter.

- *Chapter 2* provides the theoretical background that is essential for a basic understanding of the thesis.
- *Chapter 3* reviews laboratory experiments that are relevant and or comparable to the research addressed in this study.
- *Chapter 4* describes the materials and the setups that are employed to conduct the relevant experiments.
- *Chapter 5* gives details about different types and scales of experiments conducted in the framework of the thesis. Also a short description on the estimation of various quantities of interest from the measured data is provided.
- *Chapter 6* gives the results from conservative tests conducted in homogeneous and heterogeneous porous media. Parameters of dilution and mixing are derived from the results of conservative tests. The results obtained in the heterogeneous porous medium are qualitatively compared with the results from the numerical study of *Cirpka and Kitanidis (2000a)*. A modified version of the spectral solutions derived by *Dentz et al., (2000a)* and *Fiori and Dagan (2000)* for effective dispersion and macrodispersion is applied to the observed results.
- *Chapter 7* provides a comparison between the actual reactive mixing results to reactive mixing predicted from the conservative tests. Applicability of conservative data to predict reactive mixing is discussed in this chapter.
- *Chapter 8* summarizes the findings of this study and provides an outlook on further research possibilities.

If contents of any chapter are found to be of significance, one may proceed to the first paragraph of the relevant chapter where a more detailed description of the contents are given.

2 THEORETICAL BACKGROUND

In this chapter, the theory that is essential for a basic understanding of the thesis is provided.

The chapter is structured as follows:

- Short description of the basic concepts and the conservation principles in porous media,
- Discussion on scale effects of dispersion,
- Basics on solute transport modelling and statistical moments,
- Reactive transport and the processes that lead to reaction in porous media, and
- Various developments in quantifying dilution and dispersion-driven reactive mixing in porous media.

Finally, a short description of the system that is being considered in the study is explained.

2.1 Basic Concepts and Conservation Principles in Porous Media

2.1.1 Continuum hypothesis and REV

A rock mass consisting of mineral grains and pore spaces, or voids, is referred to as a porous medium (*Lichtner et al., 1996*). An actual porous medium is a highly heterogeneous body containing physical discontinuities marked by the boundaries of pore walls which separate the solid framework from the void space.

The common quantitative description of fluid flow within rocks is based on a mathematical idealization of the real physical system by a continuum. In the continuum representation of a porous medium, the physical variables describing the system, which are discontinuous on the pore scale, are replaced by continuous functions on the macroscale.

The value of each physical variable assigned to a point in the continuum is obtained by locally averaging the actual physical property over some representative elementary volume, REV (*Bear, 1972*). The dimensions of a REV are usually large compared to the grain size but small compared to the characteristic length scale over which the quantities of interest change.

2.1.2 Flow in porous media

2.1.2.1 Darcy's law

Darcy's law is fundamental to describing flow in a porous medium. The law states that the one-dimensional flow of water through a pipe filled with sand is proportional to the cross-

sectional area and the head loss along the pipe and inversely proportional to the flow length (*Darcy, 1856*).

$$\mathbf{q} = \frac{\mathbf{Q}}{A} = -\mathbf{K} \nabla h \quad (2.1)$$

where \mathbf{q} = Darcy flux or specific discharge

\mathbf{Q} = volumetric discharge

\mathbf{K} = hydraulic conductivity

A = cross-sectional area

∇h = spatial gradient of hydraulic head, or hydraulic gradient.

The hydraulic conductivity \mathbf{K} is defined as the measure for the capacity of a porous medium to transmit water (*Fetter, 1999*). It can have different values depending upon the actual direction of water flow through the porous media.

Since the actual flow takes place only in the interconnected pores, the average flow velocity or the seepage velocity, \mathbf{v} , is greater than the specific discharge, \mathbf{q} . The two quantities are related to each other by

$$\mathbf{v} = \frac{\mathbf{q}}{n_e} \quad (2.2)$$

where n_e is the effective porosity of the porous medium. The effective porosity is the ratio of the volume of the interconnected pores $V_{p,e}$, to the total volume of the porous media, V_{total} .

$$n_e = \frac{V_{p,e}}{V_{total}} \quad (2.3)$$

Darcy's law is valid only for laminar flow and when the pore sizes are much smaller than the characteristic dimensions governing the flow field.

2.1.2.2 Flow equation

The law of mass conservation states that the divergence of the mass flux $\rho_w \mathbf{q}$ must be balanced by the rate of change of the stored water mass $n_e \rho_w$ and internal sources/sinks of water mass $s \rho_w$:

$$\frac{\partial(n_e \rho_w)}{\partial t} + \nabla \cdot (\rho_w \mathbf{q}) = s \rho_w \quad (2.4)$$

in which ρ_w is the mass density of water and s is a volumetric source/sink term.

Equation (2.4) is known as the *continuity equation*. Considering that the compressibility of water is small, the spatial gradient of fluid density can be neglected.

$$\frac{1}{\rho_w} \frac{\partial(\rho_w n_e)}{\partial t} + \nabla \cdot \mathbf{q} = s \quad (2.5)$$

Substituting Darcy's law into (2.5) yields,

$$\frac{1}{\rho_w} \frac{\partial(\rho_w n_e)}{\partial t} - \nabla \cdot (\mathbf{K} \nabla h) = s \quad (2.6)$$

The change in the fluid density and porosity is proportional to the change in hydraulic head. Applying the chain rule to the temporal derivatives yields

$$\left(\frac{n_e}{\rho_w} \frac{\partial \rho_w}{\partial h} + \frac{\partial n_e}{\partial h} \right) \frac{\partial h}{\partial t} - \nabla \cdot (\mathbf{K} \nabla h) = s \quad (2.7)$$

or

$$S_0 \frac{\partial h}{\partial t} - \nabla \cdot (\mathbf{K} \nabla h) = s \quad (2.8)$$

where $S_0 = \frac{n_e}{\rho_w} \frac{\partial \rho_w}{\partial h} + \frac{\partial n_e}{\partial h}$ is known as the specific storage coefficient, describing the relative change of mass of the water stored in the porous medium due to an absolute change of the hydraulic head.

The above equation describes transient flow in an anisotropic medium. In a fully saturated medium, the specific storage coefficient is very small, because the compressibilities of both water and the pore spaces have small values. Therefore for a fully saturated medium we may assume quasi-steady state conditions which becomes for the case without internal sources/sinks:

$$\nabla \cdot (\mathbf{K} \nabla h) = 0 \quad (2.9)$$

2.1.3 Solute transport in porous media

Transport of solutes in fully saturated porous media occur due to

- diffusive processes, where the mass flux is against a concentration gradient, and
- advection, which is the mass flux of a solute with the moving water.

2.1.3.1 Diffusive Transport

Transport of a solute from a region of higher concentration to a region of lower concentration is known as *molecular diffusion*, or *diffusion*. Caused by Brownian motion, diffusion will occur as long as a concentration gradient exists, even if the fluid is not moving.

Fick's first law states that the diffusive mass flux density is proportional to the concentration gradient,

$$\mathbf{F}_d = -n_e D_d \nabla c \quad (2.10)$$

where

\mathbf{F}_d - diffusive flux of solute mass per unit area per unit time

D_d - diffusion coefficient

c - solute concentration

2.1.3.2 Transport by advection

The process where the dissolved solids are carried along with the flowing ground water is called advection. The advective mass flux density \mathbf{F}_a is the product of the solute concentration and the specific discharge

$$\mathbf{F}_a = \mathbf{q} c \quad (2.11)$$

2.1.3.3 Hydrodynamic dispersion

Due to heterogeneity of the geologic materials, groundwater containing a solute travels with varying velocities resulting in solute spreading along the flow path, which is called *mechanical dispersion*. The spreading along the direction of the flow is called longitudinal dispersion and the spreading in directions normal to the flow is called transverse dispersion.

Assuming that mechanical dispersion can be parameterized by an anisotropic diffusion law, we can introduce a mechanical dispersion tensor \mathbf{D}_{mech} :

$$\mathbf{D}_{mech} = \begin{bmatrix} D_L & 0 & 0 \\ 0 & D_{T,h} & 0 \\ 0 & 0 & D_{T,v} \end{bmatrix} \quad (2.12)$$

here formulated in the longitudinal/transverse system of coordinates in which D_L , $D_{T,h}$ and $D_{T,v}$ are the longitudinal, transverse horizontal and transverse vertical mechanical dispersion coefficients. According to *Scheidegger (1954)*, the directional dispersion coefficients are proportional to the seepage velocity \mathbf{v} :

$$D_L = \alpha_L |\mathbf{v}| \quad (2.13a)$$

$$D_{T,h} = \alpha_{T,h} |\mathbf{v}| \quad (2.13b)$$

$$D_{T,v} = \alpha_{T,v} |\mathbf{v}| \quad (2.13c)$$

in which α_L , $\alpha_{T,h}$, and $\alpha_{T,v}$ are the longitudinal, horizontal transverse, and vertical transverse dispersivities. They are assumed to be a property of the medium.

In flowing groundwater, the process of diffusion cannot be separated from mechanical dispersion. Therefore, the two are combined to define the *hydrodynamic dispersion tensor*, \mathbf{D} .

$$\mathbf{D} = \begin{bmatrix} \alpha_L \mathbf{v} + D_d & 0 & 0 \\ 0 & \alpha_{T,h} \mathbf{v} + D_d & 0 \\ 0 & 0 & \alpha_{T,h} \mathbf{v} + D_d \end{bmatrix} \quad (2.14)$$

For an arbitrary orientation of the velocity vector, we have to rotate the system of coordinates, leading to:

$$\mathbf{D} = \frac{\mathbf{v} \otimes \mathbf{v}}{|\mathbf{v}|} (\alpha_L - \alpha_T) + \mathbf{I} (D_d + \alpha_T |\mathbf{v}|) \quad (2.15)$$

in which $\mathbf{v} \otimes \mathbf{v}$ is the velocity dyad (the matrix product of the seepage velocity with itself), and \mathbf{I} is the identity matrix.

Therefore the dispersive mass flux, \mathbf{F}_d , can be finally represented as

$$\mathbf{F}_d = -n_e \mathbf{D} \nabla c \quad (2.16)$$

2.1.3.4 Advection-dispersion equation (ADE) for solute transport

For the derivation of the advection-dispersion equation (ADE), it is assumed that the porous medium is homogeneous, isotropic, and saturated with water, and flow conditions satisfy Darcy's law. The derivation is based on the law of mass conservation for a small REV of the porous media. The flow is at a macroscopic scale, i.e. within a domain including a sufficient volume that the effects of individual pores are averaged (*Bear, 1972*).

The mass flux due to both advection and hydrodynamic dispersion is,

$$\mathbf{F} = \mathbf{F}_a + \mathbf{F}_d = c\mathbf{q} - n_e \mathbf{D} \nabla c \quad (2.17)$$

The source and sink term is represented as, $s = c_{in} S_{in} - c S_{out}$, in which $c_{in} S_{in}$ is the source of the solute mass, and $c S_{out}$ is the solute mass leaving the solute volume.

Taking the above relations, the transport equation, without reaction, is formulated as,

$$\frac{\partial(n_e c)}{\partial t} + \nabla \cdot \mathbf{F} = s \quad (2.18)$$

Substituting for \mathbf{F} and s in the above equation,

$$\frac{\partial(n_e c)}{\partial t} + \nabla \cdot (c\mathbf{q} - n_e \mathbf{D} \nabla c) = c_{in} S_{in} - c S_{out} \quad (2.19)$$

Applying the chain rule of differentiation, the above equation becomes,

$$n_e \frac{\partial c}{\partial t} + c \frac{\partial n_e}{\partial t} + \mathbf{q} \cdot \nabla c + c \nabla \cdot \mathbf{q} - \nabla \cdot n_e \mathbf{D} \nabla c = c_{in} s_{in} - c s_{out} \quad (2.20)$$

which can be rewritten as,

$$\frac{\partial c}{\partial t} + c \frac{1}{\rho_w} \left(\frac{\partial n_e}{\partial t} + \nabla \cdot \mathbf{q} + s_{out} \right) + \frac{\mathbf{q}}{n_e} \cdot \nabla c - \frac{1}{n_e} \nabla \cdot (n_e \mathbf{D} \nabla c) = c_{in} \frac{s_{in}}{n_e} \quad (2.21)$$

Considering the continuity equation (2.4), the above equation is rearranged to

$$\frac{\partial c}{\partial t} + c \frac{1}{\rho_w} \frac{\partial \rho_w}{\partial t} + \mathbf{v} \cdot \nabla c - \frac{1}{\rho_w} \nabla \cdot (n_e \mathbf{D} \nabla c) = (c_{in} - c) \frac{s_{in}}{n_e} \quad (2.22)$$

Neglecting the compressibility of water, and assuming a uniform porosity, the transport equation for a system without source or sink is formulated as,

$$\frac{\partial c}{\partial t} + \mathbf{v} \cdot \nabla c - \nabla \cdot (\mathbf{D} \nabla c) = 0 \quad (2.23)$$

2.2 Scale Effects of Dispersion

2.2.1 Classification of dispersion

The values of hydrodynamic dispersion depend on the scale of observation. According to the scale of observation, dispersion could be generally classified as micro-scale (pore-scale) and macro-scale dispersion.

2.2.1.1 Microdispersion (pore-scale dispersion)

Microdispersion or pore-scale dispersion is caused by the combined effects of molecular diffusion and the spatial variability of advection on the sub-REV scale. It has been concluded from many lab-scale studies on homogeneous porous media that the pore-scale dispersivity depends on the mean grain size (*Bear 1969; 1972*).

2.2.1.2 Macrodispersion

Macrodispersion describes the spreading of a plume at field scales. Macrodispersion coefficients measure the expected rate of change of the second central spatial moments of a conservative tracer in a very large plume. The longitudinal macrodispersivity values increase with increasing travel distance or observation scale. The longitudinal macroscopic dispersion coefficients D_L^* can be orders of magnitude larger than the longitudinal pore-scale dispersion coefficients D_L (*Oelkers, 1996*). The wide variations in porosity and hydraulic conductivity, generally observed at field-scales, are the major reasons for an increase in macrodispersivity values with travel distance.

An upper limit for the longitudinal macrodispersion coefficient D_L^* in an isotropic heterogeneous aquifer is given by Dagan's (Dagan, 1984) well-known result:

$$D_{L,\infty}^* = \bar{v}\lambda\sigma_Y^2 \quad (2.24)$$

in which \bar{v} is the mean seepage velocity, λ is the correlation length of the aquifer heterogeneities, and σ_Y^2 is the variance of the log-conductivity. The macrodispersion coefficient $D_L^*(t)$ increases with time until it reaches its asymptotic value $D_{L,\infty}^*$. The time dependence can be described approximately by an exponential function with a characteristic time of about $2\tau_a = 2\lambda/\bar{v}$ in which τ_a is the advective time-scale related to the length-scale of the heterogeneities.

$$D_L^*(t) \approx D_{L,\infty}^* (1 - \exp(-t/(2\tau_a))) \quad (2.25)$$

A critical review on field-scale dispersivities by Gelhar *et al.*, 1992 classified dispersivities into three directions:

- Longitudinal dispersivity, α_L^* (in the direction of the flow).
- Horizontal transverse dispersivity, $\alpha_{T,h}^*$ (in direction perpendicular to the flow but parallel to the flow surface).
- Vertical transverse dispersivity, $\alpha_{T,v}^*$ (in direction normal to the flow and perpendicular to the surface).

Oelkers, (1996) suggests that it is reasonable to assume a ratio of 0.33 for $\alpha_{T,h}^*/\alpha_L^*$ for mass transport calculations in the absence of measured values for $\alpha_{T,h}^*$. Gelhar *et al.*, (1992) noted that measured $\alpha_{T,h}^*$ tend to be larger than the corresponding $\alpha_{T,v}^*$ values. It is reasonable to use $\alpha_{T,v}^*/\alpha_L^*=0.04$ for mass transport calculations in sedimentary environments in the absence of measured data (Oelkers, 1996). The reported values for vertical transverse dispersivities are normally much less than 1mm (Grathwohl *et al.*, 2000; Klenk and Grathwohl, 2002).

2.2.1.3 Effective dispersion coefficient

In addition to the pore-scale and macrodispersion coefficients, I also consider a mixing related coefficient. Dilution, which is defined as the decrease in the actual concentration peak as mass is distributed over a larger volume (Kitanidis, 1994), is considered as the process that leads to mixing between potential reactants and therefore determines the amount of product mass in

reactive transport (Cirpka et al., 2000a ,b; Kapoor et al., 1997). While macrodispersion describes the combined effects of spreading and mixing, the effects of mixing alone can be parameterized by the so-called effective dispersion coefficients, $D_L^e(t)$, describing the expected spreading rate of a point source rather than a very large plume (Cirpka and Kitanidis, 2000a; Cirpka 2002) (see also section 2.5.2).

2.2.2 Characteristic times

Since a large part of my thesis deals with mixing-controlled reactive transport, the difference between spreading and mixing of compounds is extensively discussed. It has been reported that mixing leading to reaction is accurately estimated by dilution, and not by the spreading related quantities, which normally leads to the overestimation of reaction (Kitanidis, 1994; Kapoor et al., 1997; Cirpka and Kitanidis, 2000a). Depending on whether spreading or mixing is considered, two types of characteristic times are to be considered – a characteristic advective time $\tau_a = \lambda/v$, and a characteristic dispersive time $\tau_d = \lambda^2/D$, where λ corresponds to the correlation length. Both scales have a direct physical interpretation: in the time given by τ_a , the solute is advected over the distance of one disorder correlation length; in the time τ_d , the solute cloud has spread by molecular diffusion or local dispersion over the same length.

At $t > \tau_a$, macrodispersion coefficient D^* nears its asymptotic value. For normal field conditions, $t \gg \tau_a$ and for the time regime $\tau_a < t < \tau_d$, D^e grows relatively fast and reaches values that are comparable to its asymptotic value, which is equal to D^* at $t \gg \tau_d$.

The characteristic times are again classified based on the observation scale as grain- and field-scale characteristic times:

$$\text{Grain-scale advective time: } \tau_{a,g} = \frac{d_{50}}{v} \quad (2.26a)$$

$$\text{Grain-scale dispersive time: } \tau_{d,g} = \frac{d_{50}^2}{D_d} \quad (2.26b)$$

$$\text{Field-scale advective time: } \tau_{a,f} = \frac{l}{v} \quad (2.26c)$$

$$\text{Field-scale longitudinal dispersive time: } \tau_{d,f} = \frac{l^2}{D_L} \quad (2.26d)$$

where d_{50} is the mean grain diameter, and l is the correlation length in the flow direction. The characteristic field-scale dispersive time could be classified again based on dispersivities and correlation lengths in the three principal directions.

2.2.3 Peclet numbers

The relative contribution of mechanical dispersion and diffusion to solute transport is evaluated using dimensionless Peclet numbers, Pe . Depending on the observation scale, they are classified into grain-scale Pe_g , and field-scale Peclet numbers Pe_f :

$$Pe = \frac{\tau_d}{\tau_a} \quad (2.27a)$$

$$Pe_g = \frac{v d_{50}}{D_d} \quad (2.27b)$$

$$Pe_f = \frac{v l}{D_L} \quad (2.27c)$$

where D_L is the longitudinal hydrodynamic dispersion coefficient.

It was reported from various lab-scale experiments that diffusion dominates solute transport for Pe_g below 0.4, while both diffusion and mechanical dispersion are relevant at Pe_g values between 0.4 and 5. For Pe_g values greater than 5, mechanical dispersion dominates the system (*Bear, 1969; Bear, 1972*).

From different models that were developed to distinguish between longitudinal and transverse hydrodynamic dispersion coefficients in lab-scale studies, it was found that for Pe_g values greater than 30, $\frac{D_T}{D_L}$ generally varied between 0.01 and 0.03, and for Pe_g values less than 0.5, the value was 1.

If dilution at a control plane is estimated from several point measurements of tracer concentration as described in *Cirpka and Kitanidis (2000a)*, then the characteristic grain-scale dispersive time determines the validity of the concept of complete mixing. Under these conditions, a mixed Peclet number Pe_{mix} is introduced to determine the speed with which mixing catches up with spreading.

$$Pe_{mix} = \frac{\tau_{d,g}}{\tau_{a,f}} \quad (2.27d)$$

2.3 Solute Transport Modeling

Modeling of solute transport is done mainly by two approaches – the deterministic approach and the stochastic approach.

2.3.1 Deterministic models

In deterministic models, partial differential equations for the required variables are solved either numerically or analytically considering that the underlying aquifer parameters are exactly known. This yields results with a single output value for each point in the aquifer.

2.3.2 Stochastic models

In stochastic models, a probabilistic approach is used. For example, the parameter values of hydraulic conductivity and porosity may vary considerably in an aquifer (*Freeze, 1975; Dagan, 1988*), and it is impossible to accurately determine these aquifer parameters. In order to predict flow and transport in such heterogeneous aquifers, the spatial and temporal variability of the aquifer parameters have to be characterized. For this purpose, stochastic models have been used.

In the stochastic approach, the small-scale variability of the hydraulic properties is treated as being random in an appropriate, relatively simple fashion. As a consequence, the hydraulic-head, velocity and concentration fields are also random space variables. A random space variable, Y , typically is characterized by its mean \bar{Y} , and variance σ_Y^2 :

$$\bar{Y} = E[Y] = \lim_{n \rightarrow \infty} \frac{1}{n} \sum_{i=1}^n Y_i \quad (2.28)$$

$$\sigma_Y^2 = E[(Y - \bar{Y})^2] = \lim_{n \rightarrow \infty} \frac{1}{n-1} \sum_{i=1}^n (Y_i - E[Y])^2 \quad (2.29)$$

in which Y_i is the value of the random space variable Y at location \mathbf{x}_i , and $E[]$ is the expected-value operator. A normally distributed parameter is fully characterized by its mean and variance. Since Y is a random space variable, its value varies from location to location. The similarity of Y values at different locations is expressed by the autocovariance $R_{Y(x_1)Y(x_2)}$ function:

$$R_{Y(x_1)Y(x_2)} = E[(Y(x_1) - E[Y(x_1)])(Y(x_2) - E[Y(x_2)])] \quad (2.30)$$

When the above equation is used to define correlations between different quantities at separate points, then it is called crosscovariance function. Random fields for which the expected value and the variance of $Y(\mathbf{x})$ remain identical throughout the domain are called

stationary. The autocovariance $R_{Y(x_1)Y(x_2)}$ of stationary fields depends exclusively on the separation vector $\mathbf{h} = \mathbf{x}_1 - \mathbf{x}_2$, and not on the particular locations \mathbf{x}_1 and \mathbf{x}_2 .

An alternative measure for the autocovariance is the variogram $\gamma_{YY}(h)$, which has the advantage that it could be calculated without any knowledge of \bar{Y} .

$$\gamma_{YY}(h) = 0.5 E[(Y(x_1) - Y(x_2))^2] \quad (2.31)$$

The autocovariance function and the variogram relate to each other by:

$$R_{YY}(h) = \sigma_Y^2 - \gamma_{YY}(h) \quad (2.32)$$

From the above relations it is obvious that $R_{YY}(0) = \sigma_Y^2$. The same statistical methods are also used for random temporal distributions, where time increments Δt are considered instead of spatial separations h .

The major techniques employed to characterize the correlations between parameters are the spectral approach, the direct solution approach via a response function, and the solution of differential equations describing the covariance functions. The spectral approach has the advantage that it involves relatively simple mathematical manipulations, even for multidimensional systems while the response function and covariance differential equation approach has the advantage that they can treat nonstationary situations (*Gelhar, 1993*).

The output of a stochastic model is always a probabilistic distribution of possible values corresponding to the distribution of the parameters. The relevance of each output is then checked by comparing the accuracy of the simulated values at measurement locations. Finally a collection of all such simulation results satisfying the statistical characteristics of the aquifer and the observed values at the measurement locations are averaged to form the most probable distribution of the relevant aquifer parameter. Such results are usually expressed in terms of some simple statistical measures, such as the mean behaviour representing the central tendency and a variance reflecting the possible spread around the mean. Output from each simulation is called a 'realisation' and the average of all the realisations is called an 'ensemble'.

2.3.3 Statistical moments

The exact shape of a solute cloud introduced into a fluid may be very irregular. Since it is difficult to measure the actual distribution of such a plume, they are characterized by their statistical moments. Statistical moments could be estimated from spatial or temporal distributions.

2.3.3.1 Spatial moments

The zeroth, first, second, and second central spatial moments are defined by:

$$\mu_0(t) = \int_{V_\infty} c(\mathbf{x}, t) dV \quad (2.33)$$

$$\mu_i(t) = \int_{V_\infty} x_i c(\mathbf{x}, t) dV \quad (2.34)$$

$$\mu_{ij}(t) = \int_{V_\infty} x_i x_j c(\mathbf{x}, t) dV \quad (2.35)$$

$$\mu_{ij}^c(t) = \int_{V_\infty} (x_i - \bar{x}_i)(x_j - \bar{x}_j) c(\mathbf{x}, t) dV = \mu_{ij}(t) - \frac{\mu_i(t) \mu_j(t)}{\mu_0(t)} \quad (2.36)$$

without repeated summation. The integral $\int_{V_\infty} dV$ implies integration from $-\infty$ to $+\infty$ over all spatial dimensions. In the above expressions, $\mu_0(t)$ is the zeroth spatial moment of the concentration distribution, $\mu_i(t)$ is the first spatial moment in direction x_i , $\mu_{ij}(t)$ is the second non-central spatial moment in the directions x_i and x_j , and $\mu_{ij}^c(t)$ is the second central spatial moment.

The zeroth moment $\mu_0(t)$ is the total mass of the solute, the vector of first moments $\mu_i(t)$ is the total mass times the position of the center of gravity \bar{x}_i . Mostly the matrix of second central moments $\mu_{ij}^c(t)$, which describes the amount of spreading of the solute plume around the center of gravity, is used rather than that of the second non-central moments.

2.3.3.2 Temporal moments

Temporal moments are defined by:

$$m_0(\mathbf{x}) = \int_{t=0}^{\infty} c(\mathbf{x}, t) dt \quad (2.37)$$

$$m_i(\mathbf{x}) = \int_{t=0}^{\infty} t^i c(\mathbf{x}, t) dt \quad (2.38)$$

$$\bar{t}(\mathbf{x}) = \frac{m_1(\mathbf{x})}{m_0(\mathbf{x})} \quad (2.39)$$

$$m_i^c(\mathbf{x}) = \int_{t=0}^{\infty} (t - \bar{t}(\mathbf{x}))^i c(\mathbf{x}, t) dt \quad (2.40)$$

where $m_0(\mathbf{x})$ is the zeroth temporal moment, $m_i(\mathbf{x})$ and $m_i^c(\mathbf{x})$ are the i^{th} temporal non-central and central moments, and $\bar{t}(\mathbf{x})$ is the mean breakthrough time.

The first spatial moment is inversely related to the first temporal moment by:

$$\frac{\mu_1(t)}{\mu_0(t)} = \mathbf{x} t \frac{m_0(\mathbf{x})}{m_1(x)} \quad (2.41)$$

and the second central spatial moment is proportional to the product of the velocity and the second central temporal moment:

$$\mu_{2c}(t) = \frac{\mu_0(t)}{m_0(\mathbf{x})} \mathbf{v}^3 m_{2c}(\mathbf{x}) \quad (2.42)$$

2.4 Reactive Transport in Heterogeneous Porous Media

A solute undergoing transport in an aquifer may encounter mainly three types of heterogeneity, namely

- (1) Physical heterogeneities due to regions with varying hydraulic conductivities,
- (2) Chemical heterogeneities due to spatial non-uniformity in the chemical properties or reactive mineral abundance, and
- (3) Microbiological heterogeneities due to nonuniform availability and growth of microorganisms in the aquifer.

2.4.1 Chemical reactions in porous media

Chemical reactions that can occur in solute transport have been classified into six different categories by *Rubin (1983)* (Fig 2.1). At the highest level, reactions are classified into

1. ‘sufficiently fast’ and reversible
2. ‘insufficiently fast’ and/or irreversible

Fast reactions are reversible in the thermodynamic sense of a reversible process and are locally in thermodynamic equilibrium (*Lichtner et al., 1996*). Slow reactions are either reversible or irreversible processes in the language of thermodynamics and require a kinetic rate law to determine the reaction rate. Conventionally the reversible and irreversible reactions are used with a different meaning when referring to kinetic reactions. An irreversible kinetic reaction is one which proceeds in only one direction, whereas a reversible kinetic reaction can proceed in the forward and backward directions.

In the next level, the reactions are classified into homogeneous or heterogeneous based on the number of phases involved in the reaction. Homogeneous reactions take place within a single phase, whereas heterogeneous reactions involve several phases.

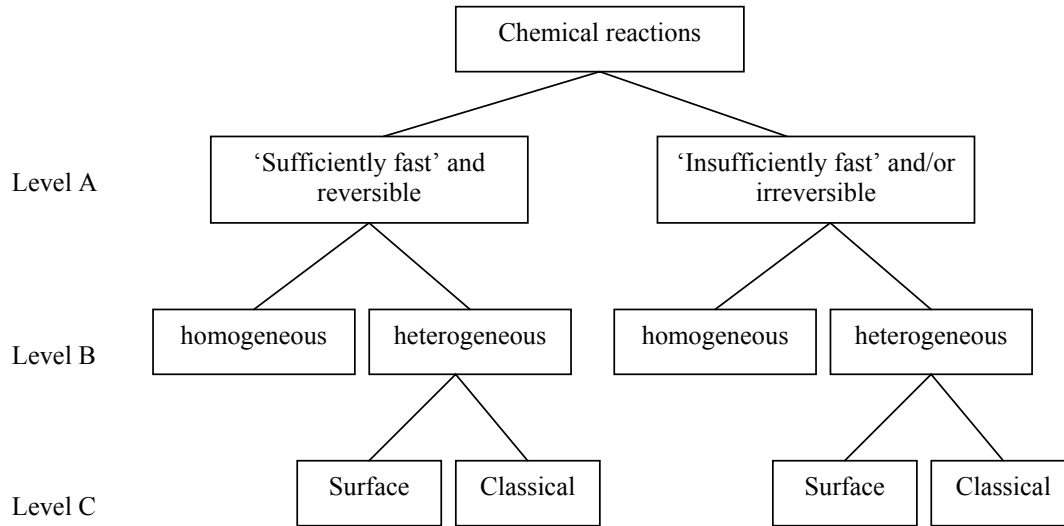


Fig 2.1 Classification of chemical reactions in porous media (*Rubin, 1983*)

The next level of classification applies only to heterogeneous reactions. These can be either surface reactions, such as hydrophobic adsorption of neutral organic compounds and ion exchange of charged ions, or classical chemical reactions such as precipitation and dissolution.

2.4.2 Retardation

Solutes transported with groundwater might undergo processes like sorption, resulting in a slow solute velocity compared to the groundwater flow velocity. This effect is termed as retardation.

Consider advective-dispersive transport of a solute undergoing inter-phase mass transfer:

$$\frac{\partial c}{\partial t} + \frac{\rho_b}{n_e} \frac{\partial c_s}{\partial t} + \mathbf{v} \cdot \nabla c - \nabla \cdot (\mathbf{D} \nabla c) = 0 \quad (2.43)$$

in which ρ_b is the bulk density of the aquifer, and c_s is the mass of solute sorbed per unit weight of dry solid. If the characteristic time-scale of inter-phase mass-transfer is much smaller than that of advection and dispersion, we may assume local equilibrium leading to:

$$R \frac{\partial c}{\partial t} + \mathbf{v} \cdot \nabla c - \nabla \cdot (\mathbf{D} \nabla c) = 0 \quad (2.44)$$

with the retardation factor R :

$$R = 1 + \frac{\rho_b}{n_e} \frac{\partial c_s}{\partial c} \quad (2.45)$$

Table 2.1 shows the major three types of sorption isotherms used to quantify equilibrium sorption – linear, Freundlich and Langmuir. There are also several models to describe nonequilibrium sorption processes. It is recommended to refer text books on transport in porous media for details regarding such models (*eg. Fetter, 1999*).

Table 2.1 Analytical expressions for the most common sorption models.

Type	Sorption Isotherm	R
Linear	$c_s = K_d c$	$1 + \frac{\rho_b}{n_e} K_d$
Freundlich	$c_s = K c^N$	$1 + \frac{\rho_b}{n_e} K N c^{N-1}$
Langmuir	$c_s = \frac{\beta c}{1 + \alpha c}$	$1 + \frac{\rho_b}{n_e} \left(\frac{1}{(1 + \alpha c)^2} \right)$

K_d , K , and N are constant coefficients; α is an adsorption constant related to the binding energy; β is the maximum amount of solute that can be adsorbed by the solid.

2.4.3 Processes influencing mixing

In order for a reaction to occur between potential reactants, they must mix. Two reactants that are being transported in a porous media could mix due to any of the following processes (*Cirpka, 2001b*):

- Chromatographic mixing
- Kinetic mass transfer
- Pore-scale dispersion

Chromatographic mixing is a mixing process which is based on differences in the mass transfer of compounds, namely sorption, at equilibrium. In this process a more mobile compound introduced into a porous media containing a less mobile compound will surpass the later at some distance in the aquifer resulting in mixing between them. *Oya and Vallochi (1998)* referred to this process as advective mixing.

Kinetic mass transfer leads to a delayed response of immobile-phase concentrations to concentration changes in the aqueous phase. Since the mass flux from the immobile to the aqueous phase continues even after the front has passed, kinetic mass transfer leads to longitudinal mixing.

Compounds that are introduced into the aquifer at different times could mix also due to *pore-scale dispersion*. In contrast to the first two processes mentioned, dispersion is active as

a mixing process even if no mass-transfer occurs, and it acts into the principle direction of flow as well as transverse to it.

2.4.4 Dispersion-controlled reactive mixing

In groundwater flow and transport, the smallest scale of consideration is the Representative Elementary Volume (REV). Molecular diffusion and spatial variability of advection on the sub-REV scale leads to pore-scale (or local-scale) dispersion. Two compounds that initially occupy separate volumes in an aquifer (Fig 2.2a), need to get into each other's territory in order to react. In dispersion-controlled reactive mixing, pore-scale dispersion is the process that makes a compound spread from its original location to adjacent regions of low concentration at the REV-scale under no-flow conditions. As a consequence, the peak concentration of a particular compound is reduced over time while the volume occupied by it increases. When two compounds diffuse into the regions originally occupied separately by each other, they mix and may react (Fig 2.2c).

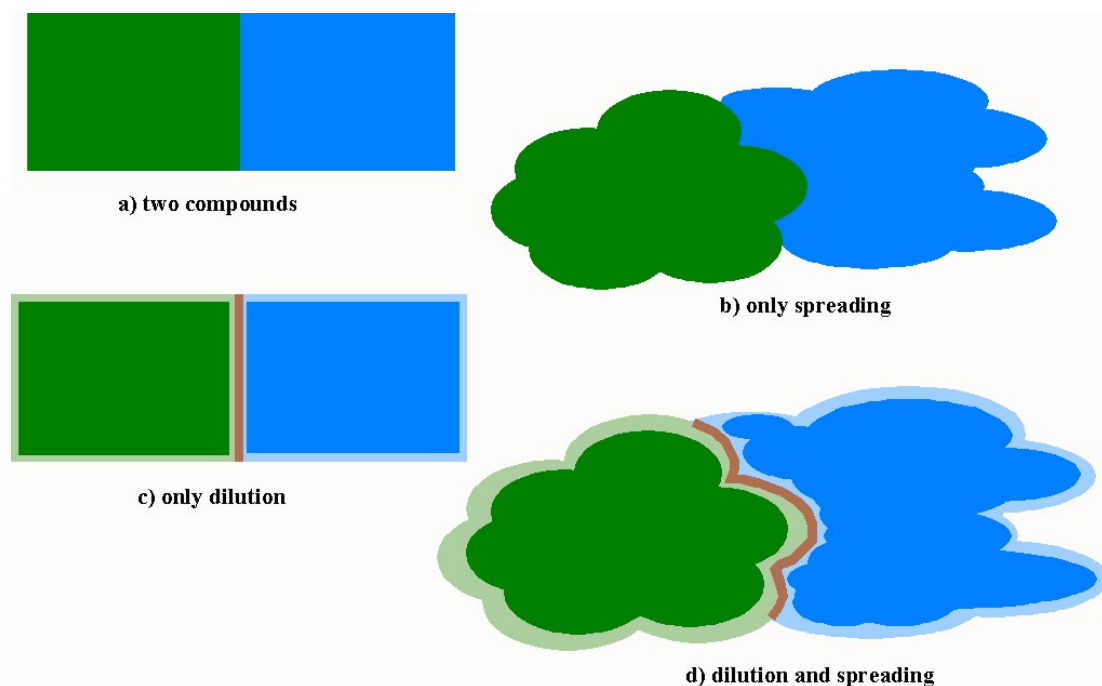


Fig 2.2 Reactive mixing of compounds

Consider two plumes of non-sorbing compounds being transported in a heterogeneous aquifer. In the absence of local-scale dispersion, the volume occupied by the plumes will not increase although the plume shapes might have distorted due to spreading by aquifer heterogeneities. Unless the volume occupied by each plume increases and enters the volume occupied by others, they won't mix to react (Fig 2.2b). Therefore from the above two cases, it

is clear that local-scale dispersion is the actual process that leads to mixing on the smallest scale.

Under natural groundwater conditions, local-scale dispersion and heterogeneity-induced spreading act concurrently. Local-scale dispersion dilutes the solute plumes while the advective-spreading enhances the dilution by providing extended mixing interface (Fig 2.2d). Results from various studies have indicated that the dilution due to local-scale dispersion is the process that actually causes mixing, which culminates in the reaction between compounds (MacQuarrie and Sudicky, 1990; Kapoor and Gelhar, 1994a, b). Kitanidis (1994) defined *dilution* as the decrease of the actual concentration peak as the mass is distributed over a larger volume.

2.5 Approaches in Quantifying Dilution

2.5.1 Quantifying mixing using macrodispersion

As mentioned in the previous section, dilution is the process that leads to mixing and reaction, if the reaction is controlled by mixing. Hence, accurate determination of dilution is crucial in predicting reactive mixing.

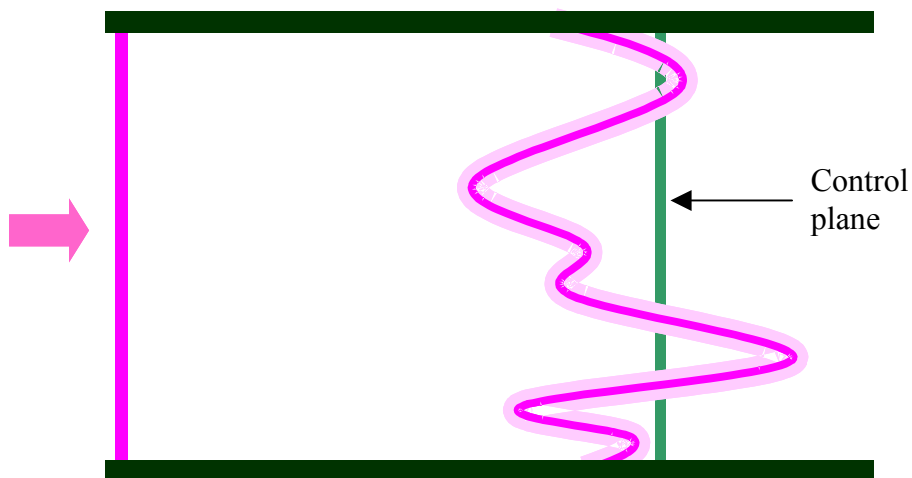


Fig 2.3 Measuring plume concentrations at a control plane

Consider a solute plume introduced as a Dirac pulse along the inflow boundary into a heterogeneous domain as shown in Fig 2.3. The transport of the conservative solute can be represented by the advection-dispersion equation (ADE):

$$\frac{\partial c}{\partial t} + \mathbf{v} \cdot \nabla c - \nabla \cdot (\mathbf{D} \nabla c) = 0 \quad (2.23)$$

where c is the tracer concentration, t is the time, \mathbf{v} is the seepage velocity, and \mathbf{D} is the hydrodynamic dispersion coefficient.

As the conservative solute plume travels in the porous medium encountering the heterogeneity, it dilutes, due to local-scale dispersion, as well as spreads, due to the encountered large-scale heterogeneities. A solute plume could be characterized by its statistical moments. The first spatial moment, μ_1 (eq. 2.34), and the second central spatial moments, μ_{2c} (eq. 2.36), yield information of the centre of gravity, and the spread of the plume, respectively. Furthermore, the longitudinal dispersion coefficients are defined as half the rate of change of the second central spatial moments:

$$D_L = \frac{1}{2\mu_0} \frac{\partial \mu_{2c}}{\partial t} \quad (2.46)$$

and the longitudinal dispersion coefficients are related to the second central temporal moments as follows:

$$D_L = \frac{v^3}{2m_0} \frac{\partial m_{2c}}{\partial x} \quad (2.47)$$

In most of the tracer studies, the solute concentrations were measured along a control plane yielding the average concentration \bar{c} . The dispersion coefficients estimated from the averaged concentration is the macrodispersion coefficient, which is actually a measure of spreading of the plume. In the past, macrodispersion values were substituted for hydrodynamic dispersion coefficient in the conservative transport equation (eq. 2.23) to estimate the mixing of a conservative solute plume. Since macrodispersion is a spreading related quantity, it includes the irregularity of the plume in addition to the actual dilution, and therefore mixing predicted using those values led to its overestimation (*Molz and Widdowson, 1988; Ginn et al., 1995; Kapoor et al., 1997; Cirpka, 2002; Gelhar, 1993; Kemblowski et al., 1997*). Hence, it is suggested that substituting a quantity for dilution instead of classical dispersion coefficients will lead to better prediction of dispersion-controlled reactive mixing (*Kitanidis, 1994; Cirpka and Kitanidis, 2000a*).

2.5.2 Other parameters to quantify mixing

Since mixing predicted using macrodispersion values resulted in its overestimation, several studies were conducted to quantify mixing more accurately. *Kitanidis (1994)* introduced a new macroscopic measure of dilution called the *dilution index*, $E(t)$, which is defined as the volume of the porous medium that is occupied by the solute:

$$E(t) = \exp \left[- \int_V p(x,t) \ln(p(x,t)) dV \right] \quad (2.48)$$

where $p(x,t) = \frac{c(x,t)}{\int c(x,t)dV}$ - is the distribution function of the mass.

He also introduced the *reactor ratio*, M , which is defined as the ratio of the actual dilution index to the maximum dilution index that is theoretically possible consistent with other limitations:

$$M = \frac{E}{E_{max}} \quad (2.49)$$

where E_{max} for field applications is the dilution index of the corresponding Gaussian concentration distribution. The reactor ratio is a relative indicator of the actual mixing of the solute.

The study showed that the instantaneous rate of increase of dilution depends only on the local dispersion coefficient and the shape of the plume. For a Gaussian plume, the rate of increase of the dilution index requires information only about the local dispersion coefficients and the spread of the plume:

$$\frac{d \ln(E)}{dt} = D_{ij} (\mu_{2c}^{-1})_{ij} \quad (2.50)$$

μ_{2c}^{-1} - inverse of the second central moments

If the plume is not Gaussian, the above expression is a lower bound to the dilution rate.

Kapoor and Gelhar (1994a, b) studied the dynamics of concentration fluctuations in solute transport in three dimensional heterogeneous aquifers and concluded that a higher concentration variance is an indicator of incomplete mixing. The concentration variance is the mean squared difference between the actual concentration and the mean concentration. They developed the following conservation equation for the concentration variance:

$$\frac{\partial \sigma_c^2}{\partial t} + v \frac{\partial \sigma_c^2}{\partial x_1} - v \alpha_{ij} \frac{\partial^2 \sigma_c^2}{\partial x_i \partial x_j} + \frac{\partial}{\partial x_i} (\overline{v_i' c'^2}) = 2v \alpha_{ij}^* \frac{\partial \bar{c}}{\partial x_i} \frac{\partial \bar{c}}{\partial x_j} - 2v \alpha_{ij} \frac{\partial c'}{\partial x_i} \frac{\partial c'}{\partial x_j} \quad (2.51)$$

where σ_c^2 : is the concentration variance

α_{ij} : is the local dispersivity

α_{ij}^* : is the macrodispersivity

and all quantities with a prime are deviations from their means.

According to equation (2.51), the concentration variance undergoes mean advection and local dispersive flux (terms 2 and 3, respectively), a macrodispersive flux (term 4), and is produced and dissipated by the first and second terms on the right hand side of the equation,

respectively. They found that the rate of production of concentration variance is determined by the product of the macrodispersion coefficient and the squared gradient of the mean concentration field, while the rate of dissipation of concentration variance is determined by the product of the local dispersion coefficient and the mean squared gradient of the concentration perturbation field. They concluded that the concentration variance can only be destroyed by local dispersion. *Kapoor and Kitaniadis (1996, 1998)* numerically verified the above concepts in different types of heterogeneous aquifers and showed that the total concentration variance and the dilution index are related measures for dilution.

Kapoor et al., (1997) studied reactive transport of nonsorbing compounds in a heterogeneous porous medium. The reaction considered was a bimolecular reaction with the rate of transformation $r(c_1, c_2) = k c_1 c_2$. They found that the usual practice of estimating transformation rates from the spatial averages of concentrations (ie. $r(\overline{c_1}, \overline{c_2}) = k \overline{c_1} \overline{c_2}$) leads to overprediction of the actual product concentration. Therefore they developed an accurate method to predict the transformation rate by introducing a factor called segregation intensity,

$$s_m = \frac{\overline{c_1' c_2'}}{c_1 c_2},$$

which is similar to the concentration variance mentioned earlier, but for two compounds:

$$r(c_1, c_2) = (1 + s_m) \times r(\overline{c_1}, \overline{c_2}) \quad (2.52)$$

The segregation intensity is strongly related to both the flow variations and the small scale mixing mechanisms like diffusion and local dispersion

The temporal behaviour of a solute cloud in a heterogeneous porous medium was studied by *Dentz et al., 2000a*. In the study, the resulting centre of mass velocity and two conceptually different dispersion coefficients – the ‘effective’ dispersion coefficient, D^e and the ‘ensemble’ dispersion coefficient, D^{ens} , - which were first mentioned in *Attinger et al., 1999* were analysed. The ensemble dispersion coefficient mentioned in *Dentz et al., 2000a* is denoted as absolute dispersion in *Andricevic and Cvetkovic (1998)*. The effective dispersion coefficient is derived from the average of the second central spatial moments evaluated in each realisation (2.53), and the ensemble dispersion coefficient is evaluated from the second central spatial moment of the ensemble-averaged concentration distribution (2.54).

$$D_{ij}^e(t) = \frac{1}{2} \frac{d}{dt} \left(\overline{\mu_{ij}^2(t) - \mu_i^1(t) \mu_j^1(t)} \right) \quad (2.53)$$

$$D_{ij}^{ens}(t) = \frac{1}{2} \frac{d}{dt} \left(\overline{\mu_{ij}^2(t)} - \overline{\mu_i^1(t)} \overline{\mu_j^1(t)} \right) \quad (2.54)$$

It is known that the ensemble dispersion coefficient takes into account an artificial dispersion effect caused by fluctuations of the centre-of-mass positions of the solute clouds in different realizations of the heterogeneous medium, and this quantity is similar to the macrodispersion coefficient. This effect is suppressed in the calculation of the effective dispersion coefficient, and therefore it is considered to be a better measure to quantify dilution or mixing of a solute cloud (Cirpka, 2002). The solutions to $D_{ij}^{ens}(t)$ and $D_{ij}^e(t)$ in the spectral domain are derived as given in equations (2.55) and (2.56).

$$\mathbf{D}^{ens} = \mathbf{D} + \int_0^t \int \mathbf{S}_{\mathbf{v}\mathbf{v}^T}(\mathbf{s}) \exp((-4\pi^2 \mathbf{s}^T \mathbf{D} \mathbf{s} - 2\pi i \bar{\mathbf{v}}^T \mathbf{s})(t-t')) dt' ds \quad (2.55)$$

$$\mathbf{D}^e = \mathbf{D}^{ens} - \int_0^t \int \mathbf{S}_{\mathbf{v}\mathbf{v}^T}(\mathbf{s}) \exp(-4\pi^2 \mathbf{s}^T \mathbf{D} \mathbf{s}(t+t') - 2\pi i \bar{\mathbf{v}}^T \mathbf{s}(t-t')) dt' ds \quad (2.56)$$

where \mathbf{D} → pore-scale dispersion tensor
 $\mathbf{S}_{\mathbf{v}\mathbf{v}^T}$ → power spectrum of velocity fluctuations
 \mathbf{s} → wave number

The solutions in the spectral domain are to the first order accurate. It is found that the longitudinal ensemble dispersion coefficient D_{11}^{ens} at large times reached its asymptotic limit:

$$D_{11}^{ens}(t) = D_L + \sigma_Y^2 \bar{v} \lambda_h \quad (2.57)$$

where D_L → longitudinal pore-scale dispersion coefficient
 σ_Y^2 → variance of log conductivity
 \bar{v} → mean velocity, and
 λ_h → correlation length in x direction

It was found that the longitudinal effective dispersion coefficient, $D_{11}^e(t)$ for a solute introduced by point-injection followed $D_{11}^{ens}(t)$ as in equation (2.58).

$$D_{11}^e(t) = D_{11}^{ens}(t) \frac{t}{\left(\frac{\pi}{8}\right) \tau_{D_r} + t} \quad (2.58)$$

where τ_{D_r} → dispersion time scale.

They showed from eq. 2.58 that the temporal behaviour of the two quantities differ considerably at finite times. It was found that the ensemble dispersion coefficients reached an asymptotic limit at times greater than the advective time scale, $\tau_a = \frac{\lambda_h}{v}$. At times much

greater than the dispersion time scale $\tau_{D_T} = \frac{\lambda_h^2}{D_T}$, where D_T is the local transverse dispersion coefficient, the effective dispersion coefficient reaches an asymptotic limit that is identical to the ensemble dispersion coefficient.

The temporal behaviour of an extended solute plume injection rather than a point injection in a heterogeneous aquifer was studied in *Dentz et al., 2000b*. The explicit analytical solutions derived in the paper confirm and quantify the concept that the difference between the two dispersion coefficients becomes less pronounced with an increase in the size of the solute source. They also demonstrated that neglecting the effects due to local dispersion may easily lead to erroneous predictions.

Since most of the above concepts were developed based on spatial moments, determining the degree of dilution at field sites will require high spatial resolution of measurement locations, which is unlikely in normal field situations. Therefore it is difficult to determine the above quantities in the field. By contrast, temporal moments could easily be measured in field studies by repeated sampling of few monitoring wells. Therefore *Cirpka and Kitanidis, 2000a* describe a method to quantify dilution and mixing using temporal moments. A method to predict reactive mixing from the dilution that has been quantified from conservative tests (*Cirpka and Kitanidis, 2000a*) is given in *Cirpka and Kitanidis, 2000b*.

2.5.3 Quantifying dilution using local temporal moments

2.5.3.1 The concept

A method to accurately estimate dilution and mixing using local temporal moments has been mentioned in *Cirpka and Kitanidis, 2000a*. Since the thesis is based on their work, it is discussed here in detail.

The system considered in the study is same as that mentioned in section 2.5.1. The paper suggests that if point measurements of conservative tracer concentration c could be obtained at the control plane instead of the averaged concentration \bar{c} (Fig 2.4), subsequently, the second central temporal moments m_{2c} are calculated from each point concentration profile. The values of m_{2c} calculated from each point measurements are then averaged across the control plane to obtain the averaged second central temporal moments, $\langle m_{2c} \rangle$. Substituting $\langle m_{2c} \rangle$ for m_{2c} in equation (2.47) yields the effective dispersion coefficient, D^e .

According to the authors, D^e is a more accurate measure to estimate mixing when compared to D^* .

$$D^e = \frac{v^3}{2m_0} \frac{\partial \langle m_{2c} \rangle}{\partial x} \quad (2.59)$$

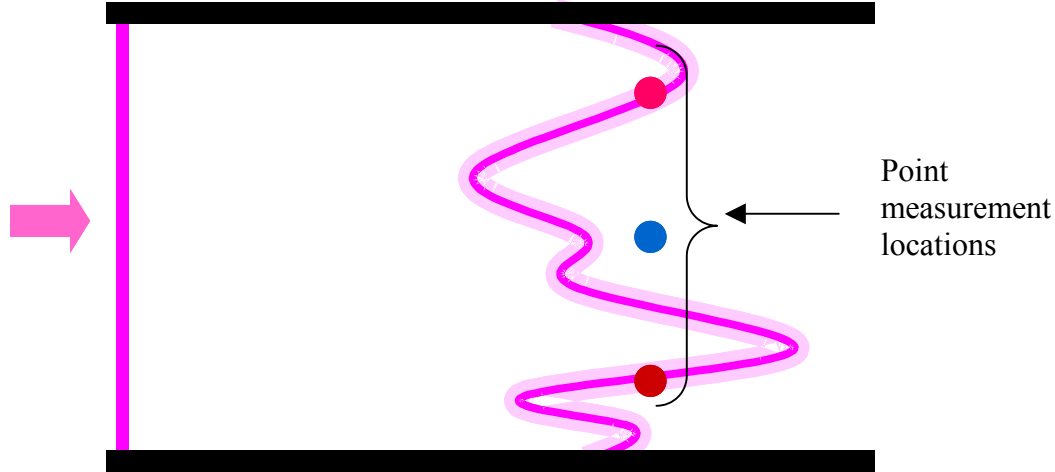


Fig 2.4 Measuring plume concentrations at several points across a control plane

In the paper, a relationship is derived between second central moment calculated from cross-sectional averaged concentration m_{2c}^* and cross-sectional average of the second central moments calculated from the point concentration measurements $\langle m_{2c} \rangle$ (eq. 2.60). According to the paper, the term in the left-hand side corresponds to macrodispersion, while the first and second terms in the right-hand side are measures for dilution and spreading, respectively.

$$m_{2c}^* = \langle m_{2c} \rangle + \frac{\sigma_{m1}^2}{m_0} \quad (2.60)$$

in which σ_{m1}^2 is the variance of the first moment m_1 .

2.5.3.2 Relevant parameters derived from temporal moments, and their physical meaning

In the paper, relationships between relevant parameters and temporal moments, as well as their physical meanings are given. The apparent velocity v_a , the apparent diffusion coefficient of mixing D_a , the apparent dispersivity of mixing α_a , and the apparent Peclet number of mixing Pe_a derived from temporal moments for the quasi one-dimensional case is given as,

$$v_a = \frac{x_1 m_0}{m_1} \quad (2.61)$$

$$D_a = \frac{m_{2c} v_a^3}{2m_0 x_l} = \frac{x_l^2 m_{2c} m_0^2}{2m_l^3} \quad (2.47)$$

$$\alpha_a = \frac{D_a}{v_a} = \frac{x_l m_{2c} m_0}{2m_l^2} \quad (2.62)$$

$$Pe_a = \frac{v_a x_l}{D_a} \quad (2.63)$$

in which x_l is the mean direction of flow. The above quantities are called apparent, because they were defined from equations of one-dimensional transport with uniform coefficients, although the actual transport is multi-dimensional and heterogeneous. Here v_a is the path-averaged seepage velocity in the x_l direction, and D_a describes the average mixing the tracer has undergone while being transported to the point of observation, and α_a is the ratio of these quantities.

The physical meaning of the local and integrated temporal moments is summarized in Table 2.2. Values within angle brackets are averaged over a cross section perpendicular to the direction of the flow. Primed values are the local deviations from the average. Parameters are inferred from both the local and the integrated moments. Those with index a are apparent parameters evaluated from the point measurements, whereas parameters with superscript ‘*’ are macroscopic quantities evaluated from the spatially integrated breakthrough curve. The second central temporal moment of the spatially integrated breakthrough curve yields an estimate of the field-scale dispersion or the macrodispersion D^* , whereas $\langle D_a \rangle(x_l)$ calculated from second central moments calculated from locally obtained breakthrough curves reflects the average mixing.

Table 2.2 Physical meaning of local and integrated temporal moments (*Cirpka and Kitanidis, 2000a*)

Identities	Physical Meaning
$\frac{m_1}{m_0} = \frac{x_1}{v_a(x_1)}$	Local breakthrough time
$\frac{\langle m_1 \rangle}{m_0} = \frac{x_1}{v^*(x_1)}$	Average breakthrough time
$\frac{\sigma_{m_1}^2}{m_0^2}$	Spatial variance of the breakthrough time
$\frac{m_{2c}}{m_0} = \frac{m_2}{m_0} - \frac{m_1^2}{m_0^2} = \frac{2x_1 D_a(x_1)}{v_a^3(x_1)}$	Local dilution
$\frac{\langle m_{2c} \rangle}{m_0} = \frac{\langle m_2 \rangle}{m_0} - \frac{\langle m_1 \rangle^2}{m_0^2} - \frac{\sigma_{m_1}^2}{m_0^2}$	Average dilution
$\frac{\langle m_2 \rangle}{m_0} - \frac{\langle m_1 \rangle^2}{m_0^2} = \frac{\langle m_{2c} \rangle}{m_0} + \frac{\sigma_{m_1}^2}{m_0^2} = \frac{2x_1 D^*(x_1)}{v^{*3}(x_1)} = \frac{2x_1 \alpha^*(x_1)}{v^{*2}(x_1)}$	Macrodispersion
$\frac{\sigma_{m_{2c}}^2}{m_0^2} = \frac{\sigma_{m_2}^2}{m_0^2} + 2 \frac{\langle m_2'(m_1^2)' \rangle}{m_0^3} + \frac{\langle (m_1^2)'^2 \rangle}{m_0^4} + \frac{\sigma_{m_1}^4}{m_0^4}$	Spatial variance of dilution
$\frac{2m_1^2}{m_{2c}m_0} = Pe_a$	Apparent Peclet number of mixing

2.5.3.3 Major conclusions

They concluded that macrodispersion coefficient is a function of the travel distance near the inflow boundary, and it reaches a constant value after travelling distances much larger than the integral scale of the conductivity distribution. It was also observed that the variance of the arrival time increases near the inflow boundary and approaches a constant value for large travel distances, where the variance destruction balances its production. Although the variance of the first temporal moment is not a direct measure for spreading, it represents the uncertainty in arrival time.

Stochastic analysis, both in the Eulerian (*Gelhar and Axness, 1983*) and in the Lagrangian framework (*Fiori, 1996*), has shown that local scale dispersion has only a minor impact on longitudinal macrodispersion for most field situations.

Cirpka and Kitanidis, 2000a, found that at large travel distances, the transport equation of the second central temporal moment of the spatially integrated breakthrough curve is identical to the transport equation of the expected value of the locally observed second central moment. Therefore the rates of change of m_{2c}^* and $\langle m_{2c} \rangle$ become identical at large distances and $\sigma_{m_1}^2$ approaches a constant value. Since m_{2c}^* hardly depends on local-scale dispersion, $\langle m_{2c} \rangle$ also becomes independent of local dispersion at this limit. However, the characteristic timescale to reach this state is controlled by local-scale dispersion.

It was also found that the apparent dispersivity of mixing α_a , equals the local-scale longitudinal dispersivity at very small distances, increases much slower than the macrodispersivity α^* with distance, and finally converges to α^* at very large distances.

2.6 System Considered in the Thesis

In this thesis, an attempt is made to quantify dilution and mixing, and thereby distinguish it from macrodispersion using local temporal moments of a conservative tracer test following the concepts mentioned in *Cirpka and Kitanidis, 2000a*. The locally obtained conservative tracer breakthrough curves, which also carry the information on tracer dilution, are then used to predict reactive mixing between two compounds at those points. In order to predict reactive mixing, additional information on reaction between the considered compounds were acquired through batch tests. The reactive mixing predicted from a conservative test was then compared with an actual dispersion-controlled reactive transport test. The tests were first carried out in a homogeneously packed one-dimensional sand column before conducting them in a heterogeneously packed sandbox.

2.6.1 Conservative tracer test

In the conservative test, a conservative tracer is continuously and homogeneously introduced along the inflow boundary into a water-saturated domain.

$$\frac{\partial c}{\partial t} + \mathbf{v} \cdot \nabla c - \nabla \cdot (\mathbf{D} \nabla c) = 0 \quad (2.23)$$

where c is the tracer concentration, t is the time, \mathbf{v} is the seepage velocity, and \mathbf{D} is the dispersion coefficient tensor.

Here α_L and α_T are the local-scale longitudinal and transverse dispersivities, respectively; v without index is the absolute value of the seepage velocity, δ_{ij} is the Kronecker delta which equals unity for $i = j$ and zero otherwise, and D_d is the molecular diffusion coefficient.

The initial concentration within the domain is zero,

$$c(x_i) = 0 \quad \text{at } t = 0 \quad (2.64)$$

Since the tracer is continuously and homogeneously introduced into the domain over the inflow boundary at $t = 0$, the flux concentration c^{in} in the inflow is uniformly distributed over the inflow boundary.

$$n_i v_i c - n_i \left(D_{ij} \frac{\partial c}{\partial x_j} \right) = n_i v_i c^{in} \delta(t) \quad \text{at } \Gamma_{in} \quad (2.65)$$

$$\text{and } \begin{cases} c^{in} = 0 & \text{for } t < 0 \\ c^{in} = 1 & \text{for } t \geq 0 \end{cases} \quad (2.66)$$

where n_i is the normal unit vector pointing outward of the domain.

If the hydraulic conductivity were homogeneous, the system with the given boundary and initial conditions could be described using a one-dimensional model. Hence a reasonable macroscopic description of a heterogeneous case is also one-dimensional and such a two-dimensional problem could be referred as quasi one-dimensional.

2.6.2 Reactive tracer test

In the thesis, reaction due to dispersive mixing in an aquifer with only physical heterogeneities is studied. I consider a homogeneous, instantaneous, irreversible, bimolecular reaction yielding a single product.



The reaction rate in such a case is defined as the rate of change of the concentration of the reactant or the product:

$$\frac{\partial c_A}{\partial t} = -\gamma c_A c_B \quad (2.68a)$$

$$\frac{\partial c_B}{\partial t} = -\gamma c_A c_B, \text{ and} \quad (2.68b)$$

$$\frac{\partial c_C}{\partial t} = \gamma c_A c_B \quad (2.68c)$$

where c_A , c_B and c_C are the concentration of the compounds A, B, and C, respectively. Here γ is the rate coefficient of the bimolecular reaction. Since the reactants are depleted in a reaction, there is a negative sign associated with their reaction rates while those of the product have a positive sign.

Considering advective-dispersive transport of the compounds A, B, and C, the governing partial differential equations are

$$\frac{\partial c_A}{\partial t} = -\frac{\partial}{\partial x} \left(v c_A - D \frac{\partial c_A}{\partial x} \right) - \gamma c_A c_B \quad (2.69a)$$

$$\frac{\partial c_B}{\partial t} = -\frac{\partial}{\partial x} \left(v c_B - D \frac{\partial c_B}{\partial x} \right) - \gamma c_A c_B \quad (2.69b)$$

$$\frac{\partial c_C}{\partial t} = -\frac{\partial}{\partial x} \left(v c_C - D \frac{\partial c_C}{\partial x} \right) + \gamma c_A c_B \quad (2.69c)$$

At the initial state, the domain is saturated with compound A, and neither B nor C are present.

$$c_A(t_0, x_i) = 1 \quad c_B(t_0, x_i) = 0 \quad c_C(t_0, x_i) = 0 \quad (2.70)$$

Then compound B is homogeneously introduced along the inflow boundary into the domain as a continuous input.

$$n_i v_i c_B - n_i \left(D_{ij} \frac{\partial c_B}{\partial x_j} \right) = n_i v_i c_B^{in} \delta(t) \quad \text{at } \Gamma_{in} \quad (2.71)$$

$$\text{and } \begin{cases} c_B^{in} = 0 & \text{for } t < 0 \\ c_B^{in} = 1 & \text{for } t \geq 0 \end{cases} \quad (2.72)$$

At the mixing interface where the compound B reacts with compound A, the product C is formed. The breakthrough curves of the product concentration are obtained as point measurements, and their temporal moments are calculated and compared with that predicted from the conservative breakthrough curves.

3 REVIEW OF LABORATORY TRACER TESTS TO DETERMINE SOLUTE TRANSPORT IN POROUS MEDIA

The chapter is divided into the following sections:

- A brief review of existing laboratory methods to determine flow and transport properties in porous media,
- A short description of a few laboratory- and technical-scale tracer experiments conducted in homogeneous and heterogeneous porous media,
- Some details about a few experiments that are comparable to the undertaken research.

I request that the title of the chapter should not be misunderstood for a review of all laboratory experiments carried out to study transport parameters, instead only tracer experiments that are relevant and or comparable to the research addressed in this study are considered.

3.1 Laboratory Methods to Determine Flow and Transport Properties in Porous Media

Laboratory methods used to address flow and solute transport issues in porous media could be generally classified as

- Probe methods,
- Nuclear Magnetic Resonance Imaging (NMRI) technique,
- Dye tracer imaging,
- Computed Tomography (CT) techniques, and
- Photoluminescent Volumetric Imaging (PVI).

In probe methods, a tracer solution is passed through the porous medium and the tracer concentrations are measured using a probe that is either placed within the porous medium or at the outflow tube (*Bear, 1961; Robbins, 1989*). The tracer used in the study could be a salt, a fluorescent dye, or even biological or nuclear tracers.

For magnetic resonance imaging of transport in porous media, paramagnetic tracers are used (*Greiner et al., 1997*). This method is a non-invasive method for determining transport properties and also yields three-dimensional data. Flow and transport processes in porous media were visualized by using a paramagnetic salt as a tracer (*Pearl et al., 1993; Guillot et al., 1991; Gaigalas et al., 1989*).

In the dye tracer imaging technique, a dye is passed through the porous medium and images of the development of the dye plume in the medium is captured either using a photo

camera or a video camera and the data is later analyzed using image analyzers (*Corapcioglu and Fedirchuk, 1999; Jia et al., 1999; Lajeunesse et al., 1999, Schäfer, 1990*).

Computed tomographic (CT) techniques are also employed in studying solute transport in porous media (*Keller et al., 1995; Khalili et al., 1998; Tidwell and Robert, 1995*). Computed tomography (CT) uses special x-ray equipment to obtain many images of the experimental setup from different angles, and then reconstruct the mass distribution within the domain. This technology has been widely used in medical science to capture images of the internal organs.

In photoluminescent volumetric imaging (PVI) techniques, a transparent porous medium is used as the experimental setup. It is then normally filled with a fluid whose refractive index matches that of the porous medium. A fluorescent tracer is then passed through the medium and it is excited using either a UV light or laser beam. The resulting illumination from the tracer is recorded by a high resolution charged-coupled device (CCD) camera. These types of imaging techniques were used by *Montemagno and Gray (1995), Gramling et al., (2002)* besides some others.

The above mentioned classification of methods is not a strict one and therefore a combination of above methods or slight variations from the said procedures may be found in published results.

3.2 Tracer Experiments in Homogeneous and Heterogeneous Porous Media

In this section, general information on some selected tracer studies are given. Table 3.1 provides necessary information on experiments conducted in homogeneous porous media, and Table 3.2 provides required details about experiments in heterogeneous porous media.

Table 3.1 Relevant information on some tracer experiments in homogeneous porous media

Authors	Method	Setup Geometry	Setup Dimensions	Grain Material	Grain Size	Tracer
<i>Bruch, 1970</i>	Probe method	Rectangular box	152.4×60.96×12.7cm ³	Sand	1.21mm	Sodium chloride
<i>Nielsen et al., 1991</i>	Probe method	Cylindrical column	∅ = 0.1m length = 1m	Glass beads	3mm	Sodium fluorescein
<i>Rashidi et al., 1996</i>	Photoluminescent volumetric imaging	Cylindrical column	∅* = 4.5cm; length = 23.5 cm	Polymethyl methacrylate beads	0.31cm	Fluorescent latex microspheres
<i>Gheith and Schwartz, 1998.</i>	Dye tracer imaging; Probe method	Rectangular box	90×50×50cm ³	Flint silica	300-425μm	Rhodamine WT; NaCl
<i>Corapcioglu and Fedirchuk, 1999.</i>	Dye tracer imaging	Rectangular box	77.5×36.12×1.25mm ³	Pyrex glass beads	1.248±9% mm	Food color McCormik
<i>Ghodrati, 1999.</i>	Probe method	Cylindrical column	∅ = 5cm length = 20cm	Silica sand;; Sandy soil; Clay loam soil.	0-2mm	Sodium fluorescein; Pyranine.

Authors	Method	Setup Geometry	Setup Dimensions	Grain Material	Grain Size	Tracer
<i>Raje and Kapoor, 2000</i>	Spectrophotometer used at the outflow tube	Cylindrical column	$\varnothing = 4.5\text{cm};$ length = 18 cm	Glass beads	1.5mm	Aniline; 1,2-naphthaquinone-4-sulfonic acid
<i>Gramling et al., 2002.</i>	Photoluminescent volumetric imaging	Rectangular box	36×5.5×1.8cm ³	Cryolite grains	1.19-1.41mm	Copper complexes
<i>Huang et al., 2002.</i>	Photoluminescent volumetric imaging	Rectangular box	180×280×10mm ³	Glass beads	60-100μm	Sodium fluorescein
<i>Nakashima and Watanabe, 2002.</i>	Computed tomography	Cylindrical column	$\varnothing = 18\text{mm}$	Glass beads	2.11±0.06mm	Iodine
<i>Huang et al., 2003</i>	Photoluminescent volumetric imaging	Rectangular box	156×120×3mm ³	Quartz sand	212-300μm	Sodium Fluorescein; Ru(phen) ₃ Cl ₂

*inner diameter

Table 3.2 Relevant information on some tracer experiments in heterogeneous porous media

Authors	Method	Setup Geometry	Setup Dimensions	Grain Material	Types of heterogeneity	Tracer
<i>Silliman and Simpson, 1987</i>	Probe method	Rectangular box	2.4×1.07×0.1m ³	Sand	Structured	Sodium chloride
<i>Haselow and Greenkorn, 1991</i>	Probe method	Rectangular boxes	10-40×10-40×1cm ³	Glass beads	Structured	Sodium chloride
<i>Bajracharya and Barry, 1997</i>	Probe method	Cylindrical columns	∅ = 4.4-30cm length = 2.7-13.9cm	Fine silt and polyethylene cylinders	Random packing	Sodium chloride
<i>Delay et al., 1997</i>	Probe method	Cylindrical column	∅* = 5cm; length = 60-120 cm	Silica beads and Catsan	Structured heterogeneity	Fluorescein
<i>Greiner et al., 1997.</i>	Nuclear magnetic resonance imaging	Cylindrical column	∅ = 19cm; length = 28.2 cm	Glass beads	Structured	Paramagnetic salt
<i>Murphy et al., 1997</i>	Hydraulic tomography	Rectangular box	0.8×0.5×0.032m ³	Sand	Structured; Nature-like	Chloride ions
<i>Cirpka et al., 1999</i>	Probe method	Rectangular box	10.10m×0.7m×0.2m	Sand	Structured	Sodium chloride; PCE ¹

Authors	Method	Shape of the Porous Medium	Dimensions of the Setup	Grain Material	Types of heterogeneity	Tracer
<i>Chao et al., 2000</i>	Probe method	Rectangular box	2.44×1.22×0.064m ³	Sand	Structured	Potassium bromide
<i>Barth et al., 2001</i>	Probe method	Rectangular box	10m×1.2m×0.06m	Sand	Structured	Bromide; tritium
<i>Silliman et al., 2001</i>	Probe method	Rectangular box	1.6×0.67×0.094m ³	Sand	Structured	Sodium chloride
<i>Silliman and Zheng, 2001</i>	Probe method	Rectangular box	1.6×0.67×0.094m ³	Sand	Structured	Sodium chloride
<i>Ursino et al., 2001a</i>	Photoluminescent volumetric imaging	Rectangular box	75×40×5cm ³	Sand	Structured	Brilliant Sulfaflavine
<i>Levy and Berkowitz, 2003.</i>	Probe method	Rectangular box	86×45×10cm ³	Quartz sand	Random packing; Exponentially correlated structure	Sodium chloride

* inner diameter
¹ polychloroethylene

3.3 Experiments Comparable to the Undertaken Research

In my thesis, I conduct experiments in one- and two-dimensional experimental setups. The one dimensional experimental setup consists of a 2m long polyvinyl chloride column with an inner diameter of 10cm. The column is filled with coarse sand. The quasi-two dimensional experimental system consists of a large sandbox with dimensions, 14m×0.13m×0.5m. The sandbox is filled heterogeneously with four types of sand. I calculate the transport parameters, and estimate the dilution of the tracer in the porous media from the experiments. In addition, it is checked whether reactive mixing could be accurately predicted from conservative test results in the respective porous media. The applicability of some of the existing numerical and theoretical developments regarding dilution and reactive mixing in porous media is also checked simultaneously. In this section, only experiments that are comparable, either due to their objectives or due to their scales, to the experiments undertaken in the framework of the thesis are discussed.

There are many experiments conducted in experimental porous media from which transport parameters have been derived (most of the experiments mentioned in 3.2). But only a few experiments have dealt with dilution and reactive mixing in porous media following the theory considered in this study.

Beginning with homogeneous experimental setups that could be compared with my study, there are only two experiments with direct relevance – one from *Raje and Kapoor (2000)* and the other from *Gramling et al., (2002)*. In both experiments, they aimed in predicting the formation of reaction product in a reactive-mixing experiment from pore-scale dispersion coefficients derived from conservative studies. *Raje & Kapoor (2000)*, performed an experiment in which solutions of dissolved aniline and 1,2-naphtoquinone-4-sulfonic acid replaced each other in a 18 cm long column. The two reactants and the reaction product, 1,2-naphtoquinone-4-aminobenzene, were measured in the outflow of the column in a flow-through spectrophotometer cuvette. In the experiment of *Gramling et al. (2002)*, sodium EDTA and copper sulfate are used as reactants in a transparent, quasi two-dimensional device with dimensions of 36cm × 5.5cm. The reaction product, CuEDTA, was detected throughout the domain by light-transmission imaging. The experiment, however, was restricted to a travel distance of 36cm, which is about five times smaller than the column setup used in my study.

There are only a few intermediate to large-scale sandbox tracer studies on solute dispersion, that could be compared with the scale of the sandbox setup in my study (*Silliman and Simpson, 1987; Murphy et al., 1997; Chao et al., 2000; Silliman et al., 1998; Silliman et*

al., 2001; Silliman and Zheng, 2001; Ursino *et al.*, 2001a, b). Silliman *et al.* (1998) give an overview over older intermediate-scale experiments. Some of these studies involve heterogeneously packed setups, but heterogeneities were introduced by blocks of different sand types, choosing either simple deterministic block structures or randomly generated indicator fields. Great care was taken to make the blocks themselves as homogeneous as possible.

In Murphy *et al.*, (1997), a heterogeneously packed sandbox with dimensions $1\text{m} \times 0.2\text{m} \times 0.1\text{m}$ was used to study the influence of physical heterogeneity on microbial distribution and degradation. The difference between field dispersivities estimated from uniform and non uniform flow tracer tests is reported in Chao *et al.*, (2000) based on intermediate-scale experiments and numerical simulations in two-dimensional heterogeneous porous media ($2.44\text{m} \times 1.22\text{m} \times 0.06\text{m}$). Silliman *et al.*, (2001) investigated bacterial transport in a heterogeneous porous medium ($1.6\text{m} \times 0.67\text{m} \times 0.09\text{m}$). The sandbox was packed in such a way that the hydraulic conductivity varied according to a two-dimensional, log normally distributed, second order stationary, exponentially correlated random field. Silliman and Zheng (2001) conducted hydraulic and tracer experiments in the heterogeneous medium of Silliman *et al.*, (2001), and the results were compared with the solutions presented by Dagan (1984, 1987). They reported that the observed rate of longitudinal spread of tracer plumes was slightly less than that predicted using the theory. They also observed that the spread in the transverse direction declined from the initial plume dimensions and then either remained constant or slightly increased, but at a rate lower than predicted by the theory.

Dilution of non-reactive tracers in variably saturated sandy structures was studied in a sandbox with dimensions $0.75\text{m} \times 0.4\text{m} \times 0.05\text{m}$ (Ursino *et al.*, 2001a). The experimental system is quasi two-dimensional with random, heterogeneous and anisotropic structures. The plume spreading and mixing in the experimental setup was quantified based on coefficient of variance of concentration (Kapoor and Gelhar, 1994a; Kapoor and Kitanidis, 1996) and the dilution index (Kitanidis, 1994). The first and second moments of small plumes traveling through the same setup is analyzed in Ursino *et al.*, (2001b).

As can be seen from the above discussion, my sandbox experiments is reportedly one of the pioneer steps in estimating dilution from point-like measurements in a natural-like heterogeneous porous medium, and that too in a technical scale experimental setup.

4 MATERIALS AND EXPERIMENTAL SETUPS

In this chapter, I give a description of all the materials and the setups that are employed to conduct the experiments. The chapter is divided into the following three main sections:

- Point-measurement system,
- Tracer,
- Experimental setups.

4.1 Point Measurement System

The theory of *Cirpka and Kitanidis, (2000a)* on local temporal moments as measure for solute dilution is based on concentrations obtained at single points within the porous medium. Hence, the verification of the theory requires that the tracer concentrations can be measured in minimal volumes directly within the sand package of a physical aquifer model.

Therefore, fiber optic fluorometry has been selected as the point measurement technique. This method is a commonly used technique in laboratory and field-scale experiments for in-situ measurements of fluorescent tracers (*Schmid and Barczweski, 1995*). The main elements of the measurement system are fluorometers, optic fiber probes, and a data acquisition and storage system.

4.1.1 Fluorometer

4.1.1.1 Principle

The fluorometer consists of a light source and a photo multiplier with a current-voltage converter. The light from the light source is transmitted through an optic fiber to the measurement medium. The light stimulates the fluorescent tracer present in the measurement volume and a part of the emitted light from the tracer is then transmitted back to the photo multiplier of the fluorometer by another optic fiber. The photo multiplier, which has a current-voltage converter creates an electrical signal corresponding to the measured light intensity, is connected to a data collecting and processing system. The sketch of the optic fiber fluorometer is given in Fig 4.1.

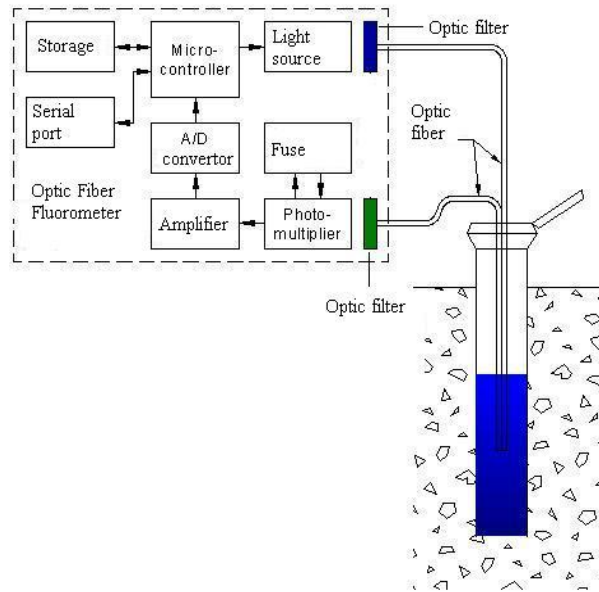


Fig 4.1 Sketch of fiber optic fluorometer (source: www.hermess.de)

4.1.1.2 Description

The fluorometers that I have used (Fig 4.2) were supplied by *Hermes Messtechnik, Germany*. Each fluorometer provides 20 channels for measurement, out of which one channel is used to measure the background intensity so that the intensities measured by the other 19 channels can be adjusted automatically for their background values.

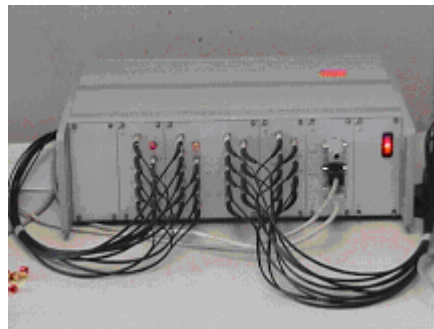


Fig 4.2 Fluorometer

The quality and performance of the obtained fluorometers have been checked by continuously measuring the intensity of a tracer solution for 24 hours. This has been done for each port of the eight fluorometers. The effects due to probable occasional voltage fluctuations are solved by connecting the fluorometers to a voltage-filter.

4.1.2 Optic fiber

4.1.2.1 Description

The optic fiber consists of two distinct and different types of optically conducting materials (Fig 4.3). The center, or core, of the fiber is the portion that actually carries light. It has the higher index of refraction. A thin layer of a material with low index of refraction, called clad, surrounds the core and is fused to the core creating a totally reflecting interface at the junction between them. Depending upon the materials used as core and clad, fibers are classified into glass fibers and polymer fibers. The optic fibers covered by an insulating material are called cables. A single cable is normally called a simplex cable while two cables joined together are denoted a duplex cable.

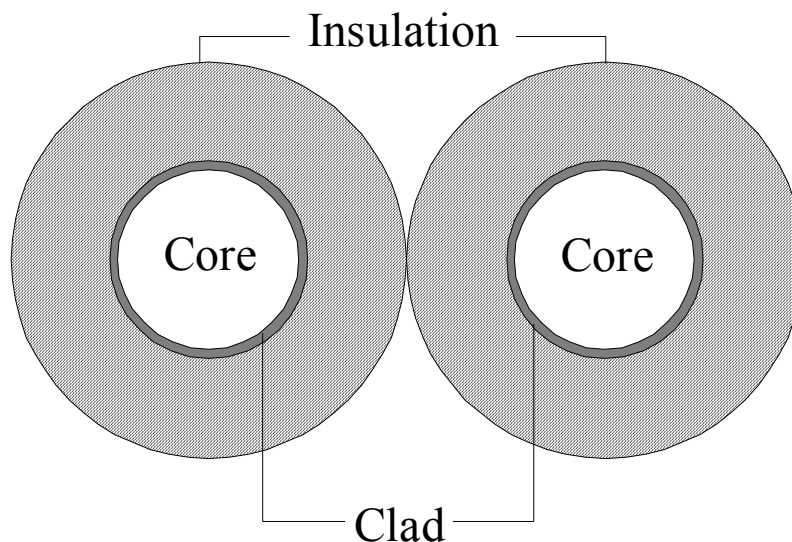


Fig 4.3 Duplex polymer optic fiber cable

4.1.2.2 Sensitivity of duplex cables

Probes used in this study are prepared from duplex cables provided by *DIS, Netherlands*, as they exhibited good performance during the sensitivity tests for tracer fluorescence conducted in the laboratory. For a duplex cable connected to a fluorometer, one of the cables carries the excitation light while the other carries the fluorescence light. The fluorescent tracer molecules present in the beam of the excitation light excites and emits fluorescence light (Fig 4.4, left). The measurement volume, which is the volume having both excitation and fluorescent light, determines the sensitivity of the probes. Sensitivity of a standard duplex cable could be increased by increasing the measurement volume. This could be done by joining the two fibers by removing their individual insulations from their tips (Fig 4.4, right). From several

methods experimented to join the fibers at the tip, a method using heat-shrinkable tubes is used in the preparation of the probes.

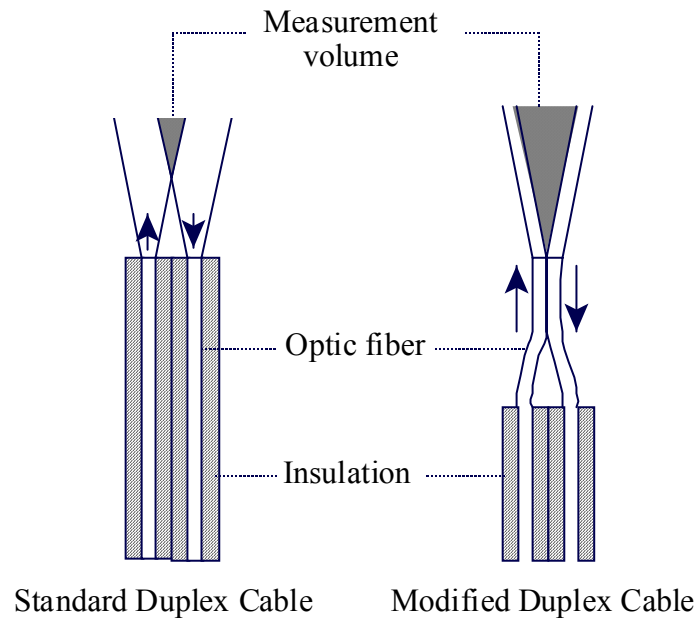


Fig 4.4 Measurement volume of standard and modified duplex cables. Note that the modified duplex cable has large measurement volume.

4.1.2.3 Preparation of the probes

The selected polymer duplex cables are cut to the required probe lengths. For each severed cable, the fibers are separated for a length of 8cm at one of their ends. The insulation of the separated fibers are then stripped off to a length of 6cm. The naked fibers are then inserted together into a heat-shrinkable tube of 6cm length. The diameter of the tube before and after shrinking is 2.4mm and 1.2mm, respectively. The tubes are then shrunk by evenly blowing hot air (temperature = 90°C) over the tubes. Since the gap that exists between the joints of the fiber insulation and the shrunk tube may provide passage for water during experiments, another shrinkable tube of length 2cm and different dimensions (diameter before/after shrinking = 4.8mm / 2.4mm) is placed at the joints and shrunk. A hot liquid-glue is applied at both ends of the second shrinkable tube to prevent leakage of water through any openings. For double safety another shrinkable tube with length 4cm and same shrinking properties is shrunk above the second shrunk tube. The ends of the third shrinkable tube are also closed by applying hot liquid-glue. This prevents the probes from leaking during the experiments. The modified tip has a diameter of 2.5mm compared to the original tip diameter of 4.4mm (Fig 4.5), and will serve as the measurement tip of the probes. The heat-shrinkable tubes were bought from *RS Components, Germany*.

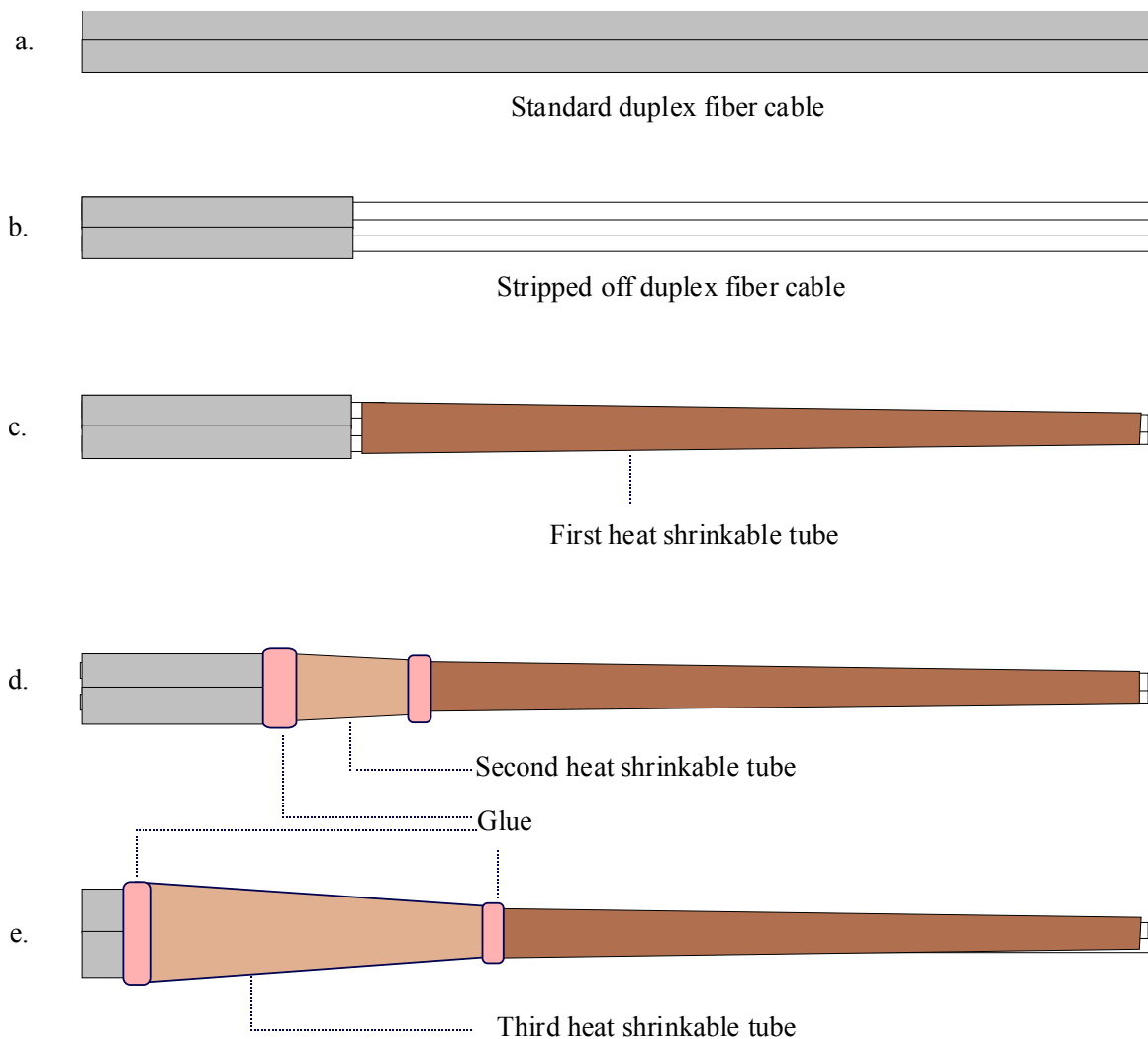


Fig 4.5 Modification of duplex polymer cables to probes a) original duplex polymer optic fiber cable. b) cable insulation stripped for 6 cm. c) individual fibers joined by heat shrinkable tube. d) the joint between the cable insulation and shrunk tube closed by another heat shrinkable tube. e) one more heat shrinkable tube put on the top of the tube closing the joint between the insulation and shrunk tube.

The other end of the severed cables is then modified to connect it to the fluorometer ports. The fibers of the duplex cable at the said end are separated to a length of 5 cm. The insulation of each fiber is then removed for 1 cm from the tip. An SMA connector is connected to each fiber tip with 1 mm of the naked fiber protruding from the connectors. This end is to be connected to the fluorometer ports.

Both ends of the probes have been polished using polishing papers of rough ($30\ \mu\text{m}$), medium ($5\ \mu\text{m}$) and fine ($0.3\ \mu\text{m}$) ranges in order of first use. It is necessary to polish the tips to remove damages that may have happened during the severing of the cables. The quality of each prepared probe is later checked by measuring its sensitivity to a standard tracer solution. The less sensitive probes, if any, are rectified, remade or replaced.

4.1.3 Data acquisition system

The fluorimeters were connected to personal computers by a CAN bus. Data acquisition and storage is done by a special software from the provider of the fluorimeter.

4.2 Tracer

4.2.1 Requirements

4.2.1.1 Experimental requirements

The tracer experiments within the thesis framework are generally classified into two types: conservative tests, and reactive tests.

In a conservative test, a conservative tracer solution is passed through a water- saturated porous medium and its concentration breakthrough curves are obtained at different locations within the medium and in the outflow.

In a reactive test, a solution of some compound B is passed through a porous medium saturated with a solution of another compound A. At the interface where the solutions B and A mix, they react to form a product C, whose concentration breakthrough curves are measured.

4.2.1.2 Tracer requirements

The conservative tracer and the reaction product C in the reactive test should be fluorescent since we employ fiber optic fluorimetry for data acquisition. Neither compound A nor B in the reactive case should be fluorescent. The selected tracers should be non-toxic, stable (not easily degradable during the tests) and within the financially affordable limits.

4.2.2 Selected tracer: fluorescein

The sand used in all experiments are silica sand with different grain size distribution. Fluorescein (Fig 4.6) is reported as a good conservative fluorescent tracer in silica sand (*Smart and Laidlaw, 1977; Kasnavia et al., 1999*), and therefore is selected as the tracer for conservative tests.

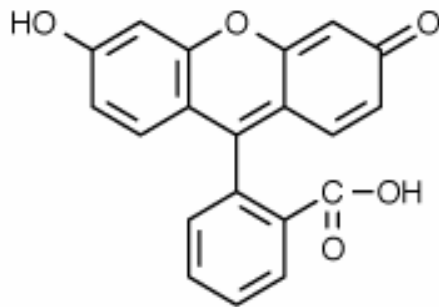


Fig 4.6 Structure of fluorescein (source: www.probes.com)

As mentioned earlier, in reactive tests a fluorescent tracer that is formed as the result of a reaction between two non-fluorescent compounds is needed. It has been reported that fluorescein has low fluorescence intensity at low pHs ($\text{pH} < 5$) and high fluorescence intensity at high pHs ($\text{pH} > 8$) (*Smart and Laidlaw, 1977*). This property of fluorescein is utilized in order to use fluorescein as the reactive tracer for the reactive tests.

Properties of fluorescein are given in (Table 4.1). Emission and absorption spectra of fluorescein are given in (Fig 4.7). *Smart and Laidlaw (1977)* reported that the intensity of fluorescein is pH dependent and is relatively stable above pH7. We have confirmed these findings by conducting batch tests, the results of which are given in Fig 4.8. The change in fluorescent intensity is attributed to the formation of different structures of the tracer associated with pH changes (*Smart and Laidlaw, 1977; Wang et al., 2001; Behrens, 1988*). Fluorescein (Fig 4.6) contains two functional groups that can be protonated/deprotonated. The phenolic group and the carboxyl group has a pK_a value of 6.4 and 5.1, respectively. The pK_a value is the pH where half of the functional groups are neutralized and half remain ionic. At one unit above or below the pK_a the functional groups are predominantly in the ionic and neutral form, respectively. The phenolic group can further be protonated to a H_2O^+ group with a pK_a of 2.1. That is, for pH values between 2 and 5, the neutral species dominates. This species does not exhibit fluorescence, whereas the monoanion and the dianion fluoresce (quantum yield 0.37 and 0.97, respectively). Fluorescein is also considered to be non-toxic (*Smart and Laidlaw, 1977; Smart, 1984*) and has high photodegradability rates (*Smart and Laidlaw, 1977*).

Table 4.1 Properties of Fluorescein

Mol. Formula	Mol. Weight	pKa	Solubility in water	Excit/Emit wavelength
C ₂₀ H ₁₂ O ₅ ^a	332.31 ^a	5.1 ^b	25 g/l ^c	490/520

^awww.probes.com
^bKasnavia (1997)
^cGasper (1987)

Although sorption of fluorescein to minerals with positive surfaces are well established it was supposed to have moderate or negligible sorption to silica surfaces at neutral and alkaline pHs (*Kasnavia et al., 1999; Sabatini, 2000; Sabatini and Austin, 1991; Smart and Laidlaw, 1977*).

The sorption of a fluorescent tracer depends upon the minerals present in the media, the tracer functional groups, and the environmental conditions (e.g., the pH of the system) (*Kasnavia et al, 1999*).

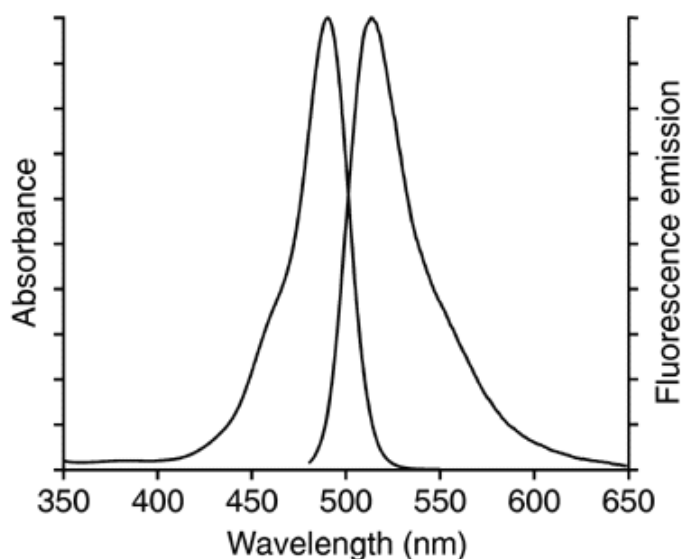


Fig 4.7 Absorption and emission spectra of fluorescein in pH 9.0 buffer (www.probes.com)

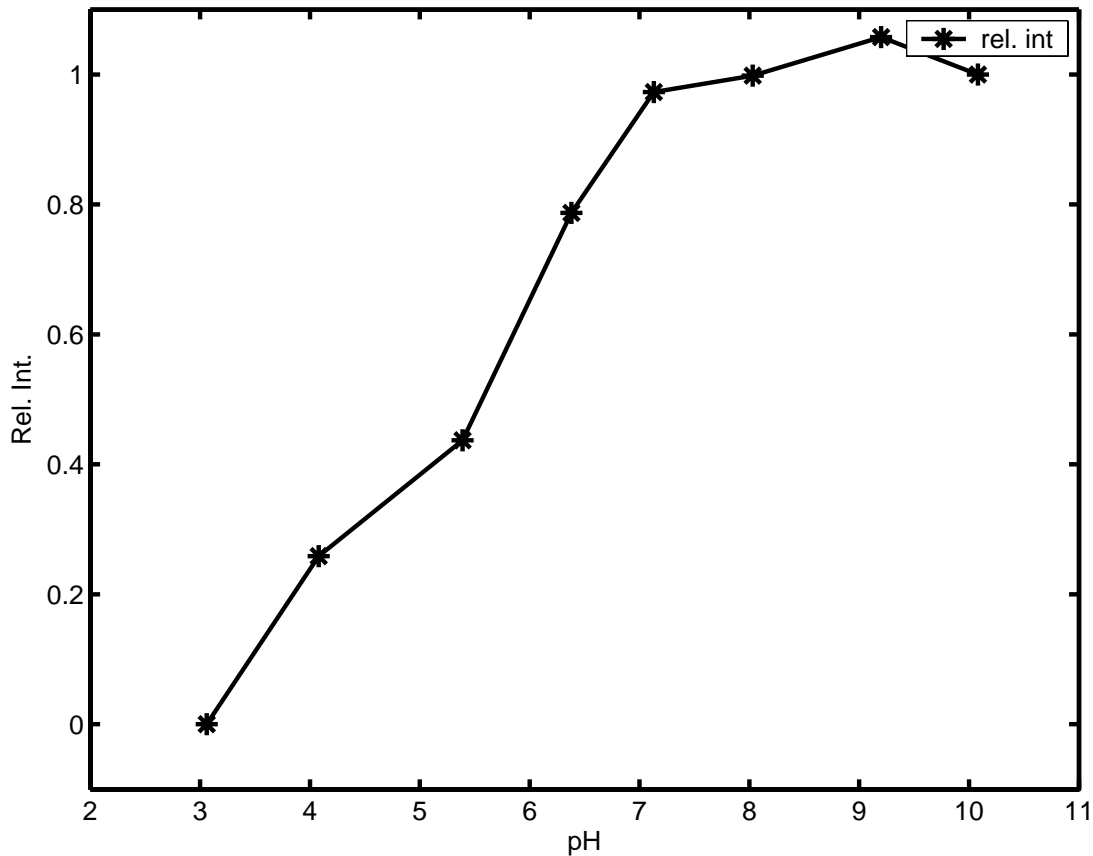


Fig 4.8 pH dependency of fluorescein intensity (*for test solutions prepared in deionized water*)

Silica sands have a net negative charge at neutral pH. But the charged sites on a medium are pH dependent. The silica sands have a reported zero point charge (ZPC) between 2 and 4 (*Montgomery, 1985*). Zero point charge (ZPC) is the pH at which the mineral has a net neutral charge. But the mineral surface does not undergo discrete charge transition at ZPC (i.e., not all sites become ionic just above or below the ZPC).

The anionic group COO^- in the fluorescein molecule (Fig 4.6) is responsible for both the increased water solubility of the tracer and the decreased tracer sorption due to hydrophobic forces (*Kasnavia et al., 1999*). Since the COO^- group of fluorescein has a pK_a value of 5.1, for tests with low pHs ($\text{pH} < 5.1$) almost all of the anionic functional groups (COO^-) are in neutralized form. This may lead to low solubility of the tracer and thereby the expulsion of it from the water phase to the less polar phase, silica sand, in our case. This, therefore, leads to sorption of fluorescein at low pHs (Fig 4.9).

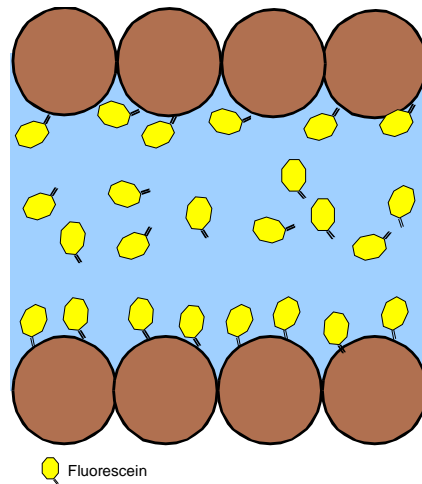


Fig 4.9 Fluorescein sorption at acidic pHs (The circles represent sand grains and the region between them denotes the fluid medium).

4.2.3 Overcoming fluorescein sorption

Several batch tests have been conducted to quantify sorption of fluorescein at different pHs to plan methods to overcome sorption.

4.2.3.1 Quantifying sorption

The amount of sorbed tracer as a function of solution pH and tracer concentration has been studied using batch tests. The pHs used for the study are 2, 3, 4, 5, 6, 7, 8 and 9, and the concentrations used are 10 μ g/l, 50 μ g/l, 200 μ g/l and 500 μ g/l. The sand used for sorption studies is pre-washed silica sand, with an average grain diameter of 0.8mm and grain size distribution between 0.4mm to 2mm, supplied by *Dorfner GmbH, Germany*.

4.2.3.1.1 *Procedure*

Four samples (each of volume 200ml) with above mentioned concentrations are prepared for each pH solution. 150ml of each sample is poured into another bottle with 50g sand and is left for 24 hour stirring. The remaining 50ml of the original sample is brought to pH9, because the fluorescence intensity measurements are done at that particular pH to enable comparison of data and prevention of tracer sorption to fluorometer parts, and is kept in a dark cold room until the sample left for stirring are ready for measurements. Brown-coloured bottles are used for sampling to avoid photodecay of the tracer. After 24 hours, the liquid part of the samples left for stirring are decanted and its pH is also raised to 9. Then, the fluorescence intensity in each sample before and after stirring is measured using a scanning fluorometer. The concentration of each sample is calculated from its intensity using the calibration curve

(Chapter 5, Fig. 5.1). The difference in the concentration gives the amount of tracer sorbed to the sand.

The samples for fluorescence intensity measurements are always passed through a filter into the measurement chamber of the fluorometer to avoid light scattering due to suspended sand particles. The measurements are done at an excitation wavelength of 510nm. The fluorometer used could only measure samples between the range of 0 and 100µg/l. Therefore samples of 200µg/l and 500µg/l are diluted before taking measurements, and then the values are scaled up to account for the actual sorption.

4.2.3.1.2 *Results*

The spectrofluorometer used for the batch test has an intensity measurement accuracy of 1.8%. Calculations done with this measurement accuracy imply that sorption leading to retardation factor, R , less than 1.99 may not be effectively quantified using the fluorometer. Only experiments with pH2 and pH3 yielded sorption in the detectable range, meaning the retardation factors for the tests with pH>3, are less than 1.99 but not necessarily 1. The sorption isotherms for pH2 and pH3 are given in Fig 4.10 and Fig 4.11, respectively.

4.2.3.2 Experiments to overcome fluorescein sorption

Since the major reason for tracer sorption is the low solubility of the tracer in water at low pHs, experiments (both batch and column) with cosolvents (alcohol) and non-ionic surfactants have been conducted to increase the tracer solubility. Cosolvents and surfactants are being used in many groundwater remediation experiments because of their ability to enhance the solubility of non-polar compounds.

Alcohol has a hydroxyl group and an alkyl group. The hydroxyl group guarantees its solubility in water, which is very polar and capable of hydrogen bonding. The alkyl group is non-polar and is incapable of hydrogen bonding. The tracer molecules at low pHs are non-polar and incapable of hydrogen bonding and therefore find the aqueous environment uninviting. But with the addition of the alcohol, the aqueous phase becomes less polar and more inviting for the non-polar tracer molecules.

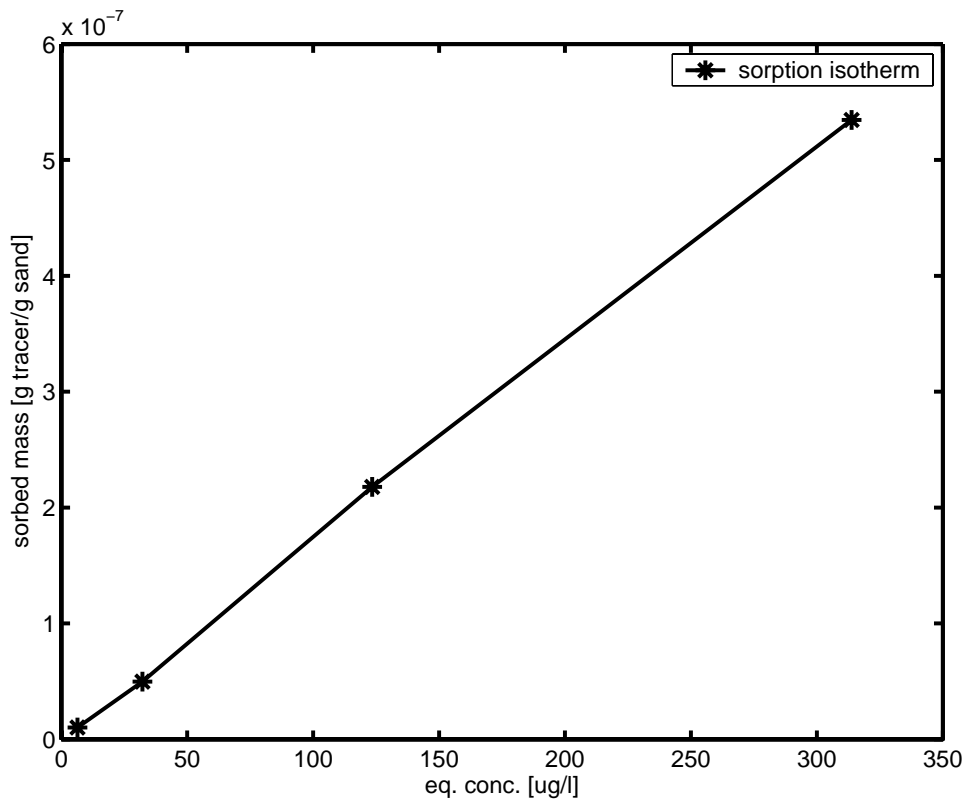


Fig 4.10 Sorption observed at pH2

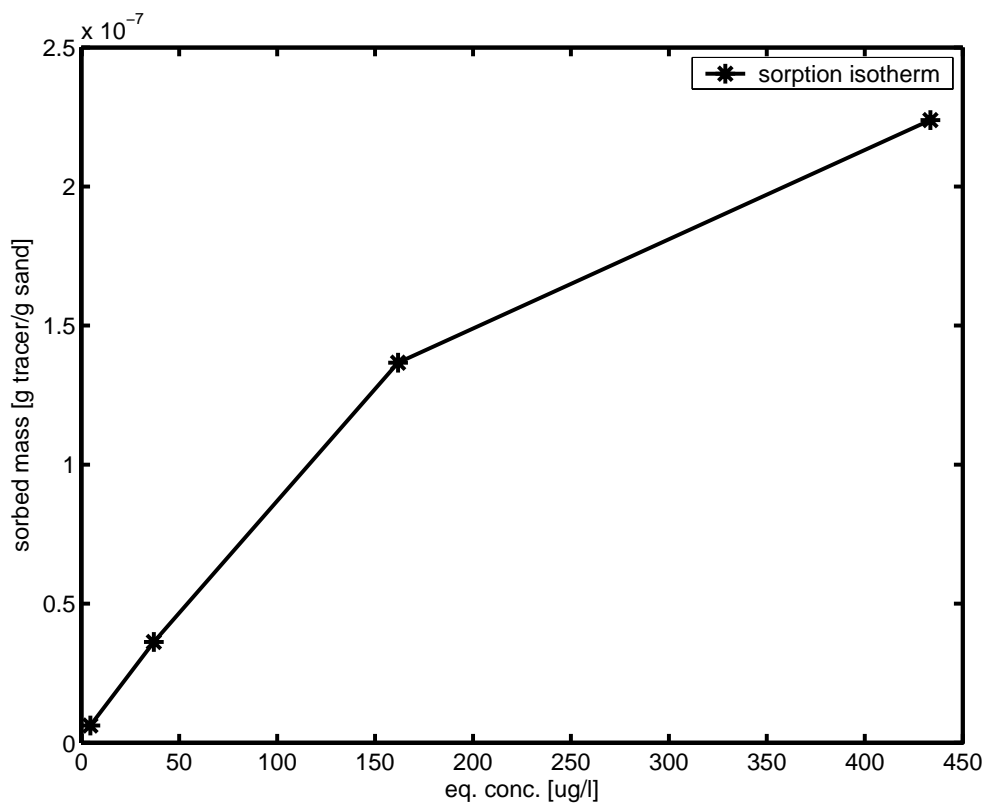


Fig 4.11 Sorption isotherm at pH3

Surfactants have a hydrophilic and a hydrophobic group. Adding surfactant to the aqueous solution will reduce the sorption of fluorescein in the following ways (Fig 4.12).

- Surfactants form a layer on the silica surface with the hydrophobic part attached to the silica surface and the hydrophilic part directed to water. This prevents the tracer from getting attached to the sand surface.
- The non-polar tracer at low pHs gets attached to the hydrophobic tail of the surfactant molecule in water. This will keep the tracer in solution itself.
- The non-polar tracer molecules are entrapped in surfactant micelles and are then transported through the porous medium without being sorbed.

Non-ionic surfactants (surfactants with no charge) are used in my experiments as they are hardly affected by pH changes.

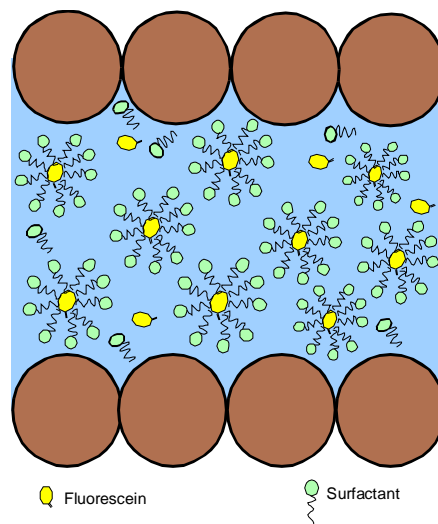


Fig 4.12 Non-ionic surfactants and tracer molecules in acid medium

Isopropanol is the selected alcohol for the tests. The tests have been carried out with an alcohol-water ratio of 60:40. A high percentage of alcohol has been used in order to enhance the nonpolar nature of the liquid medium and thereby prevent the sorption of tracer to the nonpolar sand.

The non-ionic surfactants used for the tests are Lutensit ALBN-50, Lutensit ABO, Lutensol GD-70, and Lutensol AO3. All these surfactants have been manufactured by *BASF AG, Ludwigshafen*. To the best of my knowledge, no experiments to prevent sorption of fluorescein at acidic pHs with non-ionic surfactants have been reported till date. The surfactant concentration used for the tests is 2% of volume of the test solution. This concentration is selected because most of the studies that dealt with remediation of NAPLs used similar concentrations (*Jafvert, 1996; Walker et al., 2000*).

4.2.3.2.1 *Batch tests*

Batch tests have been conducted with alcohol and surfactants to check whether they prevented sorption of fluorescein. The procedure of batch tests is same as given in section 4.2.3.1.1.

4.2.3.2.1.1 Alcohol

The results from batch tests showed that the amount of tracer sorbed in acidic conditions (pH2 and pH3) with alcohol are below the accurate measurement limit of the fluorometer. This clearly indicates that the sorption is reduced with addition of 60% isopropanol, although the actual decrease could not be quantified.

4.2.3.2.1.2 Surfactants

Out of the four selected surfactants, two of them – Lutensit ABO and Lutensol AO3, gave white colour when mixed in water. This may lead to stray intensity measurements. Also they could not be injected into the measuring tube of the fluorometer as they turned to be very bulky in solution. Therefore those surfactants have not been considered further. Sorption tests conducted with the remaining two surfactants for low pHs yielded sorption rates lower than the accurately measurable values. This implies that there has also been a reduction in the sorption of tracer, with the addition of surfactant.

4.2.3.2.2 *Column tests*

The purpose of conducting column tests has been to compare the efficiency of alcohol and surfactant in preventing sorption of fluorescein. A small plexi-glass column (length – 40 cm, diameter – 10 cm) has been used for the study. The sand used is a fine sand (geba) with a grain size distribution between 0.04 mm and 1.1mm and $d_{50} = 0.14\text{mm}$. The hydraulic conductivity (acc. Hazen) is 1.8×10^{-4} m/s and the porosity is 0.4. A fine sand has been used because it provides a large surface area for the tracer to sorb onto and therefore sorption of the tracer would be more prominent. So the effect of using alcohol or surfactant in preventing tracer sorption could be observed more clearly.

The column was homogeneously filled with the sand. The air in the column was displaced by passing, first carbon dioxide and then degassed water. A tracer solution (prepared in deionized water) with pH3 was passed through the column as a step input and the fluorescence intensity breakthrough of the tracer was measured at four different lengths in the column and then at the outlet. Later, tests with tracer solution in an alcohol mixture with same pH were conducted and its intensity measured. The fluorescence intensity could not be measured with the alcohol solution because they reacted with the tips of the optic fiber probes

and damaged them. Also the acidic alcohol mixture reacted with plexi-glass and broke the column. For this reason, alcohol is rejected as a possible solution to decrease fluorescein sorption.

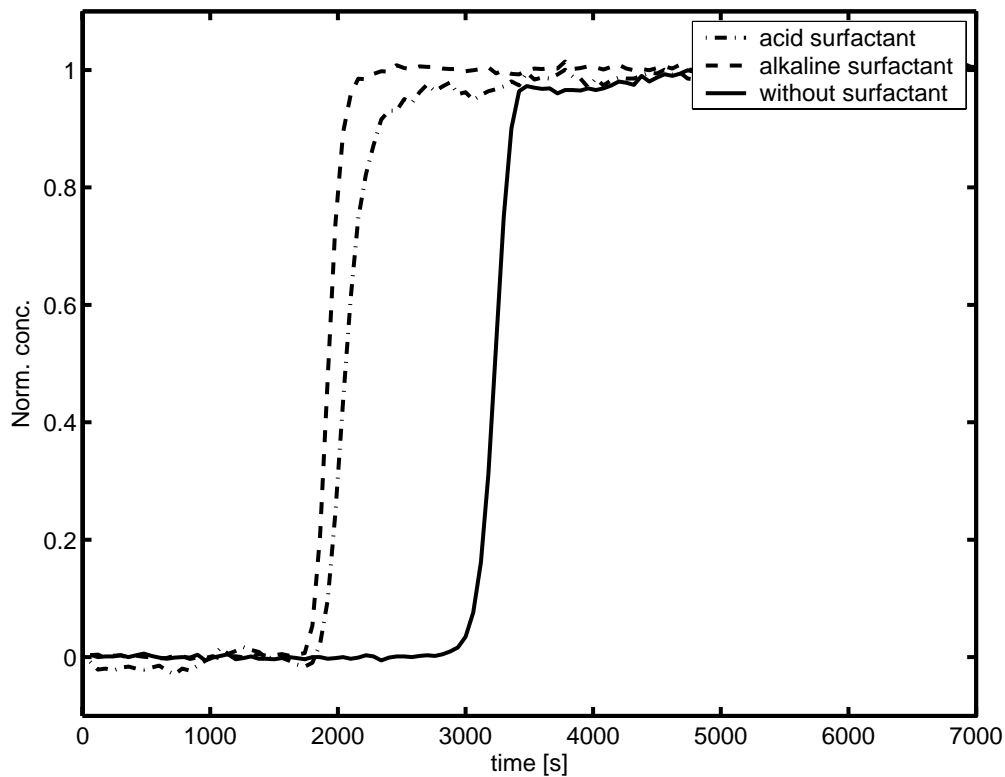


Fig 4.13 Comparison – BTCs in Lutensol GD70 and in deionised water

Similarly, fluorescence intensity BTCs are measured for a test conducted with surfactant solution of pH3. The surfactant used is Lutensol GD 70. Lutensit ALBN-50 was not included for column tests because of instable fluorescence intensity measurements noticed during the batch tests. The BTCs from the above mentioned tests have been compared. The results showed that the BTCs of acidic and basic surfactant solutions arrived earlier than that with the pure deionized water. Retardation of tracer to fine sand particles may be the reason for a delayed BTC in deionized water. Also the acidic and basic surfactant BTCs arrived at comparable times although they exhibited slightly different shapes towards the final stage. It is concluded from the results that tracer sorption has been considerably reduced by the introduction of surfactant solutions (Fig 4.13).

Since the results from small column tests supports introduction of non-ionic surfactant solution, I decided to use 2% of Lutensol GD 70 for the experiments.

4.2.4 Lutensol GD 70

The non-ionic surfactant Lutensol GD 70 is an alkyl poly glucoside. The exact number of alkyl and glucoside chains are not available as they are trade secrets of the manufacturer *BASF AG, Ludwigshafen, Germany*. The available significant details regarding the surfactant are given in Table 4.2.

Table 4.2 Properties of Lutensol GD 70

Type	Molecular weight	Critical micelle conc. (cmc)	Density at 23°C
<i>Alkyl poly glucoside</i>	<i>Approx. 600 g/mol</i>	<i>0.5 g/l</i>	<i>1170 kg/m³</i>

4.2.5 General experimental framework

4.2.5.1 Conservative tracer test

In a conservative test, the tracer (fluorescein) dissolved in an alkaline surfactant solution is passed through a porous medium saturated with an alkaline surfactant solution.

4.2.5.2 Reactive tracer test

In a reactive test, an alkaline surfactant solution is passed through a porous medium initially saturated with the tracer dissolved in an acidic surfactant solution. The tracer in acidic surfactant solution is non-fluorescent. But at the interface between the alkaline surfactant solution and the acidic surfactant solution the pH rises to about neutral and therefore the fluorescein fluoresce. The fluorescence of fluorescein at the interface is measured.

4.3 Experimental Setups

Two types of experimental setups are used to study the influence of longitudinal dispersive reactive mixing in porous media – a one-dimensional column that has been filled homogeneously with sand, and a quasi-two-dimensional sandbox that has been filled heterogeneously with four different types of sand.

4.3.1 One-dimensional column setup

The purpose of conducting column studies is:

- to check the adaptability and durability of the modified probes and the point measurement system,
- to verify the applicability of fluorescein as a conservative and a reactive tracer,

- to develop a system where dispersive mixing takes place,
- to calculate the longitudinal dispersivity and the diffusion coefficient using the temporal moments of concentration BTCs from conservative tests as mentioned in *Cirpka and Kitanidis, (2000a)*,
- to develop a methodology for predicting reactive mixing from conservative tracer data,
- to compare the experimental results with existing numerical and theoretical models of reactive mixing.

If the goal of developing a methodology that could predict dispersion-driven reactive mixing in a porous media from its conservative test data is achieved, then all other goals are met simultaneously.

4.3.1.1 Column description

The column used for the experiments is a 2m long gray-coloured PVC column with 10cm inner diameter (Fig 4.14). The gray-coloured PVC column prevents light from entering the column, and thereby suppresses photodegradation of the fluorescent tracer and the growth of algae. Above all, PVC has good resistance against the pHs (pHs between 3 and 10) used in the study.

Eight ports to insert optic fiber probes are constructed at each of the seven measurement cross sections of the column. The distance between the adjacent cross-sections is 0.25m. The eight ports present at each of the seven measurement locations are placed at equal distance with one another to measure the fluorescence intensity (Fig 4.14 and Fig 4.15). The column is designed with valuable guidelines from *Nielsen et al., (1991)* and *Ghodrati, (1999)*.

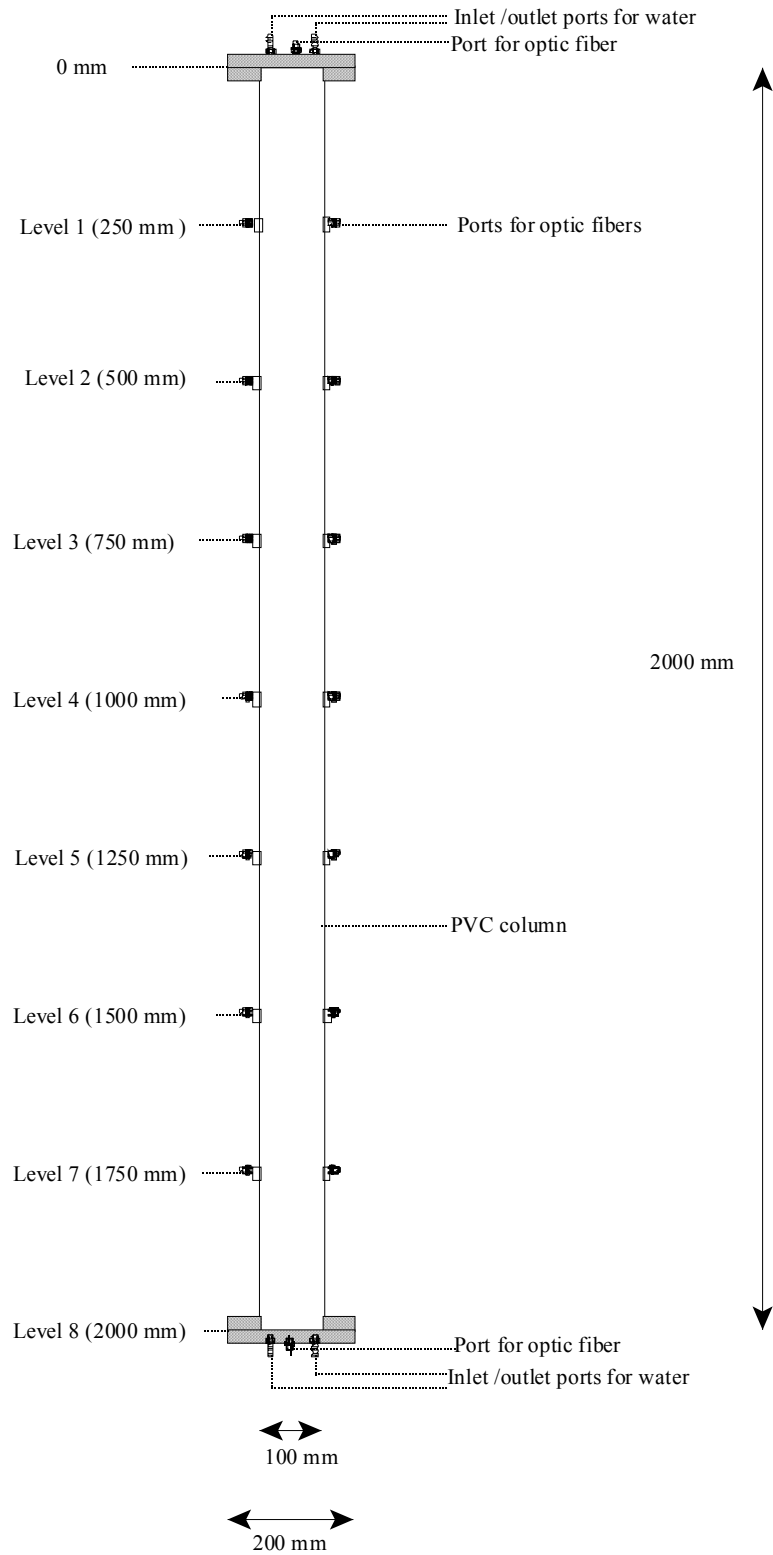


Fig 4.14 One-dimensional PVC column

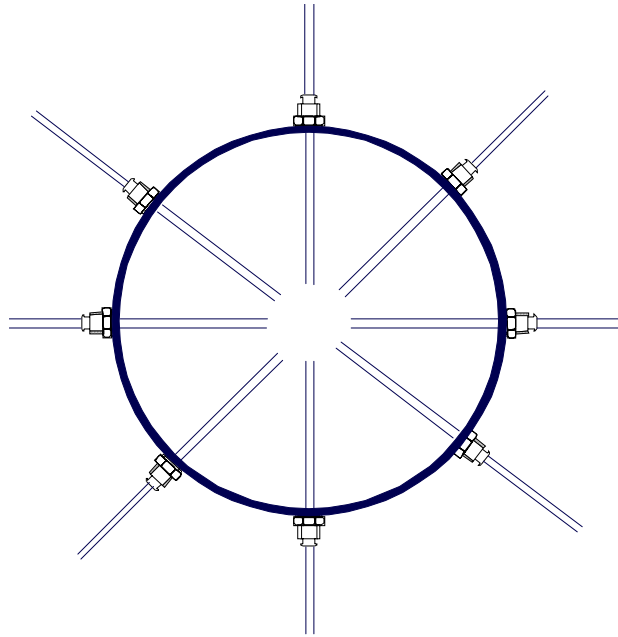


Fig 4.15 Arrangement of fiber optic probes at column cross-sections – Plan view

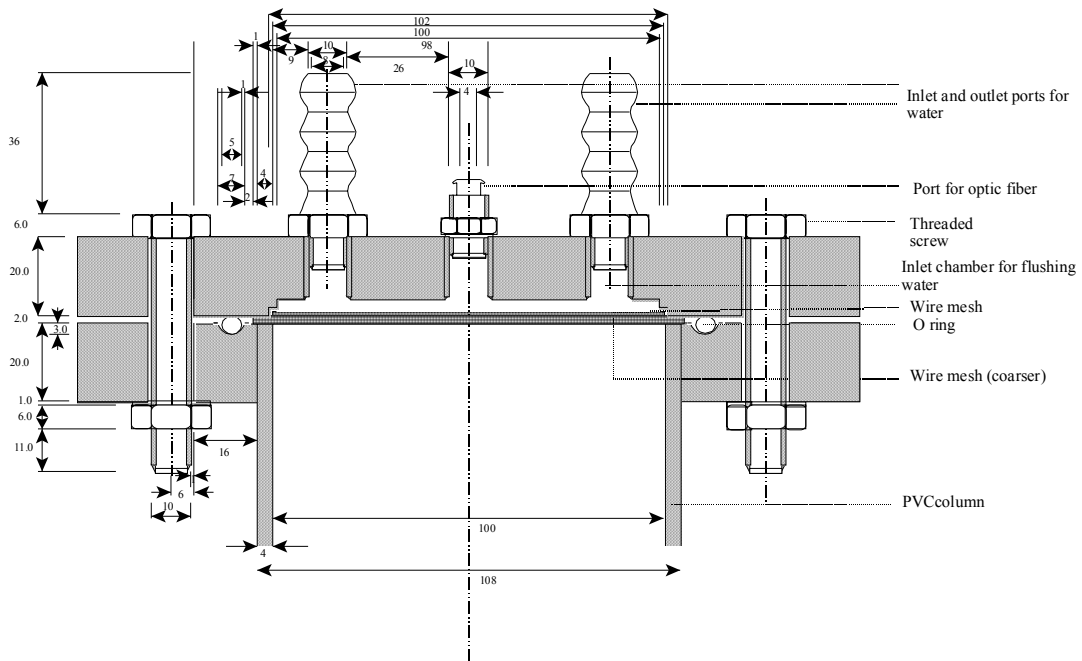


Fig 4.16 Design of the column ends

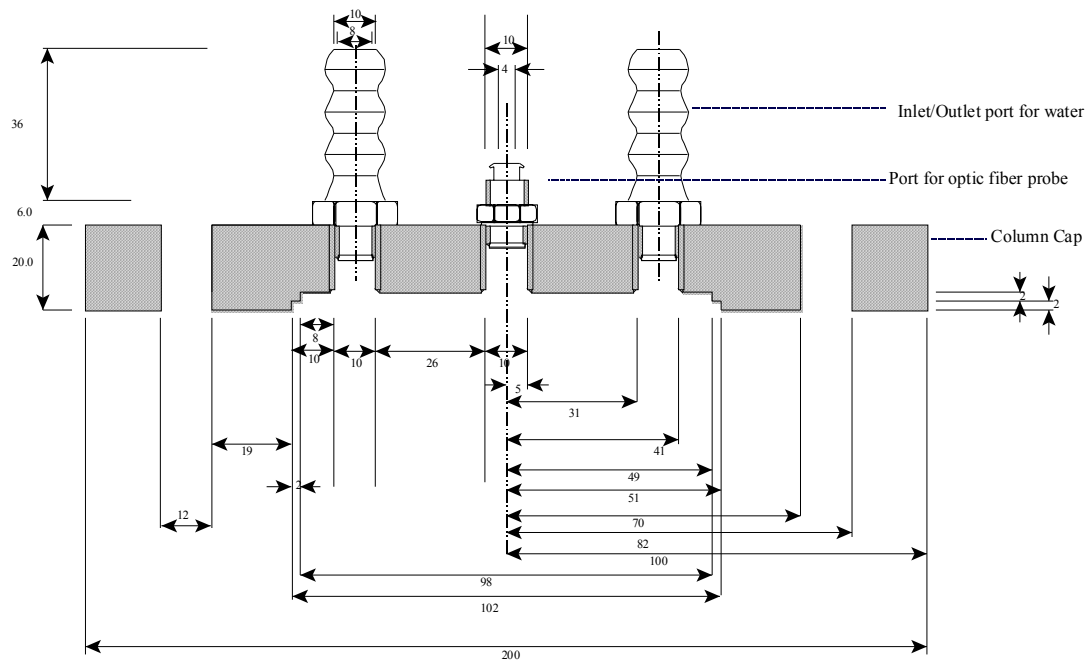


Fig 4.17 Design of the column caps

A chamber of 4mm depth and 10cm diameter is designed at the inner side of the inlet cover of the column (Fig 4.16). During the experiment, this chamber is flushed with the tracer solution before passing it through the column so that a mean concentration is achieved in the inlet for tracer tests with a step input of the tracer, and a cross-sectionally uniform injection of tracer is achieved. The outlet is also designed in a similar fashion. The advantage of having the chamber at both ends is that it allows the measurement of average concentration in the inflow and outflow. Therefore the covers at the inlet and outlet have a port each for introducing probes to measure fluorescence intensity (Fig 4.17). The covers also have two connectors each for passing water. One of those connectors at the inlet cover is used for solution input and the other one for solution output during the flushing of the inlet chamber. Out of the two connectors designed at the outlet cover, one is used for the introduction of CO₂ and the degassed water while the other is used as the outlet for water during the progress of an experiment.

4.3.1.2 Column packing

4.3.1.2.1 *Sand*

Pre-washed silica sand (*Dorosilit nr. 5, distributed by Dorfner-Firmengruppe, Germany*) with a grain size distribution between 1mm and 2.5mm (Fig 4.18) has been used for filling the column. The average grain size is 1.5mm and the hydraulic conductivity of the sand obtained from permeameter tests conducted in the laboratory is 1.67×10^{-2} m/s.

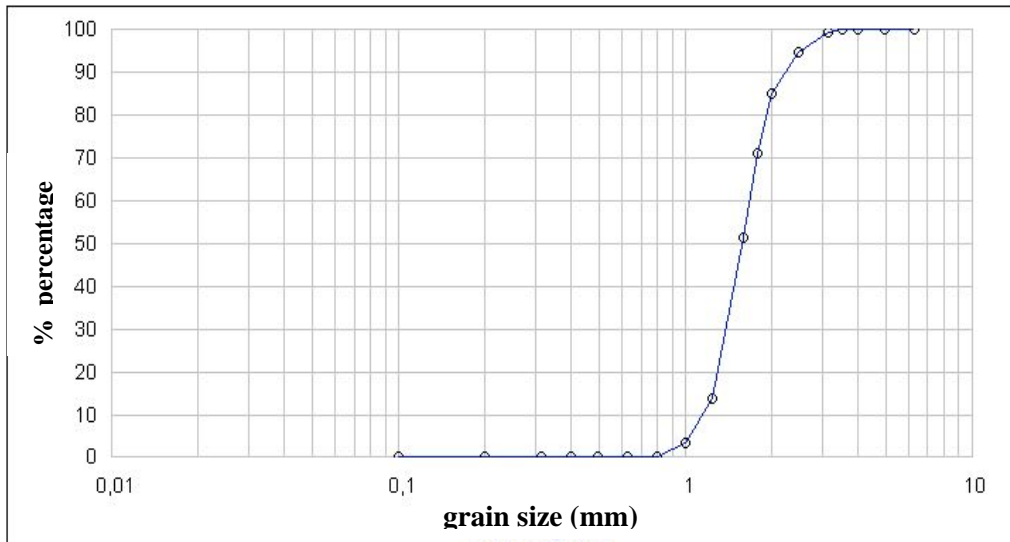


Fig 4.18 Grain-size distribution of the silica sand (Dorosilit Nr.5)

4.3.1.2.2 *Filling method*

From the several methods for uniformly filling and packing standard sandboxes and columns (eg. *Ripple et al., 1973; 1974; Oliviera et al., 1996*], the method of dry-filling has been selected for packing the column. In dry-filling of the column, sand is allowed to fall freely into the column through a funnel and a filling tube that has a diameter slightly smaller than the inner diameter of the column. A mesh is placed at the end of the filling tube, which is always maintained at a distance of 40 cm from the column bottom or the packed sand layer. During free fall, grains with larger size travel with velocities higher than the smaller ones. Large amount of sand falling freely will bounce back after hitting the mesh before it finally find its way through the mesh to settle in the column. During this bouncing back, the sand grains that fall with high velocities mix with that having low velocities and enable a homogeneous settling in the column. A continuous flow of sand grains is maintained in order to prevent formation of layers in the packed column.

4.3.1.2.3 *Filling set-up*

The accessories that were used in order to ensure a homogeneous packing of the column are:

- a 2m long steel filling-tube with steel meshes at one end,
- a funnel with a cone-shaped grain-distributor at its nozzle,
- a container of 50 liters volume,
- a crane.

The sand is directed into the column using a 2m long steel filling-tube. Steel is used as the material since it is relatively stable against deformation at room temperatures. The tube

has an outer diameter of approximately 8cm. Two steel meshes with mesh size of 5mm are placed at a distance of 5cm from each other at the bottom of the filling tube (Fig 4.19).

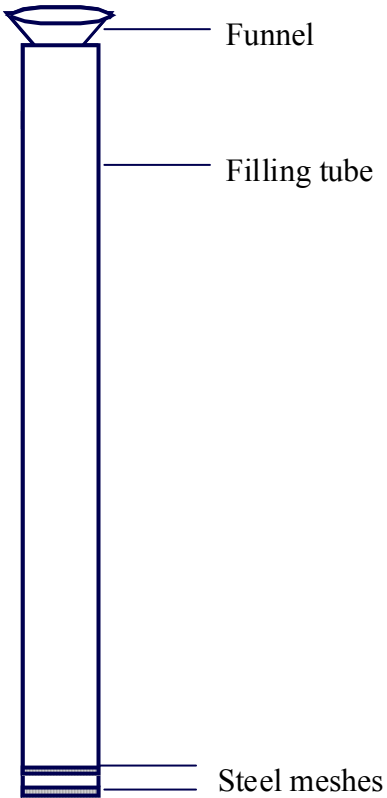


Fig 4.19 Design of the filling-tube

A funnel with a wide mouth and a nozzle with 3cm diameter is attached to the inlet of the filling tube to direct the falling sand from the container into the filling tube. A steel cone is inserted into the nozzle but not concealing it as shown in Fig 4.20. The steel cone is used to enhance the spreading of the sand, which otherwise would have settled more towards the centre of the column.

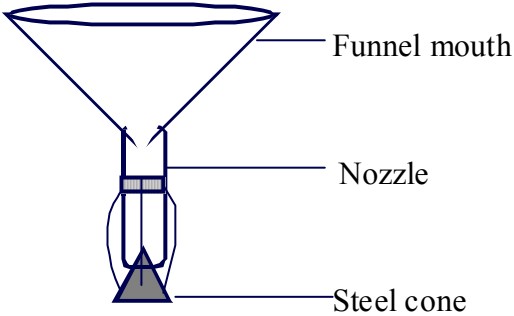


Fig 4.20 Funnel used for column packing

The approximate volume of the column is 16 litres. In order to ensure an uninterrupted flow of sand into the column, a 50 litre container was filled with sand to half its capacity. The container has an opening at its bottom, which is controlled by a valve. The container also has two hooks attached to its sides, which is used for hanging it to the crane to ensure the necessary height for the filling. Four circular hooks have also been made on the sides of the container at equal distances, to hang the filling tube (Fig 4.21).

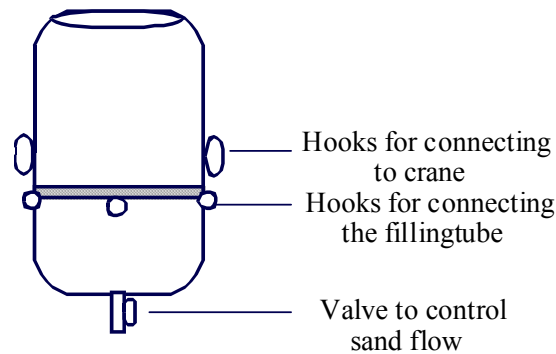


Fig 4.21 Container for holding the sand

I decided to continuously maintain a distance of 40cm between the filled sand layer in the column and the filling tube, throughout the filling procedure. For this the tube has to be moved gradually from an initial height of 2.4m to a final height of 4.4m during the filling. Therefore, the filling tube is connected to the container, which is then hung from a crane so that the height could be increased as required. The whole filling set-up is shown in Fig 4.22.

4.3.1.2.4 *Final filling of the column*

The PVC column is fixed onto a small table to prevent its toppling during filling (Fig 4.22). The filling set-up is then connected to the crane after filling the container with 50kg of sand. The filling tube is then inserted slowly into the column until the tip of the filling-tube is at a distance of 40 cm from the column bottom.

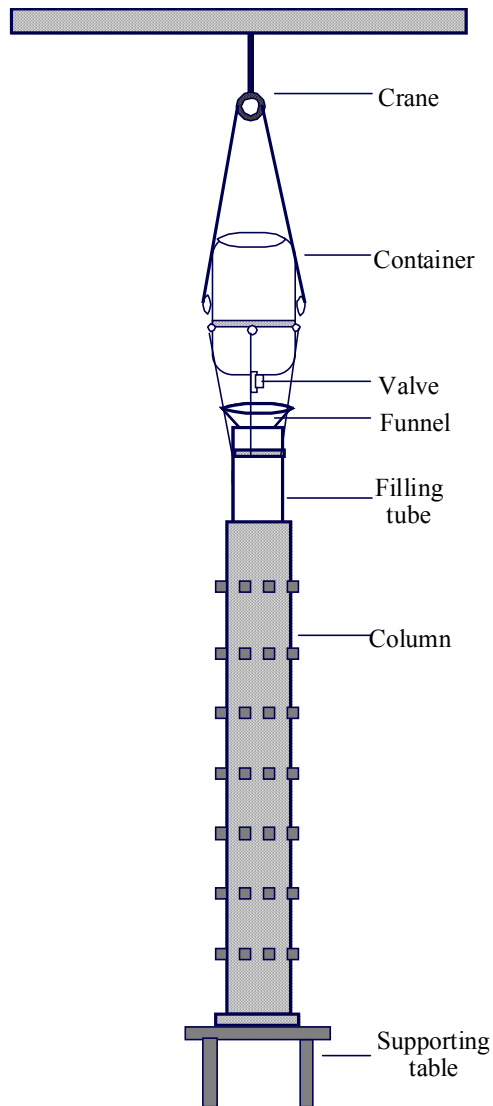


Fig 4.22 The complete set-up for column packing

The container valve is opened by two full turns and simultaneously the filling tube is raised with the lowest speed of the crane. During the filling, the column is manually hammered from its sides using a rubber hammer to increase the settling of the sand grains. Since enhanced settling of sand grains under fully saturated conditions is expected, more sand has been added at the inlet of the column to account for the settling and it is then confined by piling.

The packed sand column, which has been placed on a wide wooden base, is given additional support by connecting it to two metal holders attached to the laboratory wall. This is to prevent the PVC column from bending. A sketch of the experimental set-up is given in Fig 4.23.

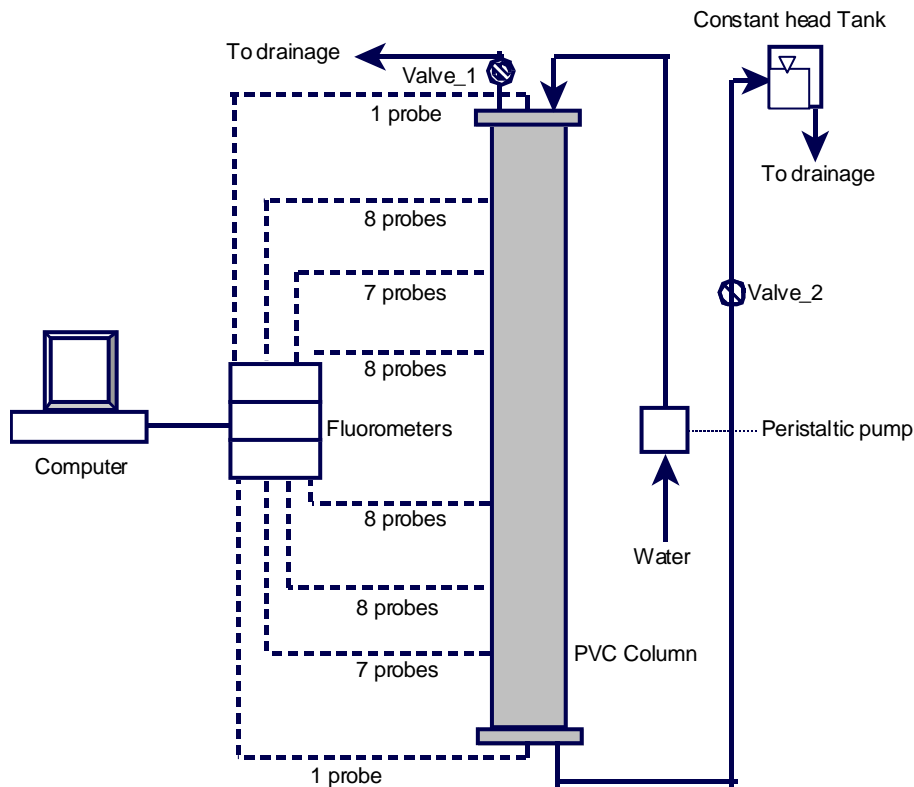


Fig 4.23 The one-dimensional experimental setup

4.3.1.3 Insertion of probes

The sand in the column is made moist by initially filling it with water and then draining. Holes of length 4cm and diameter 2.9mm are drilled into the moist sand through the ports planned to introduce optic fiber probes. The drilling has been done using a drilling machine with a needle of length 6cm and diameter 2.9mm. Drilling holes in the porous medium under moist conditions leaves them intact and therefore enables an easy placement of the probes in their prescribed positions without damaging them. The ratio of the column diameter and the proposed sand grain size together with the planned position of the probes effectively prevents the wall effects (*Schwartz and Smith, 1953; Lyczkowski, 1982; Dybbs and Edwards, 1985; Nielsen et al., 1991*). All the ports for fluorescence intensity measurements are then tightly sealed after placing the probes in their respective locations.

Following the placement of the probes in their respective locations, the water tightness of the probes and the column was checked by filling the column with water. Once the water tightness of the column is ensured, the column is drained of water and was left for 24 hours drying.

4.3.1.4 Removal of air from the column

The air in the system was removed by using the widely used method of carbon dioxide flushing. In this method, the air in the medium is displaced by passing carbon dioxide, from the bottom of the column. Since carbon dioxide has a higher solubility in water than air, it readily dissolved in the degassed water that was passed through the porous medium after it. Approx. 5 pore volumes of degassed water were used to guarantee fully saturated conditions.

4.3.2 **Sandbox setup**

[The original work on the design, construction, and filling of the sandbox is explained in Rahman's dissertation (Rahman, 2004). For more information on the sandbox, it is recommended to refer his dissertation].

The sandbox that has been used to conduct experiments relevant to my thesis is made of standard steel and has dimensions of 14mx0.5mx0.13m (Fig 4.24). The base and the rear sides are made of steel whereas the front side has a 15mm thick glass pane.

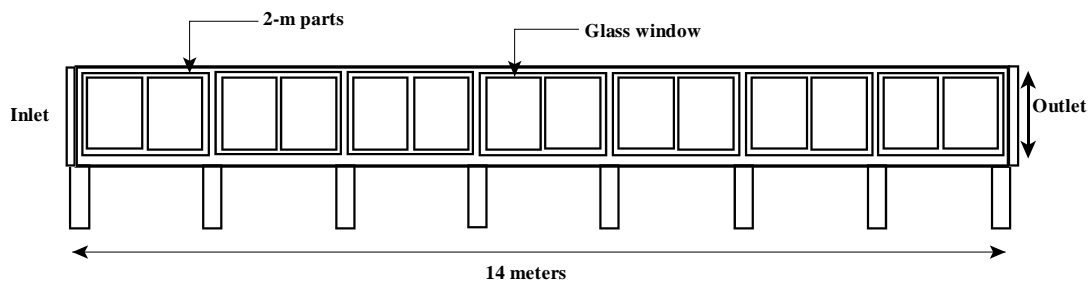


Fig 4.24 A general view of the sandbox (not to scale)

4.3.2.1 Design:

4.3.2.1.1 *Inlet*

The inlet of the sandbox has a 5cm long inlet chamber. A stainless-steel wire fabric (mesh size $< 0.1\text{mm}$) is used at the side facing the packed sandbox to keep the sand out of the inlet chamber. The wire fabric is fixed to a perforated stainless steel plate. Vertically, the inlet is divided into two parts by a stainless steel plate reaching into the sand filling as a flow separator. This provides opportunity to inject tracer solution separately into the upper or lower half of the domain.

A fiber-optic probe and a piezometer are connected to each injection chamber (Fig 4.25). Each chamber has three connections for water: one to inject water, one for the tracer solution, and a third to drain the chamber. This gives opportunity to flush the chamber with the tracer solution in order to achieve a uniform concentration in the inlet.

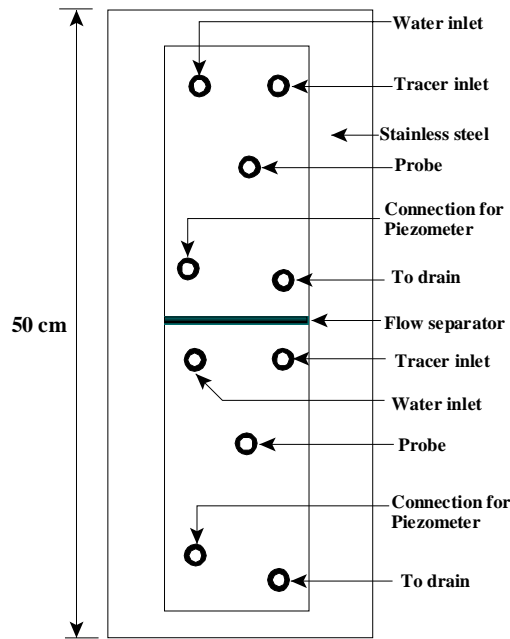


Fig 4.25 Inlet chamber of the sand box

4.3.2.1.2 *Domain*

A total of 126 fiber optic probes are inserted into the sandbox to measure tracer concentrations directly in the porous medium. They are connected in two sets, alternatively at equal distance, one with ten probes and the other with nineteen probes. The series repeat themselves at a distance of 2.8m. The connectors for the fiber optic probes are standard cable inlets with PG thread (inner diameter 9mm). The measurement tips of the fiber optic probes are kept 4cm inside the packed sandbox.

Hundred piezometer tubes are also connected to the domain to obtain pressure head measurements for the whole domain. A fine mesh is glued at the openings made for connecting the piezometric tubes to hold back the sand. Ten piezometers each are connected at every 1.4m length of the sandbox. The distance between the piezometers at each cross-section is 4.8cm. The position of the probes and the piezometers are shown in Fig 4.26.

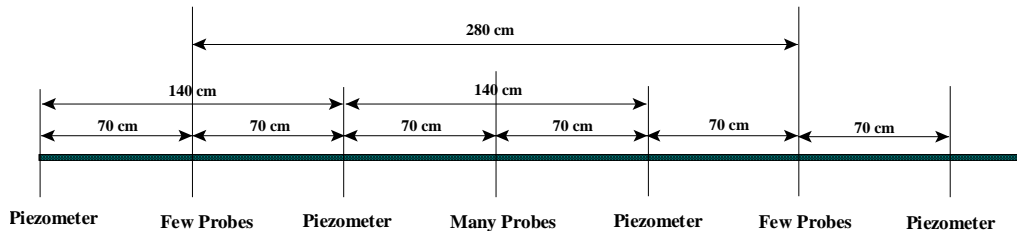


Fig 4.26 Position of the piezometers and the probes at the domain of the sandbox

4.3.2.1.3 Outlet

Like the inlet, the outlet of the box also has a chamber that is 5cm long, and it is vertically separated into 19 flow chambers that allows to measure a spatially highly resolved concentration profile at the outlet of the box. Perforated steel sheets and wire fabrics are used in the same fashion as in the inlet to keep the sand out of the outlet chambers. Each of the nineteen chambers has connections to an outlet tube and a piezometer (Fig 4.27). Fiber optic probes are connected to the outlet tubes by flow through cells (Fig 4.28), whereas piezometers are directly connected to the outlet flow chambers.

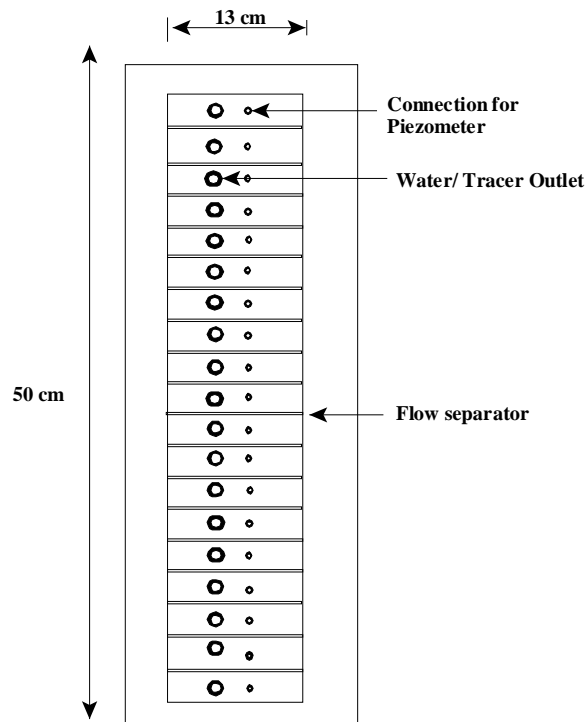


Fig 4.27 Outlet flow chamber of the model sandbox

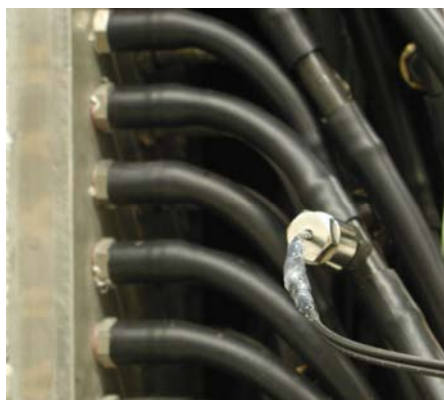


Fig 4.28 A flow through cell

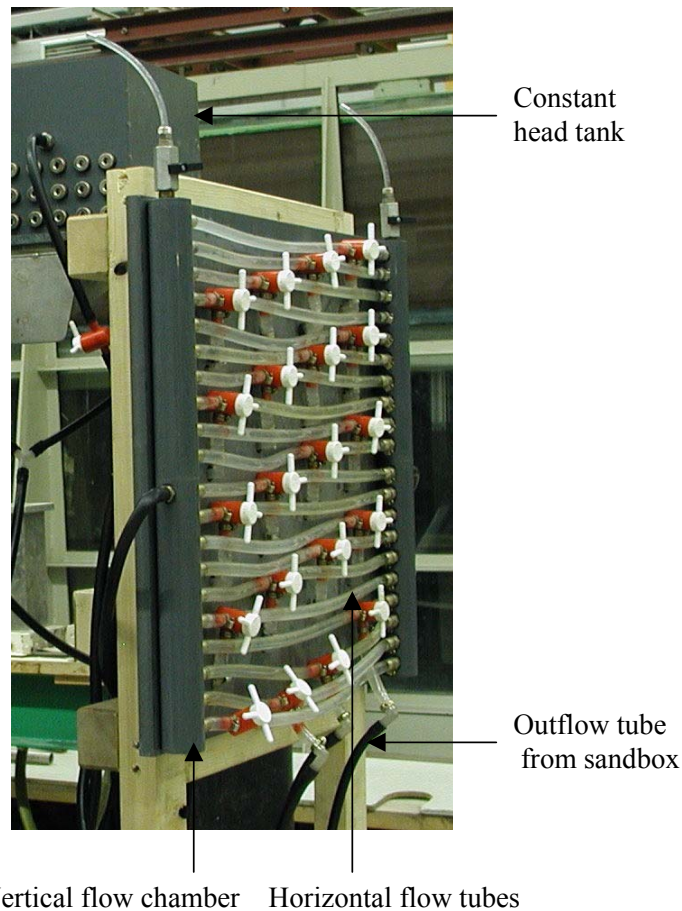


Fig 4.29 Hydraulic switchboard

The outflow tubes are connected to a hydraulic switch board (Fig 4.29). The principle of the board is to measure the discharge of the nineteen flow chambers separately. The switch board consists of two vertical flow chambers, each with connections to the outlet constant-head tank, and to the nineteen horizontal tubes. Each of the nineteen horizontal flow tubes is connected to the two vertical flow chambers of the switch board, and to one of the nineteen outflow chamber of the sandbox via a three-way-valve. By connecting a single outflow chamber to one constant-head tank while connecting all other outflow chambers to the other constant-head tank, the discharge of this single chamber can be measured.

4.3.2.2 Sandbox filling:

The sandbox is heterogeneously filled with four different types of silica sand. The grain size distribution, and hydraulic conductivity (measured in the lab by permeameter tests) of the sand are given in Table 4.3.

Table 4.3 Grain sizes and hydraulic conductivity of the sand types used in the sandbox

Name	Type	Grain size (mm)	Conductivity (m/s)
Coarse sand	Dorsilit Nr. 5	1.00-2.5	1.67×10^{-2}
Mixed sand	Dorsilit Nr. 7 and 8	0.3-0.6 and 0.6- 1.2	4.32×10^{-3}
Medium sand	Dorsilit Nr. 0-3	0.0 – 3.0	9.09×10^{-4}
Fine sand	Dorsilit Nr. 8/9	0.1-0.8	5.61×10^{-4}

The heterogeneity produced in the sandbox are quite similar to the heterogeneity pattern observed in nature (Fig 4.30). More insight into the filling procedure is given in *Rahman (2004)*. To prevent preferential flow, and also to ensure confinement of the packing, a 3 cm thick layer of bentonite (Fig 4.31) was added at the top of the sand filling. Swelling of the bentonite was supposed to adjust for the enhanced settling of the sand under fully saturated conditions. Finally an elastomer sheet is placed on the top of the bentonite layer and the sandbox is totally concealed using a combination of PVC sheets and metal frames.

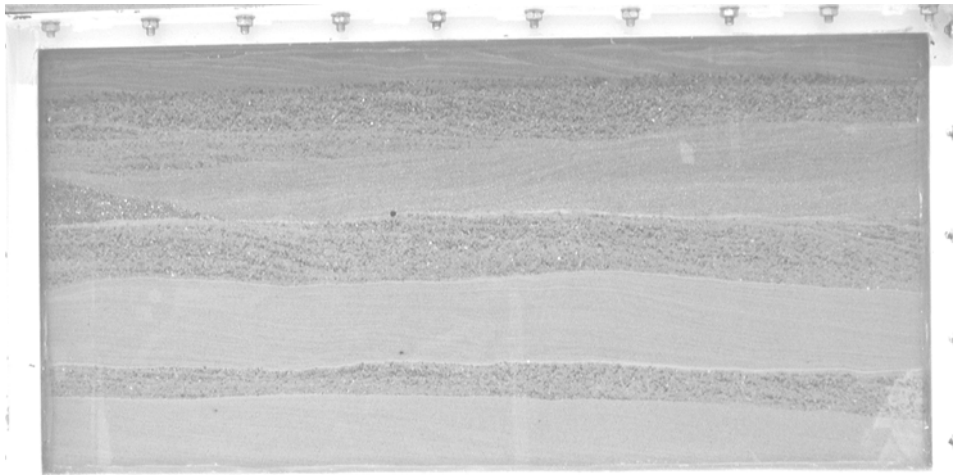


Fig 4.30 Heterogeneous filling in the sandbox

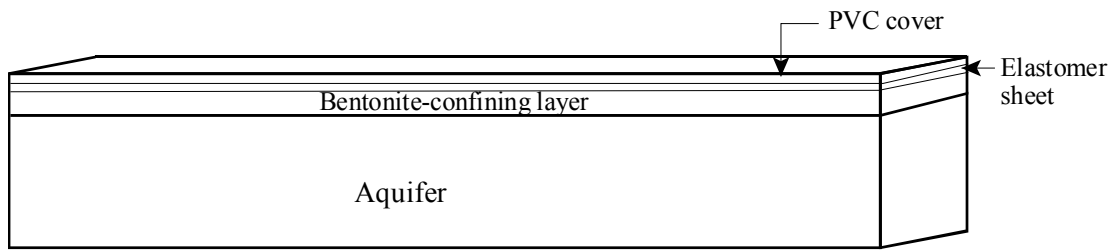


Fig 4.31 Confining layer and cover of the box

The sandbox has been completely covered using black clothes during the experiments to prevent the photodegradation of fluorescein.

5 EXPERIMENT TYPES AND PROCESSING OF MEASURED DATA

In this chapter, details about different types of experiments conducted in the framework of the thesis and their scales are given. Also a short description on the estimation of various quantities of interest from the measured data is provided. The experiments conducted within the framework of this thesis may be classified as batch tests, conservative tests, and reactive tests. The conservative and reactive tests are carried out both in laboratory-scale (column setup) and technical-scale (sandbox setup) systems.

5.1 Batch Tests

Batch tests are conducted to understand and quantify the following relationships between quantities that are relevant in terms of the conservative tests and the reactive tests:

- Fluorescence intensity as a function of tracer concentration,
- Resultant fluorescence intensity as a function of pH,
- pH of the medium as a function of mixing ratio, which is the volume of the injected solution to the total solution volume.

5.1.1 Fluorescence intensity and tracer concentration

Tracer solutions are prepared in deionized water with fluorescein concentration varying between 10 μ g/l and 90 μ g/l. About 10ml is taken from each tracer solution and its fluorescence intensity is separately measured using a spectrofluorometer.

I also prepared tracer solutions in the same tracer concentration range as mentioned earlier, but in deionized water containing the nonionic surfactant, Lutensol GD70. The concentration of the surfactant in the solution is 2% of the total solution volume. The fluorescence intensity of each tracer solution is measured using a spectrofluorometer. The results of both tests are given in Fig 5.1. A linear relationship between the two quantities as mentioned in *Guilbault (1990)* is observed from the results.

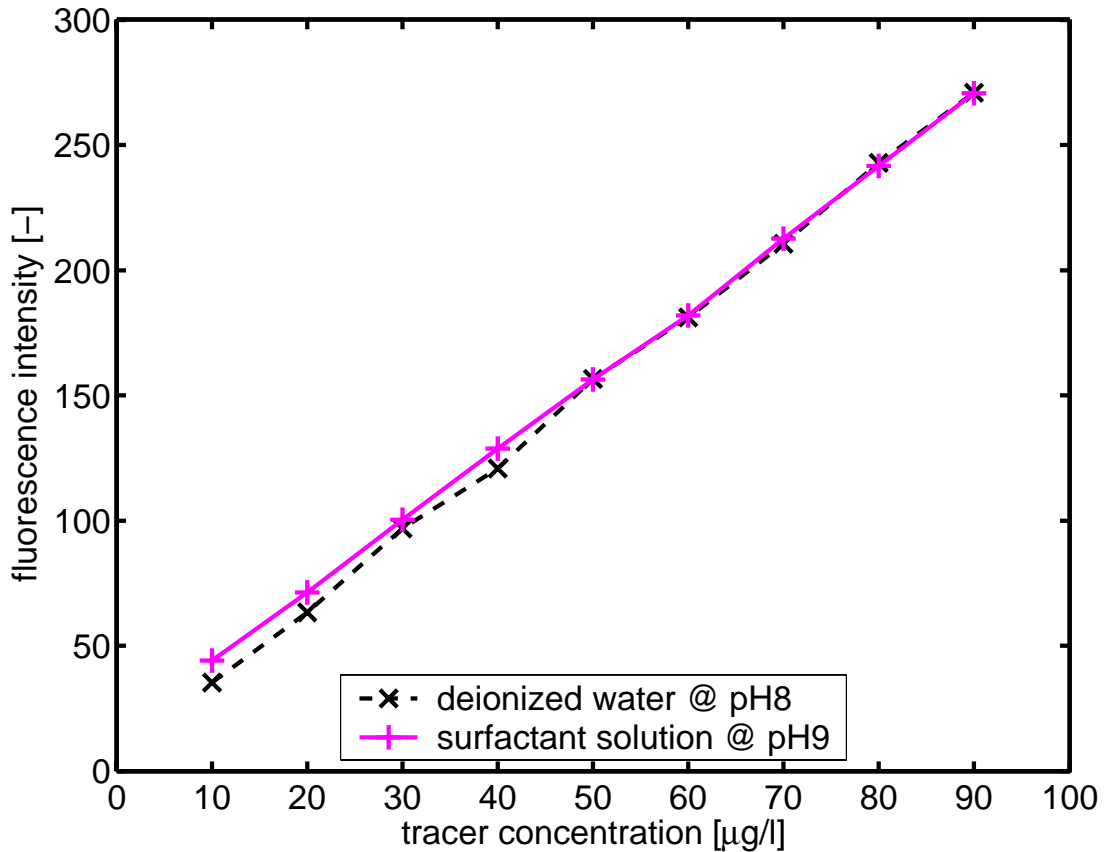


Fig 5.1 Fluorescence intensity of fluorescein as function of tracer concentration

5.1.2 Fluorescence intensity and solution pH

The relationship between fluorescence intensity of fluorescein and solution pH is established by a batch test. Two types of solutions – an alkaline and an acidic solution, both with tracer – are used for the test.

An alkaline surfactant solution is prepared by adding concentrated NaOH (sodium hydroxide) into a surfactant solution. The surfactant solution is prepared in deionized water and the concentration of surfactant is 2% of the solution volume. The pH of the alkaline solution is 11. Meanwhile, an acidic surfactant solution with pH3 is prepared by adding concentrated HNO₃ into a surfactant solution prepared in the same way as mentioned before. The fluorescein concentration of both solutions are set to 100µg/l by adding fluorescein. Both solutions are stirred to ensure complete mixing.

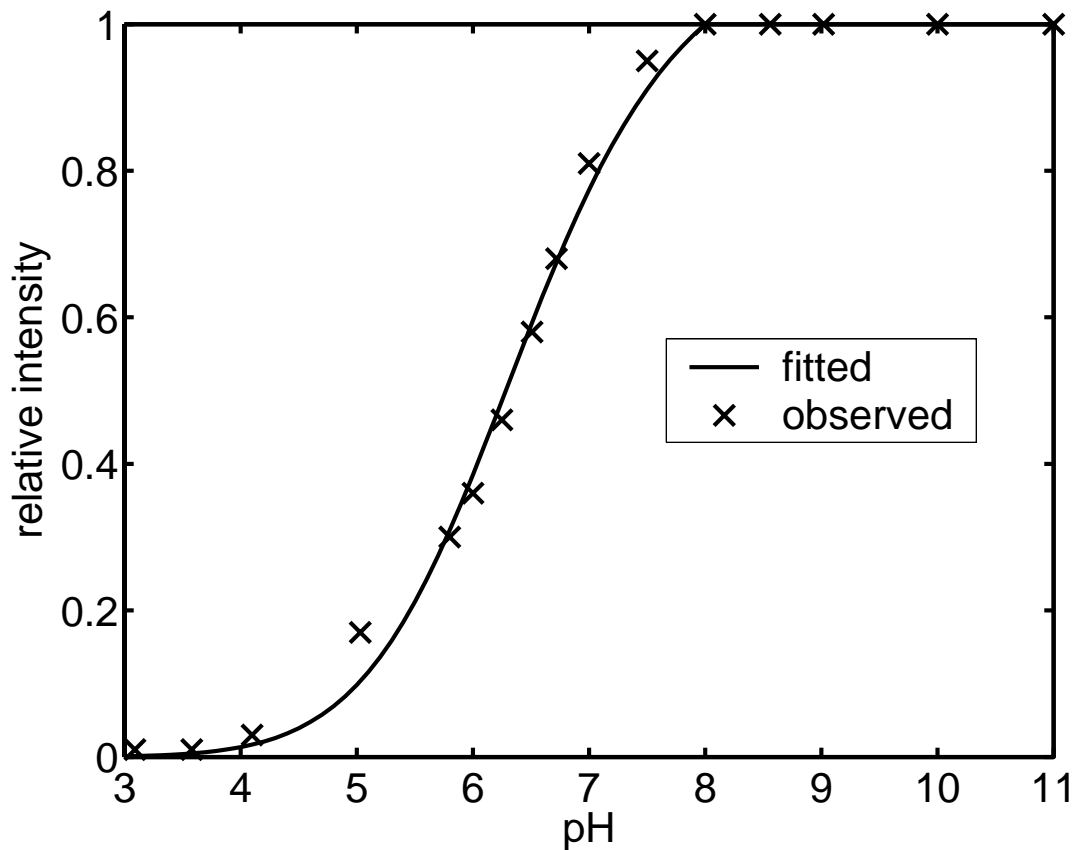


Fig 5.2 Relative fluorescence intensity as function of solution pH

50ml of the acidic surfactant solution is transferred into a brown bottle covered with a black cloth. The bottle is equipped with a pH electrode and a fiber optic probe, both fixed in their positions. The solution in the bottle is gently stirred using a magnetic stirrer. The alkaline solution is added in small amounts at regular intervals to the solution in the brown bottle and the resulting pH and fluorescence intensity are measured. Later, the fluorescence intensity and pH during the mixing of an alkaline and an acidic surfactant solution without tracer is measured to get the base values of fluorescence intensity in the measured pH range. The base values are then subtracted from the fluorescence intensities measured for the mixing tests with tracer to get its actual fluorescence intensity. The actual fluorescence intensities are normalized based on the minimum fluorescence intensity (at pH3) and the maximum fluorescence intensity (for pH above 8). The relative fluorescence intensities for pH values between 3 and 11 are plotted in Fig 5.2. It can be seen from the figure that the relative fluorescence intensity of fluorescein is negligible at acidic pHs (\leq pH4) and then increases to stabilize at alkaline pHs (pH \geq 8). The following empirical relationship is fitted to the measured data minimizing the root mean square error (RMSE):

$$I_{rel}(pH) = \max\left(pH^{9.269} \times \frac{1.135}{pH^{9.269} + 3.179 \times 10^7}, 1\right) \quad (5.1)$$

where $I_{rel}(pH)$ is the relative fluorescence intensity. The fitted curve is also shown in Fig 5.2.

5.1.3 Solution pH and mixing ratio

Titration tests using the alkaline and acidic surfactant solutions assist in establishing the relationship between the pH of the medium and the alkaline mixing ratio X_{base} , which is defined as the ratio of the added solution volume to the total solution volume.

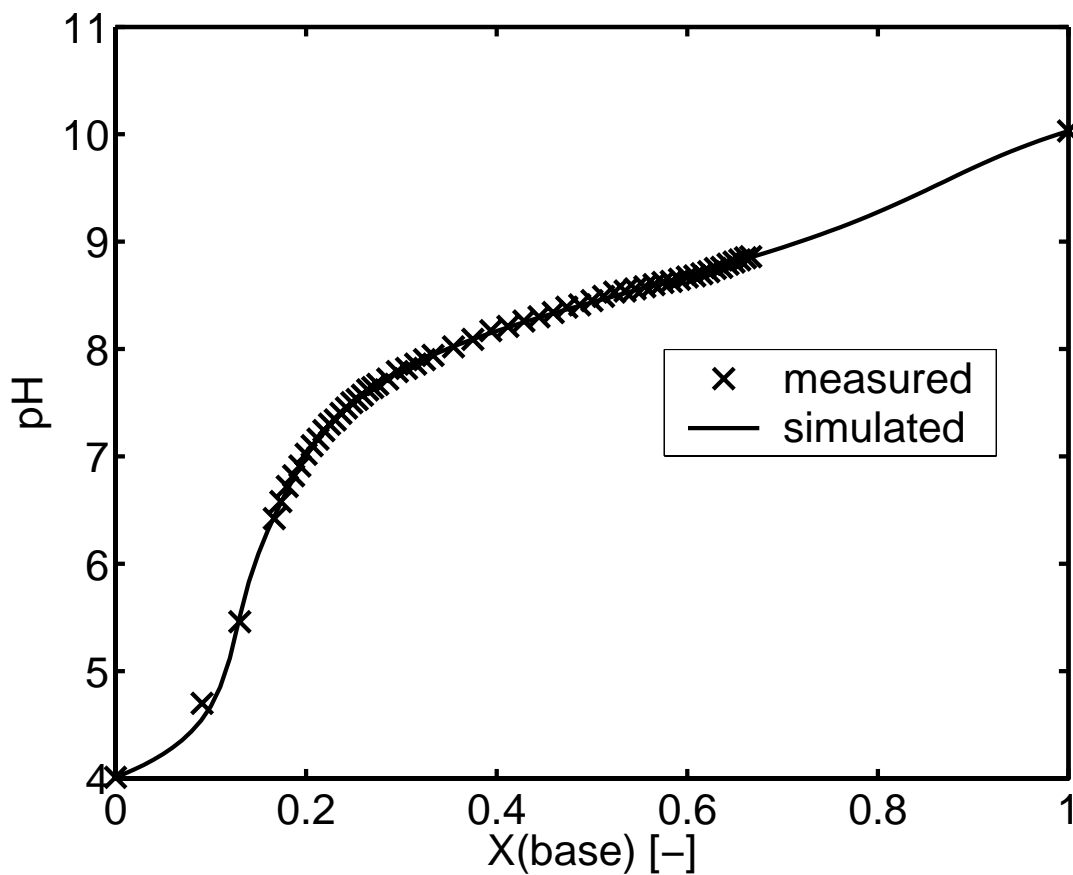


Fig 5.3 Titration curve between pH4 surfactant solution and pH10 surfactant solution

A titration test between pH4 and pH10, and two titration tests between pH3 and pH10 are carried out. The preparation of the alkaline and acidic surfactant solutions is the same as that mentioned in 5.1.2, except that the tracer is added only to the acidic surfactant solution. About 100ml of the acidic solution is transferred to the bottle used for estimating the fluorescence intensity as a function of the solution pH (5.1.2). The solution is stirred continuously. The alkaline surfactant solution is added in increments at definite intervals to

the acidic tracer solution and the resultant pH is measured. Fig 5.3 shows the results from a titration test between pH4 and pH10, and Fig 5.4 includes results from titration tests between pH3 and pH10. Titration between two pH combinations are conducted since the reactive test in the column is executed between pH4 and pH10, but that in sandbox is conducted between pH3 and pH10. All titration curves indicate buffering of the surfactant solution at slightly alkaline pH values. Although the titration curves between pH3 and pH10 differ quantitatively, they agree qualitatively among themselves (Fig 5.4). This may be due to the instability of one of the surfactant solutions used for the titration.

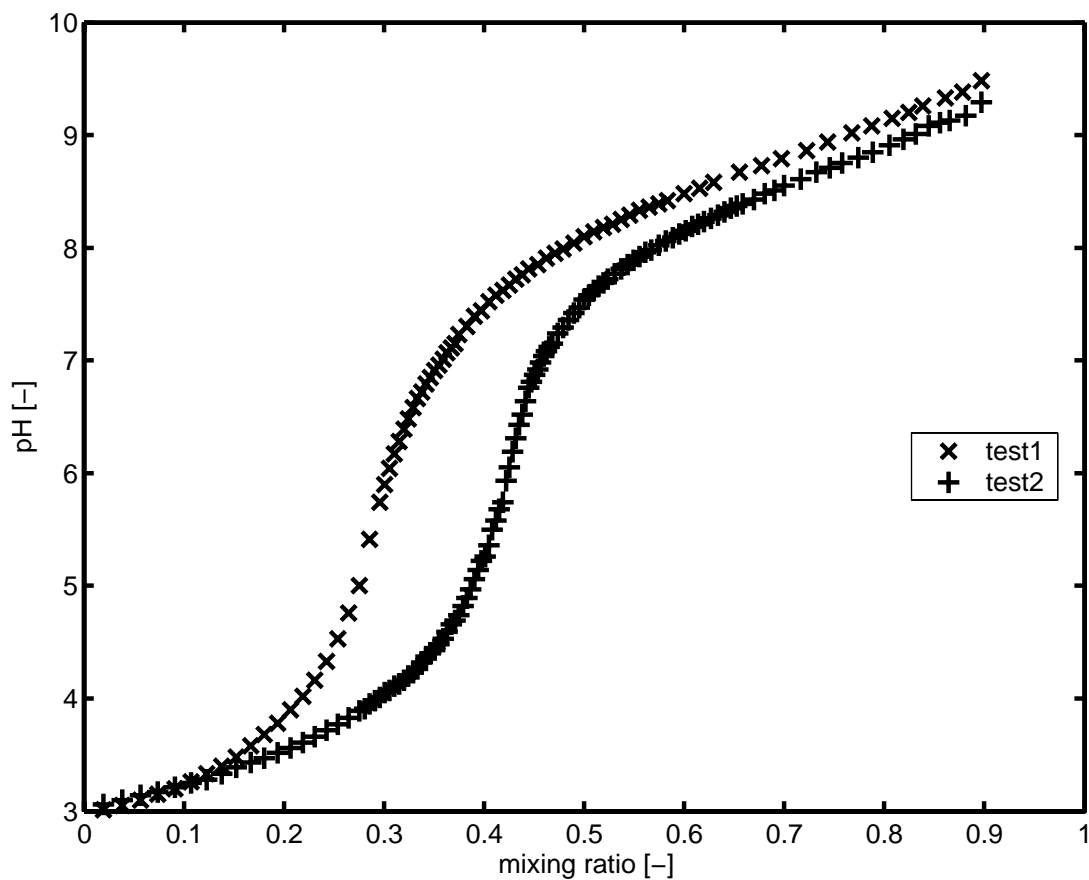


Fig 5.4 Titration curves between pH3 surfactant solution and pH10 surfactant solution.

A standard buffer equation with two buffering compounds is fitted to the titration curve between pH4 and pH10, using the Levenberg-Marquardt algorithm. For estimated equilibrium constants K_{a1} and K_{a2} of the buffer reactions and estimated total buffer concentrations $[Buf_{1,tot}]$ and $[Buf_{2,tot}]$, the proton concentration is calculated from the cumulative charge of all counter-ions, that is, all ions except for the buffer, hydronium and hydroxonium ions, by iterative solution of:

$$[H^+] = \frac{1}{2} \left(\sqrt{\text{charge}^2 + 4 \left(10^{-14} + \frac{K_{a1} [H^+] [Buf_{1,tot}]}{[H^+] + K_{a1}} + \frac{K_{a2} [H^+] [Buf_{2,tot}]}{[H^+] + K_{a2}} \right)} - \text{charge} \right) \quad (5.2)$$

in which the charge of the counter-ions for a certain mixing ratio is given by linear interpolation of the charges in the acidic and alkaline endpoint solutions.

The fitted concentration of the first buffer is $5.32 \times 10^{-4} \text{ mol/l} \pm 6 \times 10^{-6} \text{ mol/l}$ with a fitted pKa of 8.541 ± 0.006 . The fitted concentration of the second buffer is $5.27 \times 10^{-5} \text{ mol/l} \pm 1.5 \times 10^{-6} \text{ mol/l}$ with a pKa of 6.416 ± 0.047 . The simulated titration curve is included in Fig 5.3. Although the second pKa agrees with pKa-values of fluorescein reported in the literature, I do not believe that fluorescein is the major buffering compound in this pH range because the fitted buffer concentration is about two orders of magnitude higher than the fluorescein concentration added to the acidic solution. Since the exact chemical structure of the surfactant mixture is not published by the supplier, the fitted pKa values and buffer concentrations cannot be related to specific functional groups of the surfactant molecules.

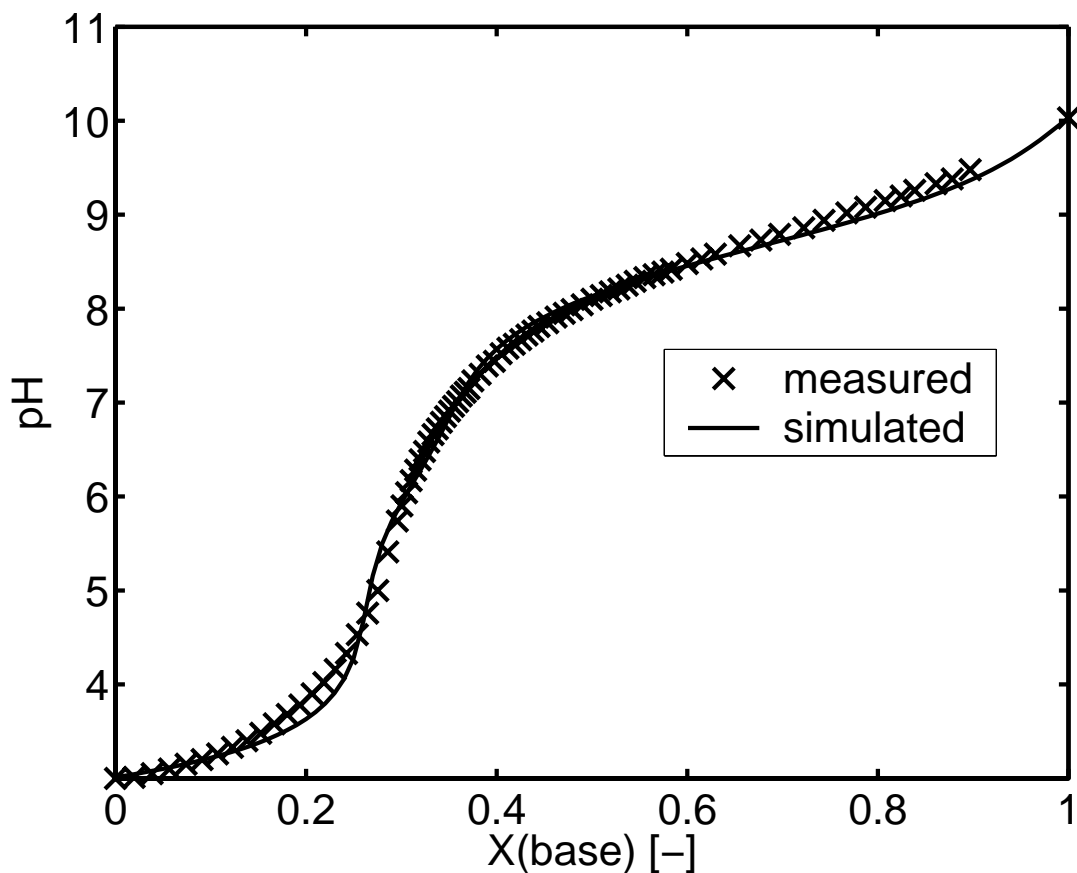


Fig 5.5 Measured and simulated titration curves between pH3 surfactant solution and pH10 surfactant solution.

The measured titration curve for test between pH 3 and pH 10 (test 1) was fitted using a buffer model developed based on the same concept (Fig 5.5). The fitted concentration of the first buffer in this case is $2.39 \times 10^{-3} \text{ mol/l} \pm 2.36 \times 10^{-5} \text{ mol/l}$ with a fitted pKa of 8.668 ± 0.024 . The fitted concentration of the second buffer is $3.46 \times 10^{-4} \text{ mol/l} \pm 1.39 \times 10^{-5} \text{ mol/l}$ with a pKa of 6.123 ± 0.067 .

5.2 Conservative Tracer Tests

In a conservative tracer test, an alkaline solution containing tracer is injected into a porous medium initially saturated with another alkaline solution without tracer but with the same pH. The general framework of the conservative tracer test is given in Fig 5.6. A conservative tracer test is done in the column and two conservative tests are carried out in the sandbox.

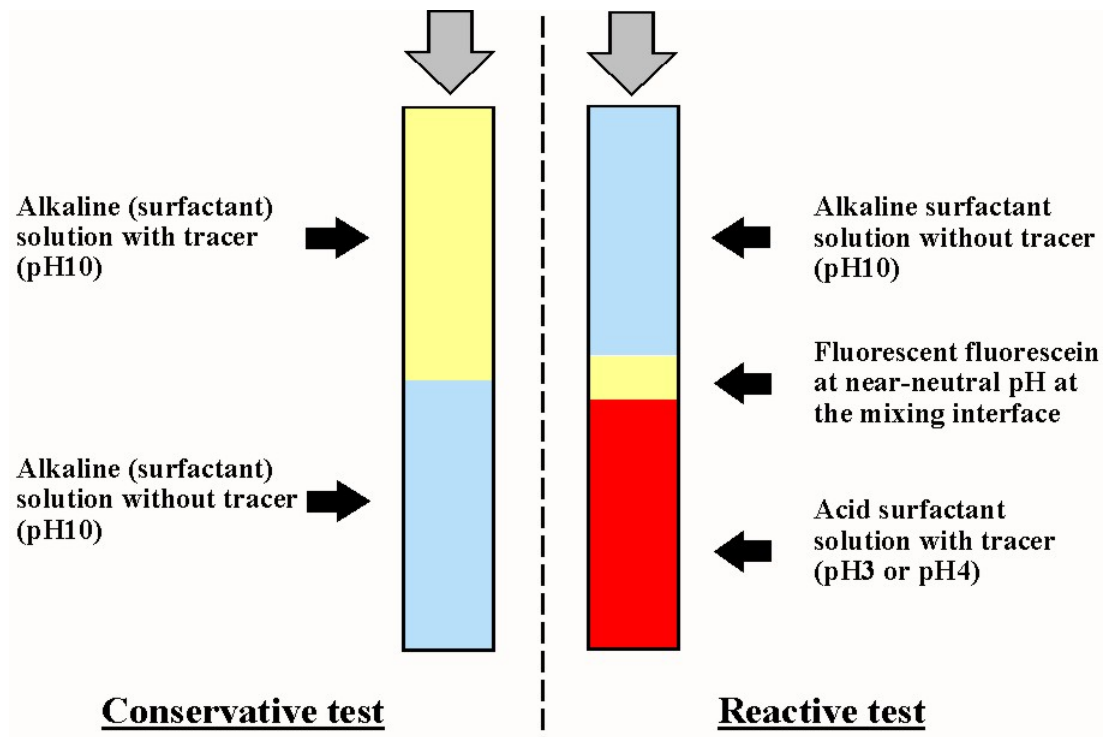


Fig 5.6 General framework of the conservative and reactive tests.

5.2.1 Homogeneously packed porous medium (column)

Twenty liters of the conservative test solution (alkaline surfactant tracer solution with pH10) is prepared following the steps mentioned in Table 5.1. The solution is stirred continuously by a magnetic stirrer. In order to prevent bacterial growth, which may occur due to the presence of surfactants, sodium azide (NaN_3) is added to the surfactant solution. The sodium azide concentration in the solution is 0.1 mmol/l (1 mole of sodium azide equals 65.01 g). The fluorescein concentration in the tracer solution is $100 \mu\text{g/l}$. The solution is stirred

approximately for 12h after adding all the required components. Similarly, an alkaline surfactant solution without tracer is also prepared.

Initially, the homogeneously packed porous medium in the column is completely saturated with the alkaline surfactant solution without tracer. This is to provide an environment with similar chemical properties for the tracer solution that is to be injected into the porous medium. Before introducing the alkaline surfactant solution with tracer into the porous medium, the inlet chambers are thoroughly flushed with it. This is to achieve a uniform tracer concentration in the inlet so that the tracer could be introduced into the porous domain as a uniform continuous input along the entire inlet domain. Flushing of the inlet is done by closing the outlet valve (valve2) of the column and simultaneously opening the valve to the drainage (valve1) at the inlet (Fig 5.7).

Table 5.1 Steps involved in the preparation of conservative test solution

Step numbers	Conservative Test Solution	
	Column	Sandbox
Step 1	Collect 20liters deionized water	Collect 2000liters deionized/degassed water
Step 2	Add 400ml of surfactant	Add 40liters of surfactant
Step 3	Add approx. 140mg of sodium azide (NaN_3)	Add approx. 14g of sodium azide (NaN_3)
Step 4	Add tracer to bring the tracer concentration to $100\mu\text{g/l}$	Add tracer to bring the tracer concentration to $100\mu\text{g/l}$
Step 5	Add conc. NaOH to get the resultant pH as 10	Add conc. NaOH to get the resultant pH as 10

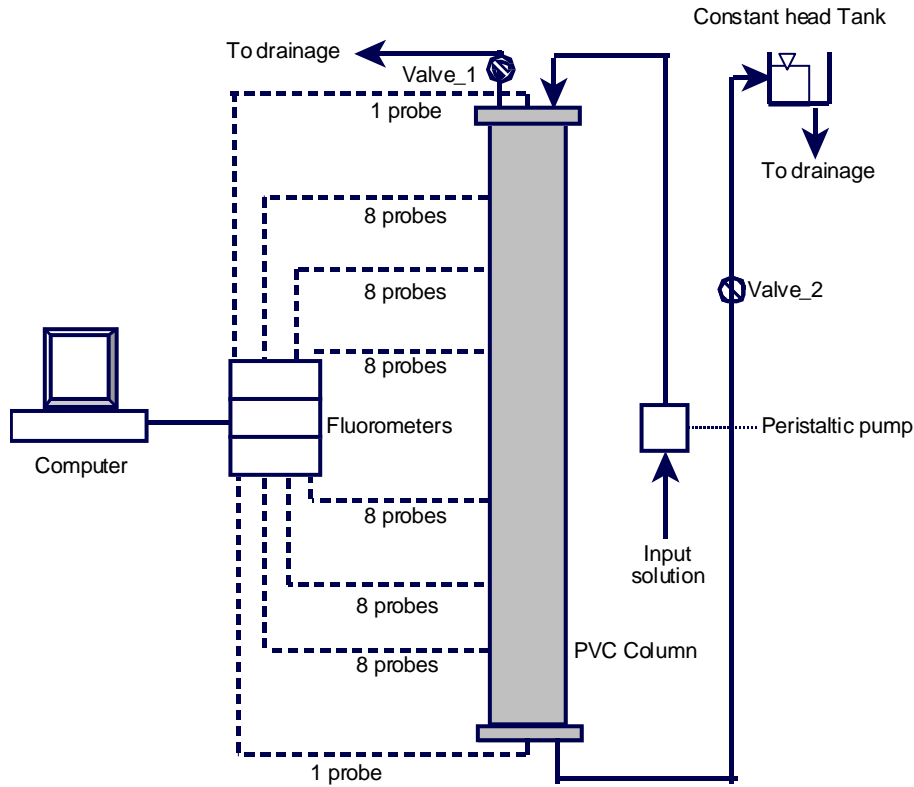


Fig 5.7 Column experiment setup

Once the inlet chamber is fully saturated with the alkaline tracer solution, it is injected into the column by closing valve1 and opening valve2 simultaneously. The experiment is carried out under constant flux conditions and the measured average specific discharge is $7.16 \times 10^{-5} \text{m/s}$ (coefficient of variation is 2%). A Masterflex peristaltic pump is used in the test. The mean porosity of the column packing is calculated to be 0.41 with a coefficient of variation of 5%. Approximately 3 pore volumes (18 liters) of tracer solution is passed through the column before the experiment is terminated. During the course of the experiment, fluorescence intensity measurements are taken every two seconds and the values are averaged over a minute. At each of the seven measurement sections for fluorescence intensity, eight probes are available except at sections 3 and 7 where a probe each was substituted by a luer-lock syringe to provide local pH measurements during the reactive tracer test that preceded the conservative test.

Breakthrough curves of fluorescence intensity as a function of time, which is obtained at each of the measurement location, is normalized based on its maximum and minimum values:

$$I_{norm} = \frac{I_{meas} - I_{min}}{I_{max} - I_{min}} \quad (5.3)$$

where I_{norm} is the normalised fluorescence intensity, while I_{meas} is the measured intensity, and I_{max} and I_{min} are the maximum and minimum fluorescence intensities, respectively. Since the fluorescence intensity is linearly proportional to the tracer concentration at constant pH, the normalized fluorescence intensity is identical to the normalized tracer concentration.

The normalized breakthrough curves are analysed by the method of temporal moments. The k th noncentral temporal moment of (m_k) of a tracer introduced as Dirac pulse is defined by

$$m_k = \int_0^{\infty} t^k c_{\delta}(t) dt \quad (5.4)$$

in which $c_{\delta}(t)$ is the normalised concentration resulting from a pulse injection. The corresponding second central moment is:

$$m_{2c} = \int_0^{\infty} (t - m_1)^2 c_{\delta}(t) dt = m_2 - m_1^2 \quad (5.5)$$

In the experiments, however, the conservative tracer is introduced continuously rather than by a pulse. The corresponding normalized concentrations, denoted by $c_H(t)$, is analysed based on their truncated temporal moments. The k th truncated moment is defined by:

$$T_k(c_H, t_e) = \int_0^{t_e} t^k c_H(t) dt \quad (5.6)$$

in which t_e is the truncation time that needs to be chosen such that the maximum concentration has already been reached. For the normalized concentrations, pulse-related temporal moments are calculated from the truncated moments of the breakthrough curves originating from continuous injection by

$$m_k = t_e^k - k T_{k-1}(X, t_e) \quad (5.7)$$

The resulting first temporal moment, m_1 , calculated from each breakthrough curve is the mean arrival time of the tracer at the measurement point, and m_0 is unity for a normalized tracer concentration. The apparent seepage velocity v is determined from m_1 using:

$$v = \frac{x}{m_1(x)} \quad (5.8)$$

The second non-central temporal moments, m_2 , are calculated for each breakthrough curve. At a given measurement level, two apparent dispersion coefficients are computed, a macrodispersive, $D^*(x)$, and an effective dispersive one, $D^e(x)$:

$$D^*(x) = \frac{x^2 \langle m_2 \rangle - \langle m_1 \rangle^2}{2 \langle m_1 \rangle^3} \quad (5.9)$$

$$D^e(x) = \frac{x^2 \left\langle \frac{m_2 - m_1^2}{m_1^3} \right\rangle}{2} \quad (5.10)$$

in which $\langle \rangle$ denotes averaging over all probes in the same measurement level x , to which I refer as cross-sectional average in the following. In the given context, the apparent macrodispersion coefficient describes the solute spreading and mixing by analyzing the moments of the concentration BTCs averaged over all probes at that level. The effective dispersion coefficient, by contrast, is evaluated for each probe individually and may be averaged over the cross-section subsequently. That is, the effective dispersion coefficient is related to the spread observed in BTCs of single probes, whereas the macrodispersion coefficient includes the variability in the mean breakthrough time among the probes within a measurement level. The coefficients are denoted as apparent ones because they do not describe the rate of change of moments. Instead, they interpret the moments of the BTCs as if caused by one-dimensional transport with constant coefficients (*Cirpka and Kitaniadis, 2000a*).

The moment-derived apparent transport parameters are sensitive to small fluctuations in the measured concentrations. As an alternative, I fitted the analytical solution of the advection-dispersion equation with uniform coefficients to the locally obtained BTCs by adjusting the parameters v and D (*Kreft and Zuber, 1978*):

$$c_{sim}(t) = \frac{1}{2} \operatorname{erfc} \left(\frac{x - vt}{2\sqrt{Dt}} \right) \quad (5.11)$$

Strictly speaking, eq. (5.11) is the analytical solution for the residence concentration in a one-dimensional infinite domain with Heaviside initial condition. The correct analytical expression of the residence concentration for step-wise injection into the flux of a semi-infinite domain contains additional correction terms which become very small for column-scale Peclet numbers $Pe = xv/D > 10$ (*Kreft and Zuber, 1978*).

5.2.2 Heterogeneously packed porous medium (sandbox)

Two types of conservative tracer tests – with and without surfactant - are conducted in the heterogeneously packed sandbox. The steps involved in the preparation of the conservative test solution are given in Table 5.1.

5.2.2.1 Conservative tracer test with surfactant

Two thousand liters of degassed-deionized water is collected together in two containers with a volume of 1000 liters each. 40 liters of nonionic surfactant is added to the 2000 liters deionized water and mixed well. Sodium azide is added to the solution following a requirement of 0.1mmol/l of the solution. The pH of the water is brought to 10 by adding concentrated NaOH solution. The water is stirred using a mechanical stirrer during the addition of the NaOH solution so that it is uniformly mixed. Necessary amount of fluorescein is added to bring the tracer concentration of the surfactant solution to 100µg/l.

The heterogeneously packed porous medium in the sandbox is initially saturated with an alkaline surfactant solution without tracer, but other chemical properties remaining the same as that of the solution with tracer. The inlet chambers of the sandbox are completely flushed with the alkaline surfactant solution with tracer before introducing it into the heterogeneous porous medium. This is done by closing the valves from the hydraulic board to the outlet constant head tanks and simultaneously opening the valves from the inlet chamber to the inlet constant head tanks (Fig 5.8). Approximately 9liters of tracer solution is flushed through the inlet chambers, which has a total volume of 3.25 liters. Once a uniform tracer concentration is achieved in the inlet chambers, the valves to the inlet constant head tanks are closed and simultaneously the valves to the outlet constant head tanks are opened. This enabled the introduction of the tracer solution with a sharp step input into the sandbox.

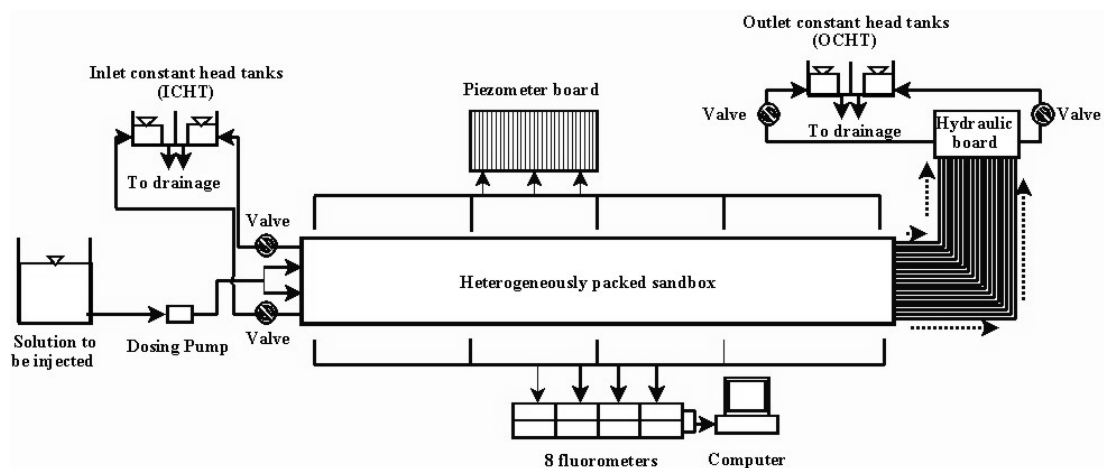


Fig 5.8 Sandbox experiment setup

The experiment is executed under constant flux conditions. The average specific discharge measured in the sandbox is 2.53×10^{-5} m/s with a measurement accuracy of 2%. Since a high accuracy of the flow rate is required, a dosing pump is used for the tracer

injection. The effective porosity of the porous domain as a whole is calculated to be 40%. The fluorescence intensity measurements are taken every minute and the values are averaged over ten measurements, i.e. over 10 minutes. On the sixth day, the experiment is terminated and approximately 900 liters of the tracer solution has been passed through the porous medium during this period.

5.2.2.2 Conservative tracer test without surfactant

An alkaline solution with and without tracer is prepared for the conservative test without surfactant. The preparation of solutions is similar to that explained in section 5.2.2.1 or in Table 5.1, but without the addition of surfactant. The procedure of the experiment is also identical to that explained in section 5.2.2.1.

The tracer solution is introduced into the porous medium under constant flux conditions. The discharge rates have been checked regularly and the average specific discharge measured during the course of the experiment is 1.35×10^{-5} m/s with a measurement accuracy of 1%. The overall porosity of porous domain is calculated to be 0.42, which is 2% higher than that calculated for the case with surfactant. Approximately 1300 liters of tracer solution is passed through the sandbox over a period of 18 days.

The fluorescence intensity of the tracer is measured continuously while the tracer solution is introduced into the domain. The fluorescence intensity is measured every 10 seconds and the values are averaged and stored every minute. The hydraulic heads are measured every four days during the progress of the experiment from the piezometer tubes connected to different locations in and at the outlet of the sandbox.

The fluorescence intensity data measured in this experiment is used in *Nowak (2004)* to estimate the hydraulic conductivity fields in the sandbox using inverse modeling.

5.2.2.3 Analysis of the measured fluorescence intensity data

The fluorescence intensity breakthrough curves obtained from the conservative tracer test is normalized based on its maximum and minimum fluorescence intensities (eq. 5.3). The normalized fluorescence intensity breakthrough curve is identical to the normalized tracer concentration breakthrough due to the linear dependency between them. The normalized tracer concentration breakthrough curves obtained from the conservative test are for a step input of the tracer. However, the analysis of dispersion by temporal moments is based on breakthrough curves resulting from a pulse-like injection moments (*Cirpka and Kitanidis,*

2000a). Therefore, I analyze, the temporal derivative of the breakthrough curves obtained from the conservative test.

The measured breakthrough curves are prone to considerable signal noise. The time-derivative of the measured signals are smoothed by convolution. In general, the convolution operation is defined as:

$$f(t) = \int_{-\infty}^{+\infty} a(t) \times b(t - \tau) d\tau \quad (5.12)$$

in which $a = \partial c / \partial t$ is the measured signal and b is the transfer function used for smoothing. Here, I use a Gaussian filter:

$$b(\tau) = \frac{1}{\sigma\sqrt{2\pi}} \exp\left(-\frac{\tau^2}{2\sigma^2}\right) \quad (5.13)$$

where σ is the specified standard deviation.

Subsequently, the smoothed breakthrough curves obtained after filtering are normalized with their respective zeroth temporal moments, m_0 . The normalized breakthrough curves of the fluorescence intensity are identical to those of concentration due to their linear dependency. From the normalized breakthrough curves, I compute the first (m_1) and second central temporal moments (m_{2c}). A convenient property of the convolution integral is that the first and second central moments of the original data and the transfer function are additive:

$$m_1(f) = m_1(a(t)) + \underbrace{m_1(b)}_{=0} \quad (5.14)$$

$$m_{2c}(f) = m_{2c}(a(t)) + \underbrace{m_{2c}(b)}_{=\sigma^2} \quad (5.15)$$

Hence the temporal moments of the original data are given from those of the filtered data minus those of the transfer function.

From each normalized breakthrough curve measured in the sandbox, the first temporal moment m_1 , the corresponding apparent seepage velocity v_a , the second central temporal moment m_{2c} , the corresponding apparent dispersion coefficient D_a , and the apparent dispersivity α_a are computed. For each travel distance, the arithmetic mean of the moments and the derived quantities over all probes within that cross-section are computed. These averages lead to apparent effective and macroscopic parameters.

5.3 Reactive Tracer Tests

The objective of conducting reactive tracer tests is to provide real data for comparing the reactive breakthrough curves predicted from the conservative tests. A reactive tracer test each is conducted in the homogeneously packed column and in the heterogeneously packed sandbox. The general procedure of a reactive tracer test is as follows (Fig 5.6):

- The porous medium is first filled with an acidic surfactant solution without tracer.
- Then the acidic surfactant solution without fluorescein is displaced by an acidic surfactant solution with fluorescein and identical pH. The tracer concentration in the solution is 100µg/l.
- Later an alkaline surfactant solution without tracer is flushed through the porous medium displacing the acidic surfactant solution with tracer. At regions where the alkaline solution interacts with the acidic solution, the pH becomes near-neutral and therefore fluorescein in the acidic solution emits fluorescence, which is measured by the fiber optic probes inserted into the porous medium (Fig 5.6).

The purpose of saturating the porous medium with an acidic surfactant solution without tracer prior to passing an acidic solution with tracer is to provide a coating of surfactant micelles onto the silica surfaces before tracer is introduced into it. Otherwise, fluorescein molecules which are hydrophobic at low pHs may sorb to sand particles.

5.3.1 Homogeneously packed column

Three types of solutions are used in the reactive test:

- Acidic surfactant solution without tracer,
- Acidic surfactant solution with tracer,
- Alkaline surfactant solution without tracer.

The steps involved in the preparation of the acidic solution with tracer and alkaline solution without tracer are given in Table 5.2. The core part of the reactive experiment is the displacement of the acidic surfactant solution containing fluorescein by an alkaline surfactant solution without fluorescein. Before introducing the alkaline surfactant solution into the homogeneously packed porous medium, it is flushed through the inlet chamber to have a uniform solution pH in the inlet. Once uniform alkaline pH is obtained in the inlet, the solution is passed through the porous medium (Refer section 5.2.1 for more technical information on flushing the inlet and introduction of solution into the porous medium).

Fluorescence intensity measurements are taken continuously at all the seven measurement levels during the course of the experiment. All the measurement levels are

equipped with eight locations for fluorescence intensity measurements, except level 3 and 7 where one fluorescence intensity measurement location is substituted by an arrangement to measure solution pH. The measurement interval for fluorescence intensity is 2 seconds and the measurements are averaged over every minute.

In the column, the acidic pH used in the reactive test is 4 and the alkaline pH is 10. The solution pH in the porous medium is measured using a luer-lock syringe system. Solution samples of volume 2ml are taken manually at regular intervals using a syringe and is transferred to a conical flask where the pH is measured using a micro-pH electrode. The purpose of measuring the solution pH in the porous medium is to qualitatively compare the increase in pH in the porous medium with that expected from the theory.

Table 5.2 Steps involved in preparing solutions for the reactive test

Step numbers	Reactive Test Solutions	
	Acid surfactant solution with tracer	Alkaline surfactant solution without tracer
Step 1	Collect deionized-(degassed [#]) water	Collect deionized-(degassed [#]) water
Step 2	Add surfactant (<i>surfactant conc. = 2% volume of the total solution volume</i>)	Add surfactant (<i>surfactant conc. = 2% volume of the total solution volume</i>)
Step 3	Add tracer (<i>Tracer conc. = 100μg/l</i>)	Add sodium azide (<i>Azide conc. = 0.1mmol/liter</i>)
Step 4	Add conc. HNO ₃ (<i>pH=4*</i>)	Add conc. NaOH (<i>pH=10</i>)

[#]Only for test in the sandbox.

*For reactive test in sandbox, the pH of the acid solution is pH3.

The experiment is carried out under constant flux conditions and the average specific discharge measured during the experiment is 7.04×10^{-5} m/s. The variation in the measurement of specific discharge is only 1%. A peristaltic pump is used to inject surfactant solutions into

the porous medium. The experiment lasted for 8.5 hours and approximately 17 liters of alkaline surfactant solution without tracer is passed through the porous domain.

The reactive breakthrough curves, which show the fluorescence intensity as a function of time, are normalised according to the maximum and minimum fluorescence intensities (eq. 5.3.) observed for the corresponding probes in the conservative tracer test.

5.3.2 Heterogeneously packed sandbox

Steps involved in preparing the solutions required for the reactive test in the sandbox are given in Table 5.2. Unlike the reactive test in the column, the acidic pH used in the sandbox is 3. This is because the pH stability of the pH4 solution is not maintained for a duration more than a couple of days. Therefore the pH3 solution, which exhibited better pH stability, is used as the acidic solution in the reactive test in the sandbox.

The alkaline surfactant solution is introduced into the heterogeneously packed porous medium after completely flushing out the acidic solution with tracer from the inlet. The experiment is conducted under constant flux conditions with an average specific discharge of 2.58×10^{-5} m/s and a measurement error of 2%. Approximately, 1900 liters of alkaline surfactant solution without tracer is passed through the sandbox over a period of 13 days. A dosing pump is used for injecting surfactant solutions into the sandbox.

The fluorescence intensity of the tracer is measured every minute and averaged over ten minutes. I normalized the fluorescence intensity breakthrough curves measured as a function of time using the maximum and minimum fluorescence intensity values (eq. 5.3) obtained from the conservative test with surfactant in the sandbox (section 5.2.2.1).

6 CHARACTERIZATION OF DILUTION AND MIXING IN POROUS MEDIA

In this chapter, dilution and mixing characterized from the results of conservative tests conducted in the homogeneously packed column and the heterogeneously packed sandbox are discussed. The results obtained in the heterogeneous porous medium are compared with the results from the numerical study of *Cirpka and Kitanidis, (2000a)*. A modified version of the spectral solutions derived by *Dentz et al., (2000a)* and *Fiori and Dagan (2000)* for macrodispersion and effective dispersion is applied to the observed results to check whether they are applicable to a porous medium packed with close-to-nature heterogeneities.

6.1 Homogeneous Porous Medium (Column Experiment)

In the conservative column test, an alkaline surfactant solution is displaced by another alkaline surfactant solution with identical pH (pH10), but with fluorescein dissolved in it. The fluorescein concentration of the tracer solution is 100 μ g/l. The experiment is carried out at a specific discharge of 7.13×10^{-5} m/s. (Please refer chapter 4 for details on experimental setup).

First temporal moments m_1 and second central temporal moments m_{2c} are calculated from the fluorescence intensity breakthrough curves obtained from the conservative test using methods mentioned in chapter 5. Values for all quantities that are estimated from the conservative breakthrough curves are given in Table 6.1.

Table 6.1 Parameters of interest calculated from the conservative breakthrough curves

Level No.	Probe No.	Norm. first temp. moment, m_1/m_0 [s]	Norm. second central temp. moment, m_{2c}/m_0 [s ²]	Apparent velocity, v_a [10^{-4} m/s]	Apparent Diffusion Coefficient of Mixing, D_a [10^{-7} m ² /s]	Apparent dispersivity, α_a [10^{-3} m]	Apparent Peclet Number, Pe_a
1	1	1406.81	35691.04	1.78	4.01	2.25	110.90
	3	1341.87	34793.23	1.86	4.50	2.42	103.50
	4	1540.29	58469.31	1.62	5.00	3.08	81.15
	5	1409.98	47540.96	1.77	5.30	2.99	83.64
	6	1394.26	47702.45	1.79	5.50	3.07	81.50
2	9	2867.76	81242.51	1.74	4.31	2.47	202.46
	10	2841.68	80882.05	1.76	4.41	2.50	199.68
	11	2904.40	86357.19	1.72	4.41	2.56	195.36
	12	2873.31	81715.58	1.74	4.31	2.47	202.06
	13	2871.05	72056.40	1.74	3.81	2.19	228.79
	14	2873.31	76022.34	1.74	4.01	2.30	217.20
	15	2908.41	78842.42	1.72	4.01	2.33	214.58
	16	2923.08	80041.64	1.71	4.01	2.34	213.50
3	17	4490.96	129010.97	1.67	4.01	2.40	312.67
	18	4306.57	156362.92	1.74	5.51	3.16	237.22
	20	4281.99	148116.93	1.75	5.31	3.03	247.58
	21	4248.73	136511.39	1.77	5.01	2.08	264.47
	22	3948.36	295584.54	1.90	13.50	7.11	105.48
	23	4284.43	148370.92	1.75	5.31	3.03	247.44
	24	4389.76	120484.59	1.71	4.01	2.34	319.87
4	25	5842.75	219640.25	1.71	5.51	3.22	310.85
	26	5932.88	196549.00	1.69	4.71	2.79	358.17
	27	6095.62	181462.03	1.64	4.01	2.44	409.52
	28	6040.39	176574.13	1.66	4.01	2.42	413.27
	29	5946.99	206368.00	1.68	4.91	2.92	342.75
	30	5969.61	191712.86	1.68	4.51	2.69	371.77
	31	5842.75	219640.25	1.71	5.51	3.22	310.85
	32	6040.39	185389.77	1.66	4.21	2.54	393.62

Level No.	Probe No.	Norm. first temp. moment, m_1/m_0 [s]	Norm. second central temp. moment, m_{2c}/m_0 [s ²]	Apparent velocity, v_a [10^{-4} m/s]	Apparent Diffusion Coefficient of Mixing, D_a [10^{-7} m ² /s]	Apparent dispersivity, α_a [10^{-3} m]	Apparent Peclet Number, Pe_a
5	33	7161.18	324627.25	1.75	6.91	3.96	315.95
	34	6542.71	426821.36	1.91	11.90	6.23	200.59
	35	7060.06	320077.94	1.77	7.11	4.01	311.45
	36	7286.41	272634.32	1.72	5.51	3.21	389.47
	37	7482.68	247001.38	1.67	4.61	2.76	453.36
	38	7202.44	349400.82	1.74	7.31	4.21	296.94
	39	7394.16	274560.29	1.69	5.31	3.14	398.26
	40	6315.57	438709.14	1.98	13.60	6.87	181.84
6	41	8849.44	369976.57	1.70	6.01	3.54	423.34
	42	8998.07	291796.67	1.67	4.51	2.70	554.94
	43	9063.32	298189.95	1.66	4.51	2.72	550.95
	44	8928.45	348341.91	1.68	5.51	3.28	457.69
	45	8923.14	385612.94	1.68	6.10	3.63	412.97
	46	8615.62	460797.51	1.74	8.11	4.66	322.18
	47	9085.27	333692.23	1.65	5.01	3.03	494.72
	48	9008.88	325345.46	1.67	5.01	3.01	498.92
7	49	9210.41	612613.97	1.90	12.00	6.32	276.95
	50	9308.39	737717.59	1.88	14.00	7.45	234.90
	51	9259.14	777909.96	1.89	15.00	7.94	220.42
	52	8798.38	1067777.21	1.99	24.00	12.10	145.00
	54	9642.28	1405437.78	1.81	24.00	13.20	132.31
	55	10005.58	1112452.55	1.75	17.00	9.72	179.98
	56	9562.72	799852.63	1.83	14.00	7.65	228.66
8	57	11627.75	943740.57	1.72	12.00	6.98	286.53
9	58	10810.71	859973.69	2.41	23.00	9.57	271.80

6.1.1 First moments and apparent velocities

The first temporal moment m_1 normalized by its zeroth moment m_0 gives the mean travel time t_{50} of the tracer from the injection to the observed point. For moments calculated from normalized concentration breakthrough curves, as in our case, the zeroth moments are equal to unity. Therefore, the first temporal moments calculated here corresponds to the mean arrival time. Hereafter, when temporal moments of order more than zero are discussed, it corresponds to the moments normalized by the zeroth moments. In an ideal homogeneous porous medium, the first temporal moments are expected to increase linearly with distance. But in reality, it is difficult to produce a perfect homogeneous medium. Therefore, one may not observe a perfect linearity between the temporal moments and the distance in a relatively-homogeneously packed porous medium as in our case (Fig 6.1). In the experiment mentioned here, the first temporal moments increased almost linearly with distance. The deviation of the locally obtained first temporal moments from their mean value, which is the non-weighted cross-sectional average of all the values obtained in that measurement section, is very small in the column, except at locations 1.25m and 1.75m, indicating that the sand packing in the column is indeed relatively homogeneous.

A small gradient of first temporal moments indicate a large seepage velocity v and large gradients indicate lower seepage velocities, since the seepage velocity is effectively the product of the inverse of the first temporal moments and the distance of measurement location from the inlet:

$$v(x_1) = \frac{x_1}{m_1} \quad (6.1)$$

However, the cross-sectional specific discharge $\langle q_1 \rangle$, which is related to the gradient of the first moments, will be identical since the experiment is carried out under constant flux conditions.

$$\langle q_1 \rangle = \left\langle n_e \left(\frac{\partial m_1}{\partial x_1} \right)^{-1} \right\rangle \quad (6.2)$$

In the above expression, $\langle \rangle$ denotes the cross-sectional average that is approximated by taking the arithmetic mean of all probe-related measurements within a cross-section.

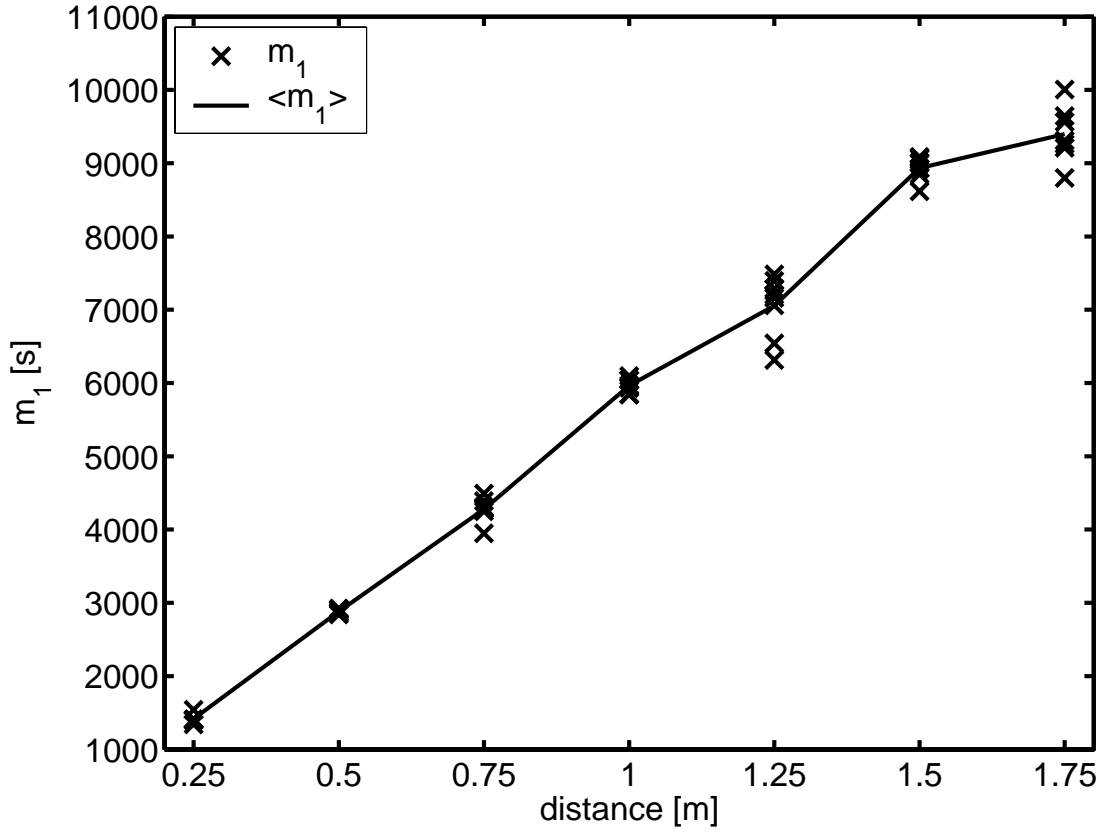


Fig 6.1 Locally determined values and arithmetic mean of first temporal moments m_1 .

In this study, two cross-sectional averages of velocity, a macroscopic velocity $v^*(x_1)$ which is computed by substituting the local first moment in eq. (6.1) by the cross-sectional average of the first moment, and an apparent effective velocity $v^e(x_1)$ which is the cross-sectional average of the locally determined apparent velocities within a measurement plane are considered:

$$v^*(x_1) = \frac{x_1}{\langle m_1(\mathbf{x}) \rangle} \quad (6.3)$$

$$v^e(x_1) = \left\langle \frac{x_1}{m_1(\mathbf{x})} \right\rangle \approx v^*(x_1) \left(1 + \frac{\sigma_{m_1}^2}{\langle m_1(\mathbf{x}) \rangle^2} \right) \quad (6.4)$$

where $\sigma_{m_1}^2$ is the variance of the first moment within the control plane. It is found that both v^* and v^e do not have uniform values within the porous medium (Fig 6.2). This is partially because eight measurement locations in a cross-section may not be enough to accurately compute the parameters in that cross section, although it is sufficient to give a general trend of the parameters. Since the velocity calculated is a path integrated quantity, the velocity values at each measurement section may vary depending upon the path taken by the solute stream

tube passing the probe at each location. Slight heterogeneities might have been induced during the packing of the column leading to velocity fluctuations. The coefficient of variation of seepage velocity, considering all measurement locations in the porous medium, is 5%. The effective velocity and macroscopic velocity have very similar values from the first measurement section onwards.

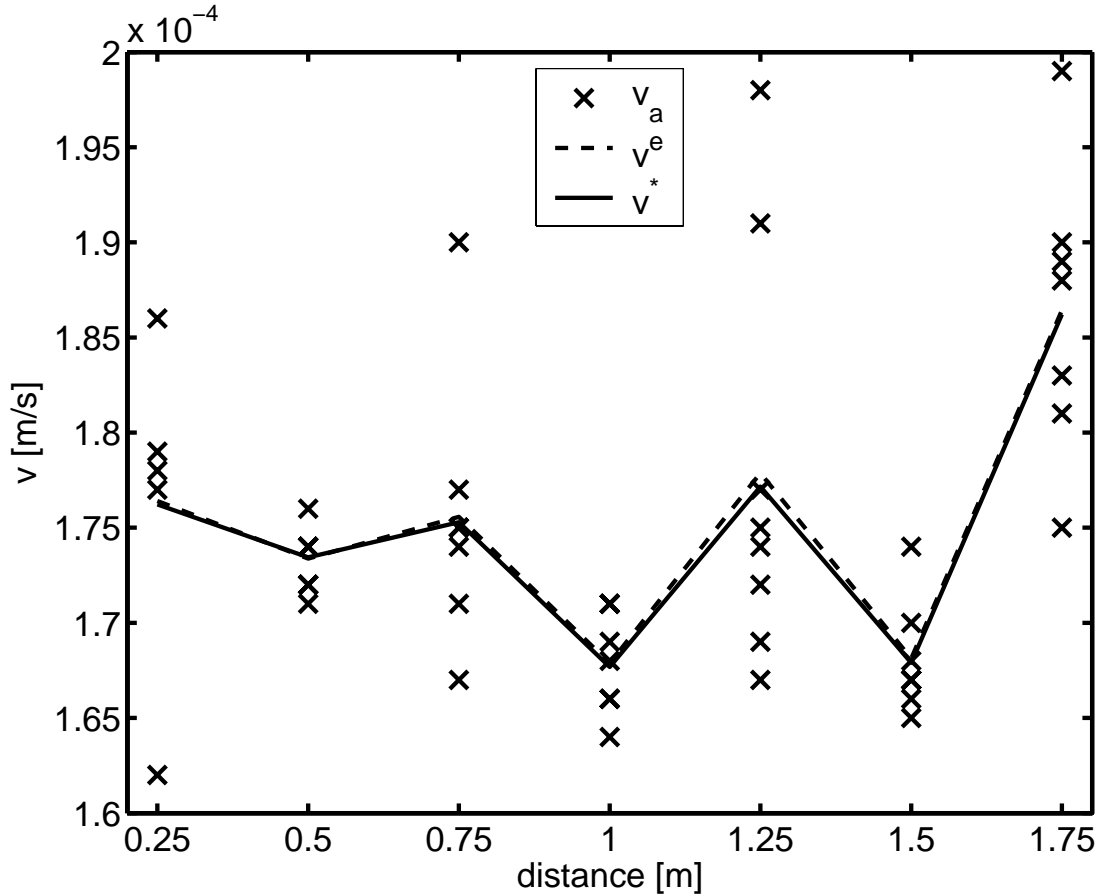


Fig 6.2 Probe-related apparent velocities $v_a(\mathbf{x})$, apparent effective velocity $v^e(x_1)$, and apparent macroscopic velocity $v^*(x_1)$ as function of travel distance.

6.1.2 Second central moments and apparent dispersivities

The normalized second central temporal moments m_{2c} , calculated from locally obtained breakthrough curves, correspond to the dilution of the plume at the respective locations (Cirpka & Kitanidis, 2000a; Cirpka, 2002). Being the variance of the locally observed breakthrough curve, a high value of m_{2c} indicates a wide breakthrough and thus reflects a smeared concentration distribution. The locally obtained second central moments $m_{2c}(\mathbf{x})$, the cross-sectional average of the locally evaluated second central moments $\langle m_{2c}(\mathbf{x}) \rangle$ and the

second central moment of the cross-sectionally averaged concentration $m_{2c}^*(x_1)$ are plotted in Fig 6.3. According to *Cirpka and Kitanidis (2000a)*, the effective second central moment, which is the cross-sectional average of the locally evaluated second central moments, is a relative measure for dilution and mixing in the measurement plane while the macroscopic second central moment, which is the second central moment of the cross-sectionally averaged concentration, is a measure for the spreading of the plume in that plane. As can be seen from the figure, the effective and macroscopic moments have very similar values except at the measurement sections of 1.25m and 1.75m. The similarity in values of the effective and macroscopic second central moments is expected for homogeneous porous medium like the one discussed here. It is known from theory that the macroscopic second central moment, which describes the spreading, consists of the actual dilution given by the effective second central moment and the variance of the first temporal moment that shows the irregularity of the advancing plume front. As can be seen from Fig 6.1, the first moments had relatively high variation at distance of 1.25m and 1.75m, resulting in higher macroscopic second central moments at the said measurement sections. From the plots of first and second central temporal moments (Fig 6.1 and Fig 6.3), it is concluded that the packing between the distances of 1m and 1.25m, and 1.5m and 1.75m are relatively non-uniform in nature.

The dispersion coefficients computed from the observed breakthrough curves in the column showed similar behavior as that of the second central temporal moments (Fig 6.4). The apparent longitudinal dispersion coefficient is calculated for a normalized breakthrough curve using the following relation:

$$D_a(\mathbf{x}) = \frac{x_1^2 m_{2c}(\mathbf{x})}{2m_1^3(\mathbf{x})} \quad (6.5)$$

The apparent effective dispersion coefficient $D^e(x_1)$ is the cross-sectional average of the local apparent dispersion coefficients, and thus reflects the mean mixing at the control plane. The apparent macrodispersion coefficient $D^*(x_1)$ is derived from the cross-sectional averaged concentration and its second central moment $m_{2c}^*(x_1)$.

$$D(x_1) = \langle D_a(\mathbf{x}) \rangle = \left\langle \frac{x_1^2 m_{2c}(\mathbf{x})}{2m_1^3(\mathbf{x})} \right\rangle \quad (6.6)$$

$$D^*(x_1) = \frac{x_1^2 m_{2c}^*(x_1)}{2\langle m_1(\mathbf{x}) \rangle^3} \approx D^e(x_1) + \frac{x_1^2 \sigma_{m_1}^2(x_1)}{2\langle m_1(\mathbf{x}) \rangle^3} \quad (6.7)$$

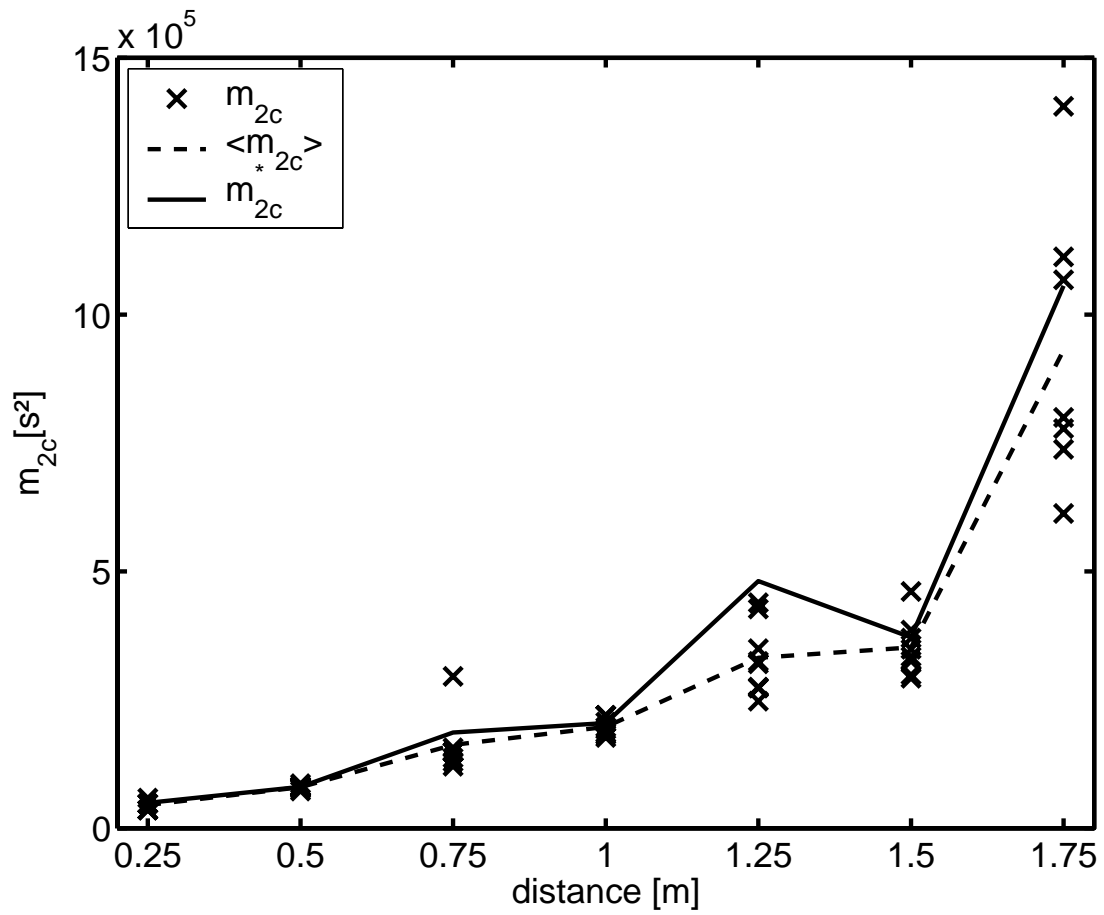


Fig 6.3 Locally determined second central temporal moments $m_{2c}(\mathbf{x})$, arithmetic mean within each measurement section $\langle m_{2c}(\mathbf{x}) \rangle$, and second central temporal moment of the cross-sectional averaged concentration $m_{2c}^*(x_1)$ as function of travel distance.

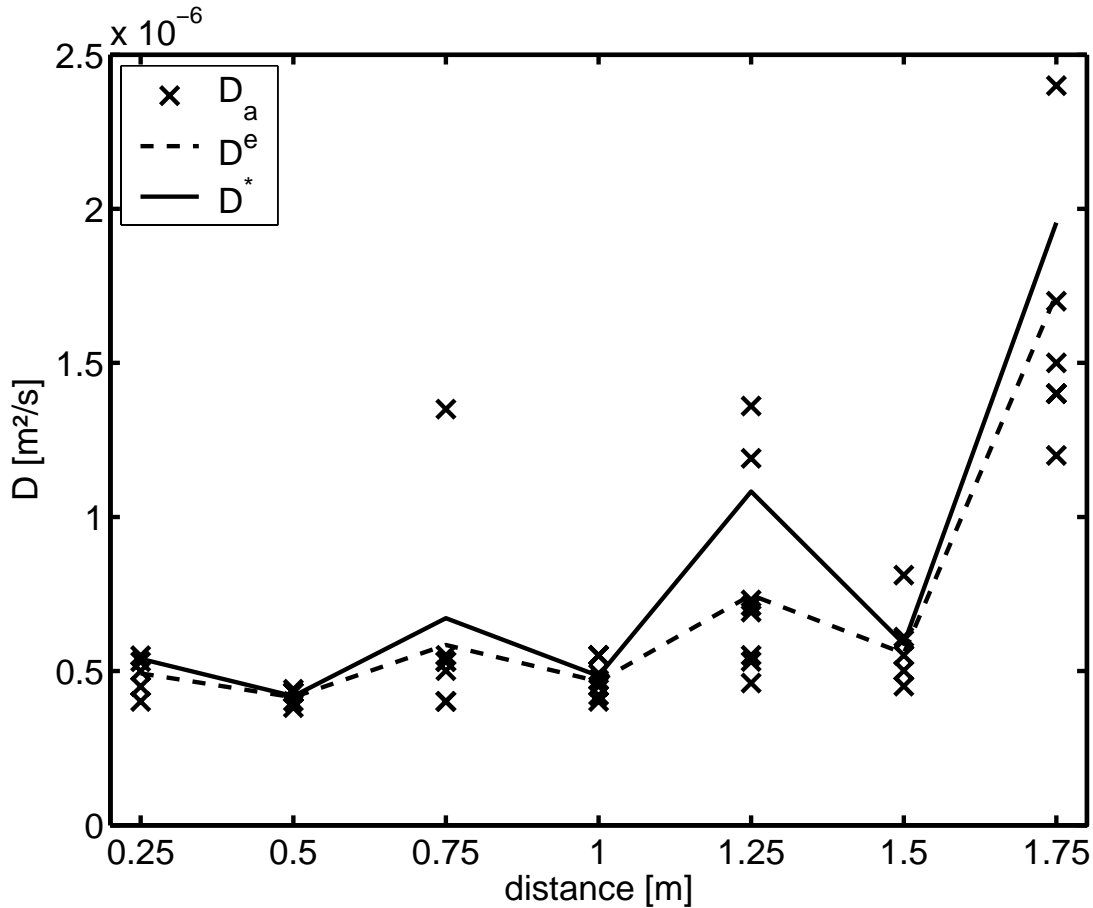


Fig 6.4 Locally determined apparent dispersion coefficient $D_a(\mathbf{x})$, apparent effective dispersion coefficient $D^e(x_1)$, and apparent macroscopic dispersion coefficient $D^*(x_1)$ as a function of travel distance.

The apparent effective dispersion coefficient $D^e(x_1)$ is a measure of mean dilution, whereas the apparent macrodispersion coefficient $D^*(x_1)$ also quantifies the combined effects of dilution and spreading. Since spreading of the tracer plume is characterized by the variance in the arrival time of the tracer front, sections with higher variance in the mean arrival time (1.25m and 1.75m) as observed in Fig 6.1 are the sections where the effective and macroscopic dispersion differ significantly. Nonetheless, the values for effective and macroscopic dispersion coefficients are in the same range implying that the spreading due to heterogeneities in the packed sand column are not very significant. The dispersion coefficients calculated within the porous medium are within the range of $4 \times 10^{-7} m^2/s$ and $2.4 \times 10^{-6} m^2/s$. The effective dispersion coefficients have values in the range of $6 \times 10^{-7} m^2/s$ until a distance of 1.5m and then it increases to a value of $1.5 \times 10^{-6} m^2/s$, implying that enhanced mixing has taken place between 1.5m and 1.75m. As can be seen from Fig 6.1, the gradient of the cross-

sectional average of first temporal moments between the mentioned distance is small, implying high velocities in this region. High velocities together with the heterogeneities in this region has given rise to a more spread tracer front, which in turn enhances the dilution and mixing of the tracer due to effects of transverse dispersion that smoothes out the fingering of the tracer front. This answers the increase of effective second central temporal moment and the effective dispersion coefficient in this region. In reality, dilution can only increase with distance. But in Fig 6.4, dilution is shown to have slightly lower values when compared with upstream values. This is observed because not the whole tracer front is sampled, instead it is sampled only at eight locations in each measurement section. Therefore a measured streamline that has undergone significant dilution upstream may not be sampled by the probe downstream as the respective streamline may bypass all probes. That is, the figure only provides a general behavior of dispersion coefficients in the porous medium.

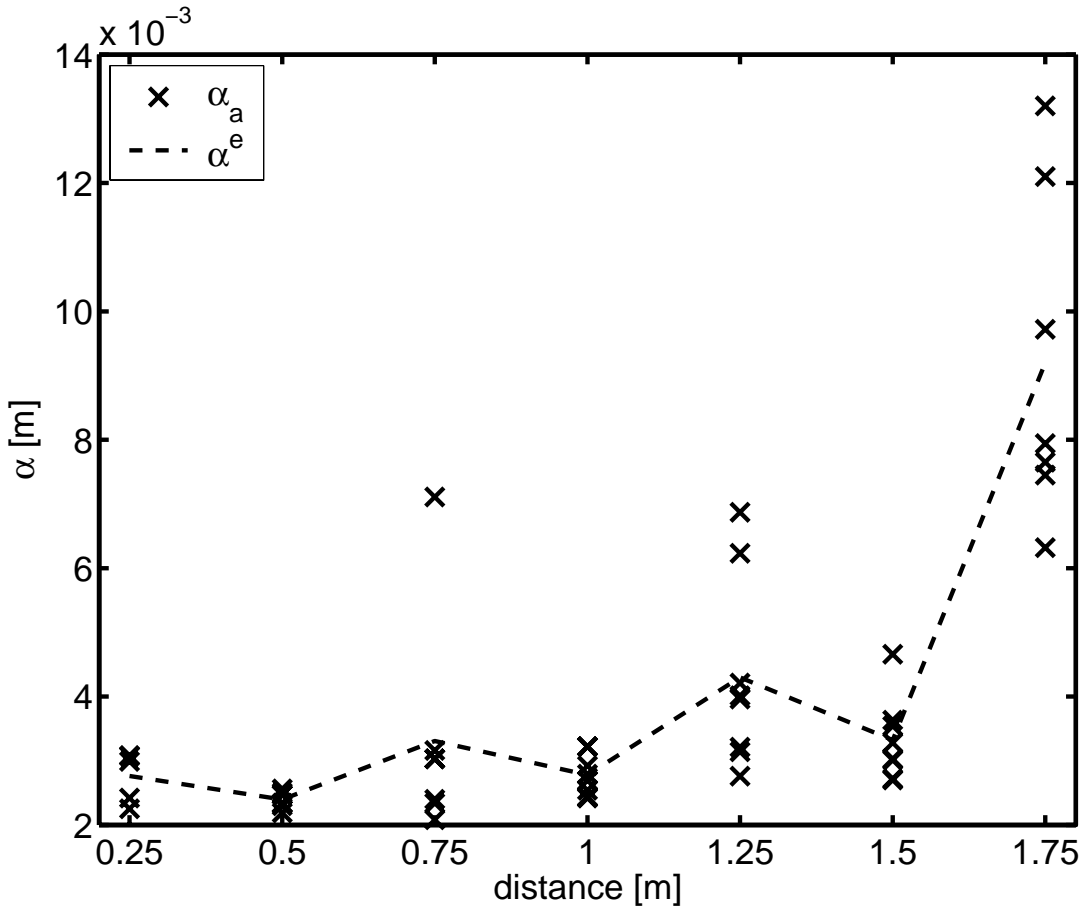


Fig 6.5 Locally determined apparent longitudinal dispersivity $\alpha_a(\mathbf{x})$, and apparent effective dispersivity $\alpha^e(x_1)$ as a function of distance.

The longitudinal dispersivities calculated for the porous medium show a behavior similar to that of dispersion coefficients (Fig 6.5). The apparent local longitudinal dispersivity values ranged between 2mm and 13mm. Ignoring the dispersivity values at 1.75m, the average apparent dispersivity value within the porous medium is about 3mm, which is in the range of the maximum grain size of the filled sand.

6.1.3 Apparent parameters at the outflow boundary

The measurement accuracy of the relevant quantities for the section at 1.75m is given in Table 6.2. The first temporal moment and the apparent velocity, which is inversely proportional to the first moment, are estimated with the highest accuracy of 4%. Other quantities have a measurement accuracy in the range of 25%. The macroscopic dispersion coefficient at this section is 1.14 times larger than the effective dispersion coefficient.

Table 6.2 Accuracy and variability of quantities of interest (Column test)

Variable	Value	SD	CV
$\langle m_1 \rangle$	$9.4 \times 10^3 \text{s}$	$3.54 \times 10^2 \text{s}$	0.04
$\langle m_{2c} \rangle$	$9.31 \times 10^5 \text{s}^2$	$2.55 \times 10^5 \text{s}^2$	0.27
$\langle v_a \rangle$	$1.86 \times 10^{-4} \text{m/s}$	$7 \times 10^{-6} \text{m/s}$	0.04
$\langle D_a \rangle$	$1.71 \times 10^{-6} \text{m}^2/\text{s}$	$4.55 \times 10^{-7} \text{m}^2/\text{s}$	0.27
$\langle \alpha_a \rangle$	9.2mm	2.39mm	0.26
$\langle Pe_a \rangle$	202.6	48.31	0.24
v^*	$1.86 \times 10^{-4} \text{m/s}$		
D^*	$1.95 \times 10^{-6} \text{m}^2/\text{s}$		
α^*	10.5mm		

SD is the standard deviation and CV is the coefficient of variation

6.2 Heterogeneous Porous Medium (Sandbox Experiment)

The procedure for the conservative test is identical to that in the column, but without surfactant. An alkaline solution (pH10) without tracer that initially saturated the heterogeneously packed sandbox is displaced by an alkaline solution with Fluorescein (tracer concentration = $100\mu\text{g/l}$). The experiment is carried out under constant flux conditions with a specific discharge of $1.35\times 10^{-5}\text{m/s}$. The close-to-nature heterogeneities in the sandbox are made of four sand types. (Please refer chapter 4 for details on experimental setup). The full length image of the sandbox is given in Fig 6.6 a, and the sketch of the distribution of different sand types in the sandbox is given in fig 6.6 b.

6.2.1 First moments and apparent velocities

The first normalized temporal moment m_1 of a breakthrough curve is the mean travel time from the injection to the observation point. Fig 6.6 c shows a contour plot of the first moment in the experimental domain, evaluated by interpolating the probe-related values. The shape of contour lines gives a general understanding of how the tracer plume propagates through the heterogeneously packed sandbox. The dark-shaded regions correspond to early tracer breakthrough, while the light-shaded regions mark late breakthrough. The flow field may be explained best by dividing the experimental domain into five sections ranging from 0-2m, 2-5m, 5-10m, 10-12m, and 12-14m, respectively.

The tracer plume is introduced evenly along the inflow boundary. In the first 2m, it travels faster in the upper regions than at the bottom of the domain. This is due to the presence of lowly conductive sand at the bottom. Subsequently, between 2m and 5m, the plume travels faster in the upper and lower regions of the sandbox, while the flow is slower in the middle. The travel-time pattern observed in the region cannot be explained by the conductivity of the sand in the region alone, as the travel time is an integrative measure of the velocity and thus affected by the conductivity sampled by the plume over the entire travel distance. Later on, until a distance of 10m, the plume flows faster through the middle of the domain. Within this section, two regions with low permeability can be identified. One low-permeability region lies between 8m and 9m and is located at the top of the experimental domain, while the other region is at the bottom of the domain between the distances 7m and 10m. At about 10m, the plume bifurcates with fast flowing arms in the upper and lower regions of the sandbox until a distance of 12m. The upper arm is relatively faster than the lower arm due to the presence of low permeable sand layers at the lower section of the domain at 12m. In the section between 12m and 14m, the flow converges towards the middle of the domain since relatively high

permeable sand layers are present in this region. It can be seen that the flow through the upper region between 13m and 14m is extremely slow.

As mentioned earlier, the first temporal moment in a homogeneous porous medium increases linearly with distance, while that in a heterogeneous medium exhibits deviations from the linear behavior. Fig 6.7(top) shows the normalized first temporal moments computed from the locally measured breakthrough curves and their cross-sectional averages at all measurement profiles. Fig 6.7(top) includes the averaged first temporal moment which increases with distance, but does not grow in a perfectly linear fashion. This may result partially from approximating the true cross-sectional average by the arithmetic mean of only a few point measurements. However, even the true cross-sectional average in a heterogeneous porous medium need not have to increase linearly. A uniform quantity in the given setup, like in the column, is the mean specific discharge which is related to the gradient of the first moment by:

$$\langle q_1 \rangle = \left\langle n_e \left(\frac{\partial m_1}{\partial x_1} \right)^{-1} \right\rangle \quad (6.8)$$

in which $\langle \rangle$ denotes the cross-sectional average. From eq. (6.8), it is clear that the mean gradient of the first moment is higher in regions with higher spatial variability.

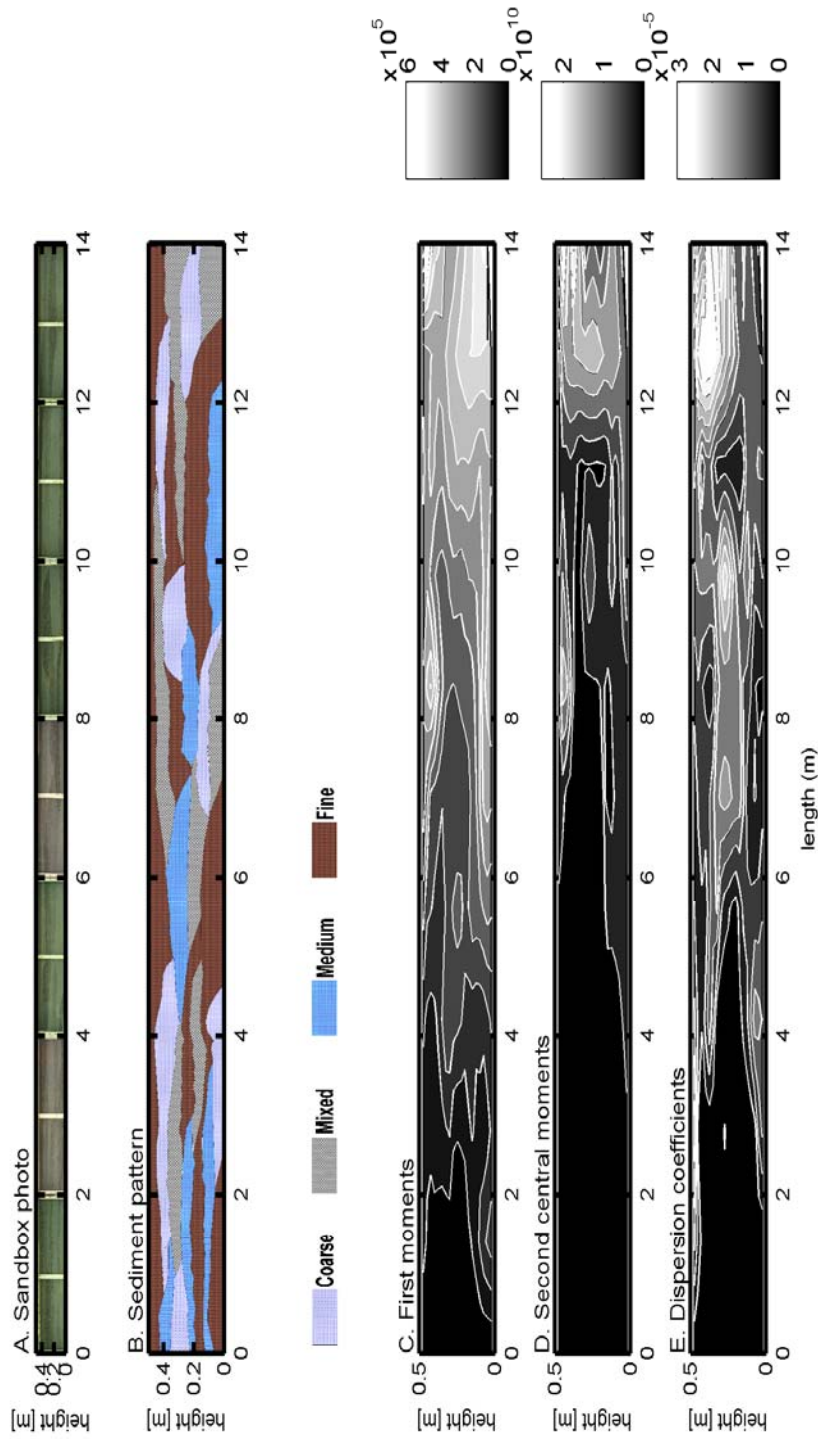


Fig 6.6 Distribution of sand types and quantities of interest determined in the sandbox. a) full length photo of sedimentation pattern in the sandbox. b) distribution of various sand types in the sandbox. c) two-dimensional distribution of normalized first temporal moments m_1 in the sandbox. d) two-dimensional distribution of normalized second central temporal moments m_{2c} in the sandbox. e) two-dimensional distribution of apparent dispersion coefficients D_a in the sandbox.

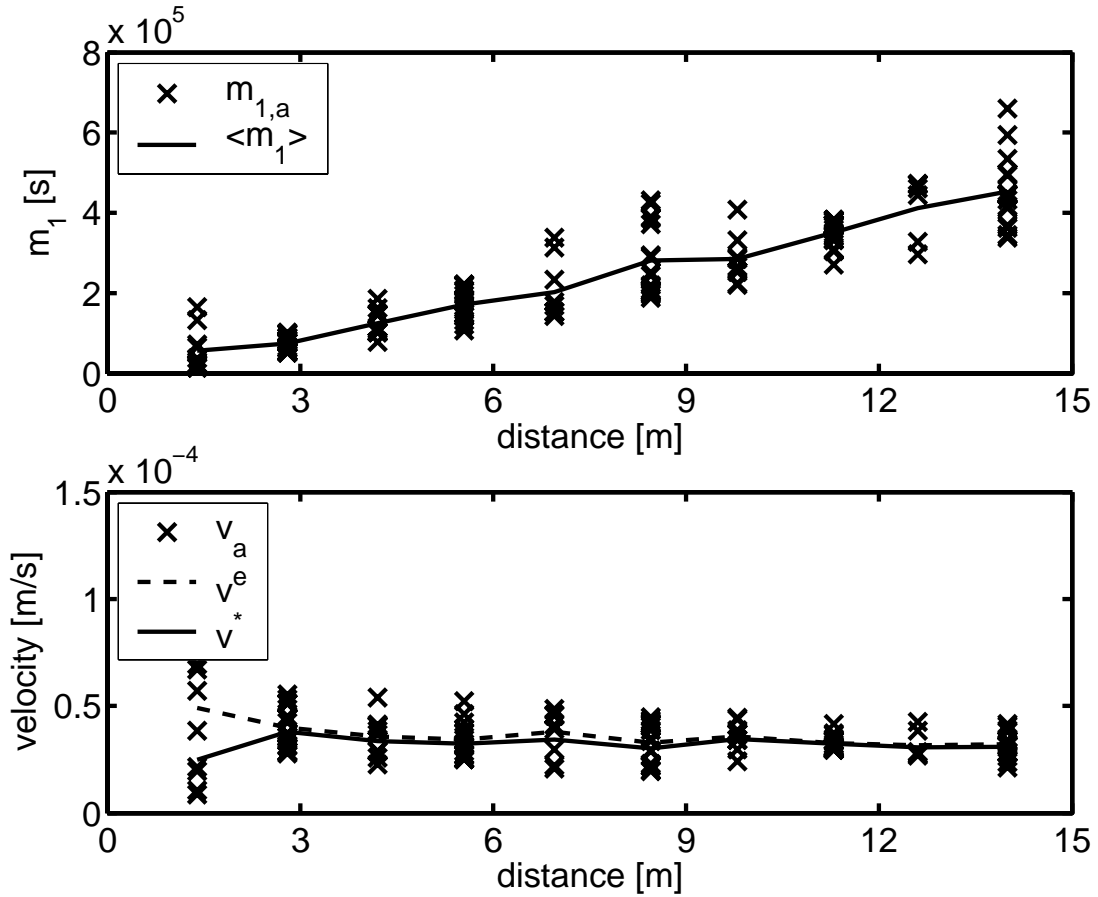


Fig 6.7 Normalized first temporal moments and the various apparent velocities at each measurement plane as a function of travel distance in the sandbox. (top) locally determined values and arithmetic mean of first moments m_1 . (bottom) probe-related apparent velocities $v_a(\mathbf{x})$, apparent effective velocity $v^e(x_1)$, and apparent macroscopic velocity $v^*(x_1)$ as function of travel distance.

The variability in the first moments is caused by contrasts in hydraulic conductivity. Higher variability indicates higher mechanical spreading and leads to enhanced mixing. As can be seen in Fig 6.7(top), the sections with a larger variability in the breakthrough times were between 7m and 10m, and near the outlet, i.e., between 12m and 14m.

The spatial pattern of $v_a(\mathbf{x})$ is essentially the inverse of that of the first temporal moments, corrected for a linear trend. Fig 6.7 (bottom) shows the apparent velocities of all probes, indicated by markers, as function of the distance. The large variation in $v_a(\mathbf{x})$ observed near the inlet is due to the differences in the conductivities among the various sand types. At larger distances, $v_a(\mathbf{x})$ becomes more uniform because it is a path-averaged quantity, and also because transverse pore-scale dispersion smoothes fluctuations of the first moment.

The macroscopic velocity $v^*(x_1)$ (6.3) and the apparent effective velocity $v^e(x_1)$ (6.4) within a measurement plane are also considered. The second-order approximation of $v^e(x_1)$ in equation (6.4) is derived by a Taylor series expansion about $v^*(x_1)$. Here, $\sigma_{m_1}^2$ is the variance of the first moment within the control plane. Fig 6.7(bottom) includes both $v^*(x_1)$ and $v^e(x_1)$ as solid and dashed lines, respectively. At short distances, $v^e(x_1)$ is significantly larger than $v^*(x_1)$ because the first-moment coefficient of variation $\sigma_{m_1}/\langle m_1 \rangle$ is rather high. With increasing distance, $\sigma_{m_1}/\langle m_1 \rangle$ decreases, that is, the first moment becomes in relative terms more uniform. At large distances, both $v^*(x_1)$ and $v^e(x_1)$ converge to the same asymptotic value, namely the mean specific discharge divided by the mean porosity. The behavior of apparent velocity is very similar to that reported by *Cirpka and Kitanidis (2000a)*.

6.2.2 Second central moments and apparent dispersivities

Fig 6.6d shows the spatial pattern of second central temporal moments $m_{2c}(\mathbf{x})$ in the experimental domain, evaluated by interpolating the probe-related values. In general, the spatial distribution of $m_{2c}(\mathbf{x})$ exhibits a similar pattern as that of $m_1(\mathbf{x})$, although not all local maxima of the first moment confirm with pronounced maxima of the second central moment.

Fig 6.8(top) shows a plot of the local values $m_{2c}(\mathbf{x})$, the mean of the local values $\langle m_{2c}(\mathbf{x}) \rangle$ and the macroscopic second central moment $m_{2c}^*(x_1)$ as function of distance. In a homogeneous medium, $\langle m_{2c} \rangle$ and m_{2c}^* would be identical and increase linearly with distance. In a stationary heterogeneous system, $\langle m_{2c} \rangle$ is smaller than m_{2c}^* , and both quantities are expected to increase more than linearly at small distances while approaching a linear behavior at large distances. In a domain with rather small cross-sectional area, such as the present sandbox, the cross-sectional averages $\langle m_{2c} \rangle$ and m_{2c}^* may differ from their expected behavior. In general, Fig 6.8(top) shows an increase of both quantities with distance, however, m_{2c}^* decreases between 8.4m and 11.3m, and $\langle m_{2c} \rangle$ decreases between 9.8m and 11.3m. Obviously, there is a region of low velocity in the top of the domain between 8m and 10m. In this region, we find high values of the second central moment. Further downstream, the water that has passed through the low-conductivity zone flows through layers of higher conductivity so that the width of the plume with high $m_{2c}(\mathbf{x})$ -values decreases. Lateral exchange also contributes to a smoother $m_{2c}(\mathbf{x})$ -profile.

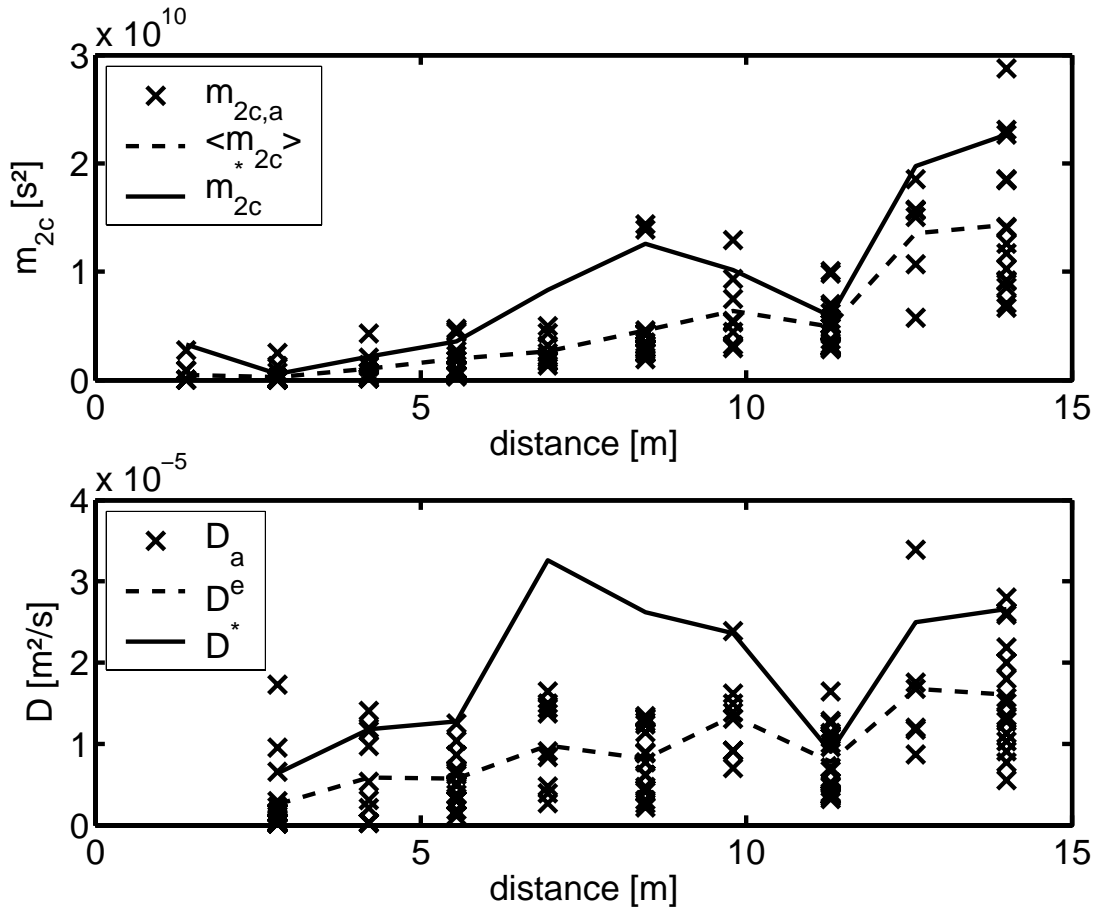


Fig 6.8 Normalized second central temporal moments and the various apparent dispersion coefficients at each measurement plane as a function of travel distance in the sandbox. (top): locally determined values $m_{2c}(\mathbf{x})$, arithmetic mean within each measurement plane $\langle m_{2c}(\mathbf{x}) \rangle$ and second central moment of the cross-sectional averaged concentration $m_{2c}^*(x_1)$ as a function of travel distance, (bottom) locally determined values $D_a(\mathbf{x})$, apparent effective dispersion coefficient $D^e(x_1)$, apparent macrodispersion coefficient $D^*(x_1)$ as a function of travel distance.

The macroscopic second central moment m_{2c}^* differs significantly from the mean of the local values $\langle m_{2c} \rangle$ in regions with high variance in first moments. This is the case between 7m and 10m, and towards the end of the domain. The large values of m_{2c}^* and $\langle m_{2c} \rangle$ between 12m and 14m indicate strong spreading and enhanced mixing.

Fig 6.6e shows a contour plot of the apparent dispersion coefficient $D_a(\mathbf{x})$ evaluated by interpolating the probe-related values. Relatively large apparent dispersion coefficients are found mainly in two regions in the sandbox: at the middle of the sandbox between 9m and 10m, and near the top of the sandbox between 12m and 14m. These regions may be addressed

as regions with enhanced mixing. Fig 6.8(bottom) shows the locally determined apparent dispersion coefficients $D_a(\mathbf{x})$, the apparent effective dispersion coefficient $D^e(x_1)$ (eq. 6.6), and the apparent macrodispersion coefficient $D^*(x_1)$ (eq. 6.7) as function of travel distance. The locally estimated apparent dispersion coefficients $D_a(\mathbf{x})$ range between $1.8 \times 10^{-7} \text{ m}^2/\text{s}$ and $3.39 \times 10^{-5} \text{ m}^2/\text{s}$. A general increase with distance can be observed which is evident in the profile of the apparent effective dispersion coefficient $D^e(x_1)$. The apparent macroscopic dispersion coefficient $D^*(x_1)$ is considerably higher than $D^e(x_1)$ in regions with higher variability in m_l . Overall, $D^*(x_1)$ is about 1.5 times larger than $D^e(x_1)$.

Fig 6.9(top) shows the contour plot of the apparent dispersivity $\alpha_a(\mathbf{x})$ evaluated by interpolating the locally obtained values. It can be noticed that the two-dimensional distribution of apparent dispersivities are very similar to that of the dispersion coefficients. Plots of apparent dispersivities $\alpha_a(\mathbf{x})$ and its cross-sectional averages $\alpha^e(x_1)$ and $\alpha^*(x_1)$ (Fig 6.9, bottom) are very similar to those of the apparent dispersion coefficients. Values determined at single probes range between 5.5mm and 860mm. The apparent effective dispersivity $\alpha^e(x_1)$ remains small (<10cm) until a distance of approximately 3m and increases more strongly from there onward. An asymptotic value is not reached within the experimental domain.

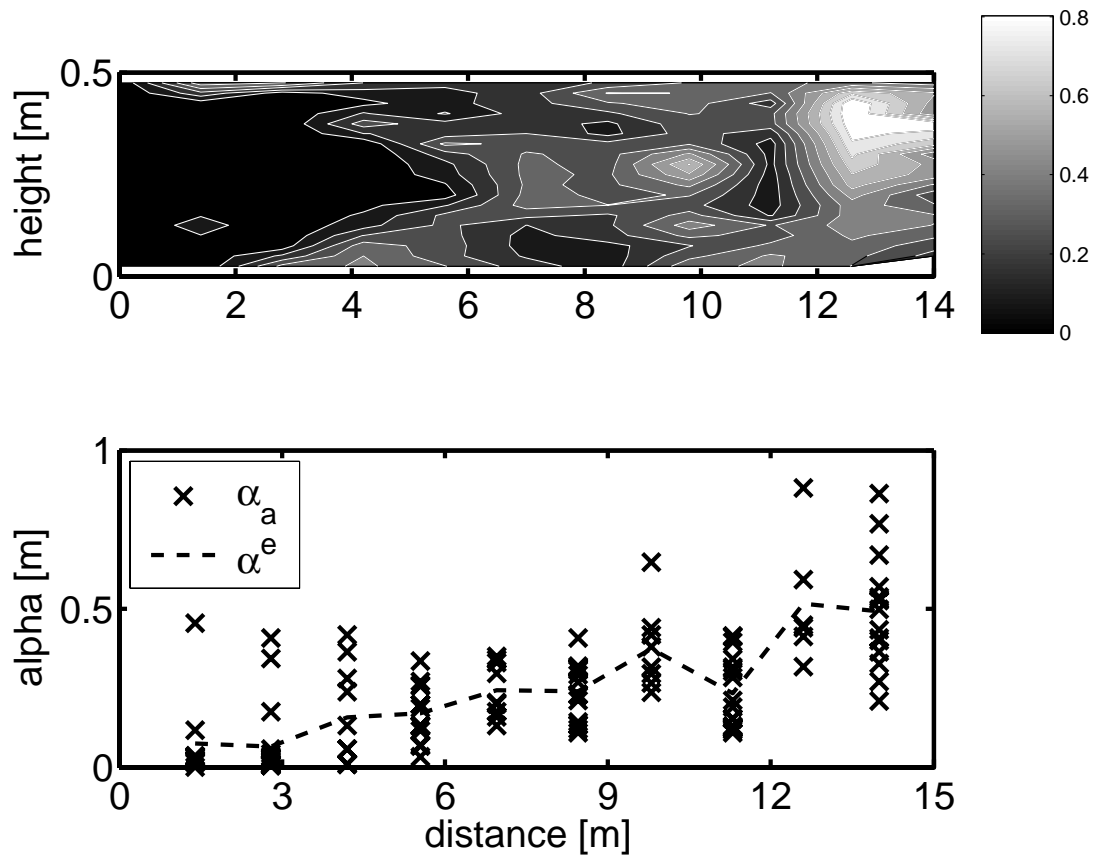


Fig 6.9 Distribution of apparent dispersivities in the sandbox. (top) two-dimensional distribution of apparent dispersivities in the sandbox. (bottom) locally determined apparent dispersivity α_a and apparent effective dispersivity α^e as a function of travel distance.

Regions with large contrast in hydraulic conductivity give opportunity to enhanced mixing. This may be explained by considering the section between 10m and 14m (Fig 6.10). The plot includes the distributions of the apparent dispersion coefficient (top), the first moment (middle), and the pattern of soil materials (bottom). In the following I discuss the influence of the material distribution on the propagation of the tracer plume, indicated by the travel-time distribution, and how it leads to enhanced mixing.

The layers in the sketch are numbered to simplify the discussion. Table 6.3 lists the hydraulic conductivity values of the various sand types, as obtained from permeameter studies. The coarse sand has the highest hydraulic conductivity followed by the mixed, medium, and fine sands. When the tracer plume enters the section shown in Fig 6.10, it finds a preferential flow path in the coarse-sand layer (layer 5 in the figure). Advection through the fine-sand layers 2 and 4 is significantly slower. The medium-sand layer 1 has a higher conductivity than the fine-sand layers. However, this particular lens is blocked by fine sand (layer 2) further downstream (12.1m to 13m), so that layer 1 is not efficient as a preferential

flow path. The water flowing through the coarse-sand layer 5 stays in this layer as long as possible. At distance 12.5m to 13m, most of the flow squeezes through the mixed-sand layer 3 and finally reaches the outlet. Flow velocities in the fine-sand layer directly above the preferential-flow region are very low. At the interface between layers 5 and 9, at the top of the domain, the strong contrast in hydraulic conductivity causes vertical gradients in the first moment. Here, transverse exchange of solutes leads to strong spreading of the breakthrough curves as quantified by the apparent dispersion coefficient $D_a(\mathbf{x})$. It may be worth noting that the hot spot of mixing is located in the coarse material. Here, the pore-scale dispersion coefficient is high because of high velocities and large grain sizes. In addition, the transverse diffusion distance is smaller in high-velocity regions. That is, narrow preferential flow paths can be identified as regions of enhanced mixing.

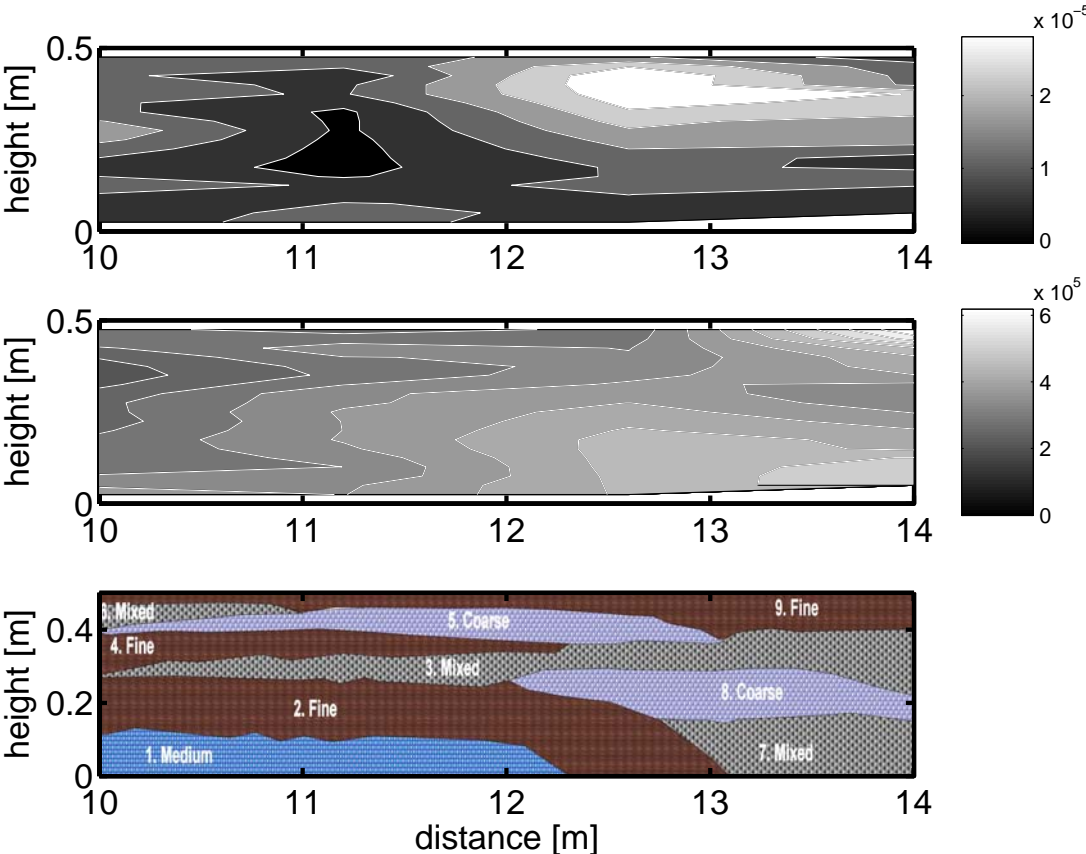


Fig 6.10 Detailed distributions in the section between 10m and 14m. (top): apparent dispersion coefficients; (middle): travel time; (bottom): sedimentation pattern in the sandbox.

Table 6.3 Grain size and hydraulic conductivity of sand types

Sand Type	Grain Size [mm]	Hydraulic conductivity [m/s]
Coarse sand	1.0mm – 2.5mm	$1.67 \cdot 10^{-2}$
Mixed sand	0.3mm – 1.2mm	$4.32 \cdot 10^{-3}$
Medium sand	0.0mm – 3.0mm	$9.09 \cdot 10^{-4}$
Fine sand	0.1mm – 0.8mm	$5.61 \cdot 10^{-4}$

6.2.3 Apparent parameters at the outflow boundary

The measurement accuracy of the variables at the outlet (distance=14m) is given in Table 6.4. Also a comparison of the averaged values to its macroscopic quantities is provided.

Table 6.4 Accuracy and variability of quantities of interest (Sandbox test)

Variable	Value	SD	CV
$\langle m_1 \rangle$	4.53×10^5 s	8.82×10^4 s	0.20
$\langle m_{2c} \rangle$	1.43×10^{10} s ²	6.40×10^9 s ²	0.45
$\langle v_a \rangle$	3.20×10^{-5} m/s	5.78×10^{-6} m/s	0.18
$\langle D_a \rangle$	1.60×10^{-5} m ² /s	6.82×10^{-6} m ² /s	0.43
$\langle \alpha_a \rangle$	0.49 m	0.17 m	0.35
$\langle Pe_a \rangle$	32.60	12.9	0.40
v^*	3.09×10^{-5} m/s		
D^*	2.66×10^{-5} m ² /s		
α^*	0.86 m		

SD is the standard deviation and CV is the coefficient of variation

It can be seen that the first temporal moment is the quantity that is determined with highest accuracy with coefficient of variation of 20%. Consequently, the velocity derived

from the first moment varies to a similar extent of 18%. The variability of second central temporal moments is 45%. Out of the derived quantities, the dispersion coefficient had the highest variability followed by the Peclet number and the dispersivity. The high variability in the dispersion coefficient indicates that a single measurement of a local breakthrough curve may not be sufficient to accurately distinguish between spreading and mixing. In general, the variability of measurements showed a trend similar to that mentioned in *Cirpka and Kitaniadis, (2000a)*. The macroscopic dispersion coefficient at distance = 14m is 1.66 times higher than the corresponding effective dispersion coefficient.

6.2.4 Comparison with results of linear stochastic theory

The expected second central moment of the averaged concentration m_{2c}^* can be estimated from the expected one-particle variance of displacements X_{11} and the variance of first moments $\sigma_{m_1}^2$ at an observation point from the two-particle covariance of displacements Z_{11} with zero initial separation by (see, e.g., *Rubin 2003*):

$$m_{2c}^*(x_1) = \frac{1}{\langle v_1 \rangle^2} X_{11}(\langle m_1(x_1) \rangle) \quad (6.9)$$

$$\sigma_{m_1}^2(x_1) = \frac{1}{\langle v_1 \rangle^2} Z_{11}(\langle m_1(x_1) \rangle) \quad (6.10)$$

in which $\langle m_1(x_1) \rangle$ is approximated to the first order by:

$$\langle m_1(x_1) \rangle = \frac{x_1}{\langle v_1 \rangle} \quad (6.11)$$

Dentz et al. (2000a) derived closed form expressions for X_{11} and Z_{11} in second-order stationary velocity fields using an Eulerian method. *Fiori and Dagan (2000)* came to identical expressions in a Lagrangian framework. In the spectral domain, these expressions are:

$$X_{ij}(t) = 2tD_{ij} + \int_{-\infty}^{\infty} \frac{(2\pi i \mathbf{v} \cdot \mathbf{s} + 4\pi^2 \mathbf{s}^T \mathbf{D} \mathbf{s})t + (\exp(-(2\pi i \mathbf{v} \cdot \mathbf{s} + 4\pi^2 \mathbf{s}^T \mathbf{D} \mathbf{s})t) - 1)}{(2\pi i \mathbf{v} \cdot \mathbf{s} + 4\pi^2 \mathbf{s}^T \mathbf{D} \mathbf{s})^2} S_{v_i v_j}(\mathbf{s}) d\mathbf{s} \quad (6.12)$$

$$Z_{ij}(t) = \int_{-\infty}^{\infty} \left(\frac{1 - \exp(-(2\pi i \mathbf{v} \cdot \mathbf{s} + 4\pi^2 \mathbf{s}^T \mathbf{D} \mathbf{s})t)}{4\pi^2 (\mathbf{v} \cdot \mathbf{s})^2 + 16\pi^4 (\mathbf{s}^T \mathbf{D} \mathbf{s})^2} + \frac{1 - \exp(-8\pi^2 \mathbf{s}^T \mathbf{D} \mathbf{s}t)}{8\pi^2 \mathbf{s}^T \mathbf{D} \mathbf{s} (2\pi i \mathbf{v} \cdot \mathbf{s} - 4\pi^2 \mathbf{s}^T \mathbf{D} \mathbf{s})} \right) S_{v_i v_j}(\mathbf{s}) d\mathbf{s} \quad (6.13)$$

in which \mathbf{s} is the vector of wave numbers, \mathbf{D} is the pore-scale dispersion tensor, i is the imaginary number, and $S_{v_i v_j}(\mathbf{s})$ is the power (cross-)spectral density function of the seepage

velocity components v_i and v_j which can be evaluated from the spectrum $S_{YY}(\mathbf{s})$ of the log-conductivity by (Gelhar & Axness, 1983):

$$S_{v_i v_j}(\mathbf{s}) = \left(J_i - \frac{\mathbf{s} \cdot \mathbf{J}}{\mathbf{s} \cdot \mathbf{s}} s_i \right) \left(J_j - \frac{\mathbf{s} \cdot \mathbf{J}}{\mathbf{s} \cdot \mathbf{s}} s_j \right) \frac{K_g^2}{n_e^2} S_{YY}(\mathbf{s}) \quad (6.14)$$

with the mean hydraulic-gradient vector \mathbf{J} and the geometric mean of the hydraulic conductivity K_g . The log-conductivity spectrum $S_{YY}(\mathbf{s})$ is the Fourier transform of the covariance function $R_{YY}(\mathbf{h})$, here defined by:

$$S_{YY}(\mathbf{s}) = \int_{-\infty}^{\infty} R_{YY}(\mathbf{h}) \exp(-2\pi i \mathbf{s} \cdot \mathbf{h}) d\mathbf{h} \quad (6.15)$$

in which \mathbf{h} is the distance vector.

A modified version of the closed form expression for m_{2c}^* derived by Dentz *et al.*, (2000a) is same as that given by Dagan (1984) at its asymptotic limits, which in its temporal form is represented as:

$$m_{2c,\infty}^* = \frac{2\lambda\sigma_Y^2 x}{\bar{v}^2} \quad (6.16)$$

where λ is the correlation length of the aquifer heterogeneity, and σ_Y^2 is the variance of log conductivity. The variance of first moments according to Dentz *et al.*, (2000a) could be written in the temporal form as given below:

$$\sigma_{m_1}^2 = \frac{2\lambda\sigma_Y^2\tau_{D_r}}{\langle v \rangle} \left(\sqrt{1 + \frac{2\pi x}{\langle v \rangle\tau_{D_r}}} - 1 \right) \quad (6.17)$$

where $\tau_{D_r} = \frac{\lambda^2}{D}$ is the dispersive time scale and D is the relevant dispersion coefficient.

Closed form expressions for ensemble and effective dispersion coefficients are derived for isotropic and anisotropic conditions of heterogeneity and pore-scale dispersion in Dentz *et al.*, (2000a).

The applicability of eqs. (6.9-6.15) to close-to-nature heterogeneities is tested by fitting the structural parameters of the covariance function $R_{YY}(\mathbf{h})$ as well as the value of an isotropic pore-scale dispersion coefficient to the measured data of m_{2c}^* and $\langle m_{2c} \rangle$. I assume two-dimensional flow and the anisotropic exponential model for the covariance function of log-conductivity fluctuations:

$$R_{YY}(\mathbf{h}) = \sigma_Y^2 \exp\left(-\frac{|h_1|}{\lambda_1} - \frac{|h_2|}{\lambda_2}\right) \quad (6.18)$$

in which the variance of log conductivity σ_Y^2 , and the two correlation lengths λ_1 and λ_2 are the structural parameters to be determined. In addition to the structural parameters, an isotropic pore-scale dispersion coefficient D is estimated. In order to ensure that the parameters have positive values, I estimate their logarithm. Then, the exponent of the estimated log parameter is the geometric mean μ_g of the parameter, and the exponent of the standard deviation of the log parameter may be denoted the factor of variation FV of the parameter.

A Levenberg-Marquardt method with prior information is used for the estimation of the parameters. The optimization routine is written as Matlab[®] script using periodic embedding and FFT techniques for spectral calculations. The prior geometric means μ_g and the factors of variation FV are given together with the fitted values in Table 6.5.

Table 6.5 Fitted parameters of linear stochastic theory.

Parameter	Prior		Posterior	
	μ_g	FV	μ_g	FV
σ_Y^2	2.4	2.72	2.45	1.43
λ_1	1.15m	1.88	1.43m	1.74
λ_2	0.04m	1.88	0.039m	1.77
D	$6 \times 10^{-9} \text{m}^2/\text{s}$	2.72	$8.24 \times 10^{-9} \text{m}^2/\text{s}$	2.04

The prior variance of log conductivity σ_Y^2 is estimated from the variability in the conductivity of the sand types used in the experiment. The prior values for the horizontal and transverse correlation lengths λ_1 and λ_2 are estimated from the known general pattern of materials in the box, while the prior mean of the pore-scale dispersion coefficient is estimated from typical transverse dispersion coefficients. The mean velocity was fixed to $3.59 \times 10^{-5} \text{m/s}$, which is the asymptotic value of $v^*(x_1)$ and $v^e(x_1)$ at the end of the domain.

The estimated parameters and their posterior factors of variation are listed in Table 6.5. The logarithm of the correlation length in direction of flow and the log variance of the log conductivity are strongly anti-correlated with a correlation coefficient of -0.91, while the logarithm of the pore-scale dispersion coefficient and the logarithm of the transverse correlation length are positively correlated with a correlation coefficient of 0.44. Other correlations among the parameters are negligible. Both correlations make physically sense. The asymptotic longitudinal dispersion coefficient scales with the product of the longitudinal

correlation length and the variance of log conductivity. In order to distinguish between the effects of these two parameters, data at distances in the range of the correlation length or smaller are needed. The data set, however, consists mainly of measurements at larger distances. Thus, we find the strong negative correlation between $\ln(\sigma_Y^2)$ and $\ln(\lambda_1)$. On the other hand, effective dispersion catches up with macrodispersion with the time scale of transverse pore-scale dispersion, $\tau_{D_T} = \lambda_2^2 / D$, see eq. (6.17). In macrodispersion, the pore-scale dispersion coefficient D is insignificant, and the transverse correlation length λ_2 has only a comparably small impact. Hence, the values of $\ln(D)$ and $\ln(\lambda_2)$ depend mainly on the $\langle m_{2c} \rangle$ -data, and the effect of increasing $\ln(\lambda_2)$ is to a certain extent similar to that of increasing $\ln(D)$.

The model fitted the experimental data except at distances between 12m and 14m where measured spreading and mixing was stronger than predicted by the model. The results are plotted in Fig 6.11, where the related error bars (standard deviation of the corresponding quantities calculated at each measurement plane) are shown together with the measured data. The fitted parameters are in the range of realistic values. The estimated local dispersivity calculated from the dispersion coefficient is 0.23mm, which is a typical value for transverse dispersivities of medium-size sand at the given velocity (*Cirpka et al., 2004*).

Given the small height of the domain, the agreement between model results and measured data is good. Stochastic theory yields ensemble averages. The cross-sectional average applied to the data fluctuates about the ensemble average because the cross-section is by far not large enough to ensure ergodicity. Nonetheless, the model fit shows the correct overall trend with realistic model parameters. Therefore it could be concluded that the expressions derived for effective dispersion and macrodispersion from stochastic theory are, in general, applicable to real systems.

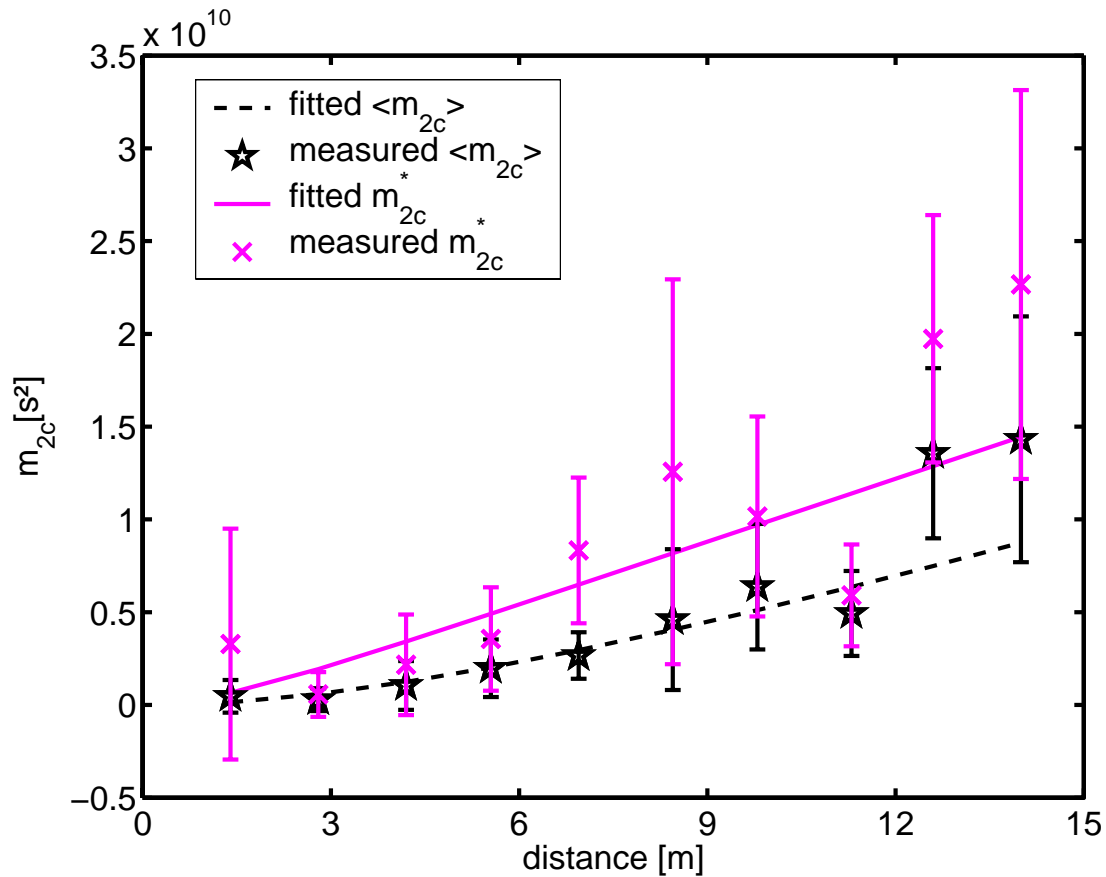


Fig 6.11 Second central moments as function of travel distance. Comparison between fitted results of linear stochastic theory and measured data. Solid line: fitted $m_{2c}^*(x_1)$; dashed line: fitted $\langle m_{2c}(\mathbf{x}) \rangle$; crosses: measured $m_{2c}^*(x_1)$; stars: measured $\langle m_{2c}(\mathbf{x}) \rangle$.

6.3 Conclusions

6.3.1 Homogeneous porous medium

- Macrodispersion and effective dispersion coefficients are in the same range as expected for experiments in a homogeneous porous medium.
- The apparent local dispersivities in the column experiment ranged between 2mm and 13mm, and the apparent effective dispersivities are in the range of 3mm, which is about the maximum grain size.
- The experiment served as the first step to confirming the efficiency of the point measurement technique and the selected tracer, Fluorescein.

6.3.2 Heterogeneous porous medium

- The strong increase of macrodispersion coefficients observed in the conservative tracer test in the heterogeneous porous medium is well known from previous studies.
- The difference between $D^*(x_1)$ and $D^e(x_1)$ is only a factor of about 1.5. The difference is not that pronounced because of the thin vertical extensions of the lenses.
- The relevant pore-scale dispersivity, estimated as 0.23mm, results in apparent effective dispersivities of 40cm at the end of the domain.
- The results qualitatively agree with the numerical studies by *Cirpka & Kitanidis (2000a)*.
- Linear stochastic theory is in agreement with results, but no ergodicity is guaranteed.

In general, the experimental studies verifies the applicability and limitations of the mixing-related theories in porous media from *Cirpka and Kitanidis (2000a)*, *Dentz et al. (2000a)* and *Fiori and Dagan (2000)* that are developed based on the stochastic approach.

7 PREDICTION OF MIXING-CONTROLLED REACTIVE TRANSPORT IN POROUS MEDIA FROM CONSERVATIVE TRACER TEST DATA

In this chapter, I compare reactive mixing predicted from the conservative tracer test with the results from the actual reactive mixing test. I investigate whether point-like measurements of concentrations provide reliable information of dilution and mixing as speculated by *Cirpka and Kitanidis (2000a, b)*. The chapter is structured as follows:

- Methodology to predict mixing-controlled reactive transport from conservative tracer test data,
- Results in the homogeneously packed column,
- Results in the heterogeneously packed sandbox.

7.1 Methodology to Predict Reactive Mixing from Conservative Tracer Test Data

In the reactive tracer test, the alkaline surfactant solution without tracer is injected into a porous medium saturated with an acidic surfactant solution with tracer. In a conservative test, an alkaline surfactant solution with tracer displaces another alkaline surfactant solution without tracer. In both tests, the fluorescence intensity of the tracer is measured at various locations in the porous media using fiber optic probes.

The Fluorescence intensities measured in both tests are normalized based on the maximum and minimum fluorescence intensity values observed at the corresponding measurement locations during the conservative tracer test:

$$I(t)_{norm} = \frac{I(t)_{meas} - I(t)_{min}}{I(t)_{max} - I(t)_{min}} = X_{base}(t) \quad (7.1)$$

where $I(t)_{norm}$ is the normalized tracer concentration. The fluorescence intensity measured in the conservative test is solely a function of the tracer concentration, and due to the linear relationship between fluorescence intensity and concentration, the normalized fluorescence intensity is identical to the normalized tracer concentration. The normalized tracer concentration in a conservative test is identical to the alkaline mixing ratio $X_{base}(t)$, which is defined as the ratio of the injected alkaline solution volume to the total solution volume at the observation point.

I account for the following processes leading to the measured fluorescence intensity in the reactive tracer test:

- The dispersive mixing of the two surfactant solutions at the displacement front,
- the acid-base reaction of the two surfactant solutions,
- the pH dependence of the specific fluorescence intensity of fluorescein.

The normalized fluorescence intensity in a reactive tracer test is a function of both the tracer concentration and the medium pH. Therefore, the relative fluorescence intensity due to the tracer concentration and the resultant pH at the observation point have to be estimated in order to predict the resultant fluorescence intensity in a reactive tracer test:

$$I_{res} = I_{rel}(X) \times I_{rel}(pH) \quad (7.2)$$

In the reactive tracer test, the solution with the tracer is displaced by the incoming solution unlike the case in the conservative test. Therefore, the tracer concentration in a reactive tracer test is predicted by $1-X(t)$, where $X(t)$ is the mixing ratio of the tracer, which is same as the normalized tracer concentration in the conservative test. Thus, the relative fluorescent intensity due to the tracer concentration may be formulated as:

$$I_{rel}(X_{base}) = 1 - X_{base}(t) \quad (7.3)$$

The change in the medium pH at the measurement location with time is a function of the ratio of the incoming alkaline solution to the total solution volume, which is called as the alkaline mixing ratio, X_{base} . In order to estimate the medium pH as a function of the alkaline mixing ratio $pH(X_{base})$, the buffer model developed to fit the titration curve between surfactant solution with pH4 and pH10 is used. The mixing ratio used to predict the resultant pH is the normalized concentration from the conservative test due to their expected identical nature. The titration test and the buffer model developed to fit the observed titration curve are explained in chapter 5, section 5.1.3.

Once the solution pH at the measurement location is estimated using the buffer model, the relative fluorescence intensity due to the medium pH is predicted using the relationship developed to fit the relative fluorescence intensity curve as a function of pH, which is explained in chapter 5, section 5.1.2. In this way, the relative fluorescence intensity due to the medium pH is determined:

$$I_{rel}(pH) = I_{rel}(pH(X(t))) \quad (7.4)$$

Substituting eqs. (7.2) and (7.3) in (7.4), the resultant fluorescence intensity in a reactive test is predicted as a function of both tracer concentration and medium pH.

7.2 Reactive Tracer Test in the Homogeneously Packed Column

In the reactive tracer test, the column is initially saturated with an acidic surfactant solution (pH4) with a fluorescein concentration of 100 μ g/l. Subsequently, an alkaline surfactant solution with pH10 is introduced into the column displacing the solution with the tracer. The experiment is conducted under constant flux conditions. The specific discharge in the column is 7.04×10^{-5} m/s with only a variation of 1%. A peristaltic pump was used to inject the test solutions into the porous medium, and approximately 17 liters of the alkaline surfactant solution was passed through the column. The duration of the experiment was 8.5 hours. The fluorescence intensity of the tracer within the porous medium was measured every two seconds during the passage of the alkaline surfactant solution without tracer, and the values are averaged for each minute and stored.

In the conservative tracer test, an alkaline surfactant solution with tracer replaces another alkaline surfactant solution without tracer that initially saturated the porous medium. The pH of both solutions is 10. The solution that is finally injected into the porous medium in a reactive test is the alkaline surfactant solution without tracer, and as per the requirements of the conservative test, such a solution is replaced by the alkaline surfactant solution with tracer in the conservative test. Therefore conservative test is conducted just after the reactive test. The advantages of this procedure are a reduction of solution waste, and the provision of a comparable state of the experimental setup in both tests.

The conservative tracer test is also conducted under constant flux conditions. The specific discharge during the experiment is measured to be 7.16×10^{-5} m/s and the variation in the measurements was 2%. During the experiment, 18 liters of alkaline tracer solution is passed through the column. The fluorescence intensity of the tracer was measured for identical intervals as that in the reactive tracer test.

The fluorescence intensities measured in both tests are normalized based on the maximum and minimum values of fluorescence intensity from the conservative test, for the corresponding locations. Since the specific discharge of the conservative test is larger than that of the reactive tracer test, the measured time in the conservative data is adjusted to make up for the difference. I reconstruct the reactive breakthrough curves observed in the reactive test by using the breakthrough curves obtained in the conservative test using the method described in section 7.1 and compared the predicted and the observed breakthrough curves. The relative difference of various moments is calculated as:

$$\text{relative difference} = \frac{\text{observed value} - \text{predicted value}}{\text{observed value}} \quad (7.5)$$

The cross-sectional average of the various moments calculated from the observed and the predicted reactive breakthroughs, and their relative differences are given in Table 7.1. It may be noticed that the zeroth moment m_0 , which is a relative quantity for the total product mass, is under-predicted until a distance of 1m and then starts to exceed the observed product mass from a distance of 1.5m onwards (see also Fig 7.1). Nonetheless the total mass could be predicted within an accuracy of 17%, which is still a good value. In Fig 7.2, the observed and predicted reactive breakthrough curves for three different locations in the porous medium are given. The under-prediction of product mass at small distances, in spite of fitting the peak time and height, is because of the reduced spread of the predicted curve compared to the observed one. Particularly, the observed tailing is stronger than the predicted one. Such behavior may be caused by slow sorption kinetics. At large distances, the effects due to retardation are more prominent, resulting in a lower peak concentration for the observed product. Since there is a clear trend of over-prediction of the total mass of the predicted reactive breakthroughs with distance, the better agreement in the product mass may be just coincidental.

Table 7.1 Relevant moments of the observed and the predicted reactive breakthrough curves and their relative differences.

A) Zeroth Temporal Moments, m_0 [s].						
<i>Distance From inlet [m]</i>	<i>Level Number</i>	Zeroth temporal moments, m_0 [s]			Relative difference = $1 - (\text{predicted}/\text{observed})$	
		<i>Observed</i>	<i>Predicted (without sorption)</i>	<i>Predicted (with sorption)</i>	<i>without sorption</i>	<i>with sorption</i>
0.25	1	2.39×10^2	2.03×10^2	2.61×10^2	0.133	-0.111
0.50	2	3.27×10^2	2.81×10^2	3.54×10^2	0.135	-0.091
0.75	3	4.67×10^2	4.10×10^2	4.39×10^2	0.101	0.022
1.00	4	4.50×10^2	4.52×10^2	4.91×10^2	-0.022	-0.117
1.25	5	6.64×10^2	6.57×10^2	5.50×10^2	0.011	0.169
1.50	6	6.94×10^2	7.35×10^2	5.95×10^2	-0.062	0.121
1.75	7	8.06×10^2	9.40×10^2	7.97×10^2	-0.173	0.010

B) Normalized First Temporal Moments, m_1/m_0 [s].						
<i>Distance From inlet [m]</i>	<i>Level Number</i>	Normalized first temporal moments, m_1/m_0 [s]			Relative difference = $1 - (\text{predicted}/\text{observed})$	
		<i>Observed</i>	<i>Predicted (without sorption)</i>	<i>Predicted (with sorption)</i>	<i>without sorption</i>	<i>with sorption</i>
0.25	1	1.39×10^3	1.39×10^3	1.47×10^3	0.000	-0.060
0.50	2	2.97×10^3	2.87×10^3	3.01×10^3	0.034	-0.013
0.75	3	4.39×10^3	4.23×10^3	4.47×10^3	0.035	-0.021
1.00	4	6.13×10^3	5.91×10^3	6.17×10^3	0.036	-0.006
1.25	5	7.25×10^3	6.94×10^3	7.36×10^3	0.044	-0.0015
1.50	6	9.14×10^3	8.76×10^3	9.27×10^3	0.041	-0.014
1.75	7	9.75×10^3	9.31×10^3	9.86×10^3	0.045	-0.012

C) Normalized Second Central Temporal Moments, m_{2c}/m_0 [s²].

Distance From inlet [m]	Level Number	Normalized second central temporal moments, m_{2c}/m_0 [s ²]			Relative difference = $1 - (\text{predicted}/\text{observed})$	
		Observed	Predicted (without sorption)	Predicted (with sorption)	without sorption	with sorption
0.25	1	6.86×10^4	2.61×10^4	5.59×10^4	0.433	-0.347
0.50	2	1.41×10^5	4.21×10^4	1.05×10^5	0.617	-0.003
0.75	3	2.92×10^5	7.76×10^4	1.61×10^5	0.581	0.110
1.00	4	2.31×10^5	1.11×10^5	2.09×10^5	0.403	-0.132
1.25	5	4.91×10^5	1.81×10^5	2.68×10^5	0.619	0.427
1.50	6	5.09×10^5	2.22×10^5	3.24×10^5	0.523	0.283
1.75	7	5.21×10^5	3.81×10^5	5.69×10^5	0.232	-0.115

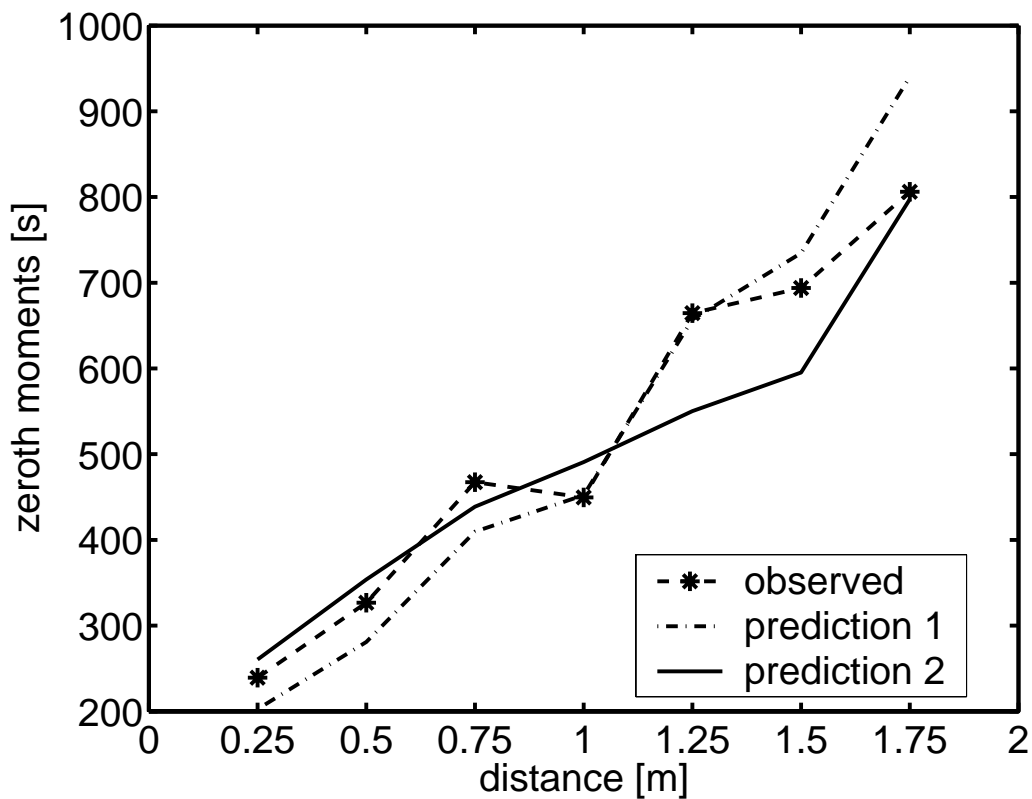


Fig 7.1 Cross-section averaged zeroth temporal moments for the different measurement sections in the column. Prediction 1 denotes to prediction without considering tracer sorption, and prediction 2 corresponds to one considering linear sorption of tracer.

The mean arrival time, which is indicated by the first temporal moment normalized by its zeroth moment, is predicted almost exactly for $x = 0.25\text{m}$; while the observed mean breakthrough time is about 3% later than the predicted one for $x = 0.50\text{m}$; and the relative difference increased to 4.5% until $x = 1.75\text{m}$. The observed temporal variance of the product breakthrough curve is, throughout the column, about 50% larger in the observations than in the predictions.

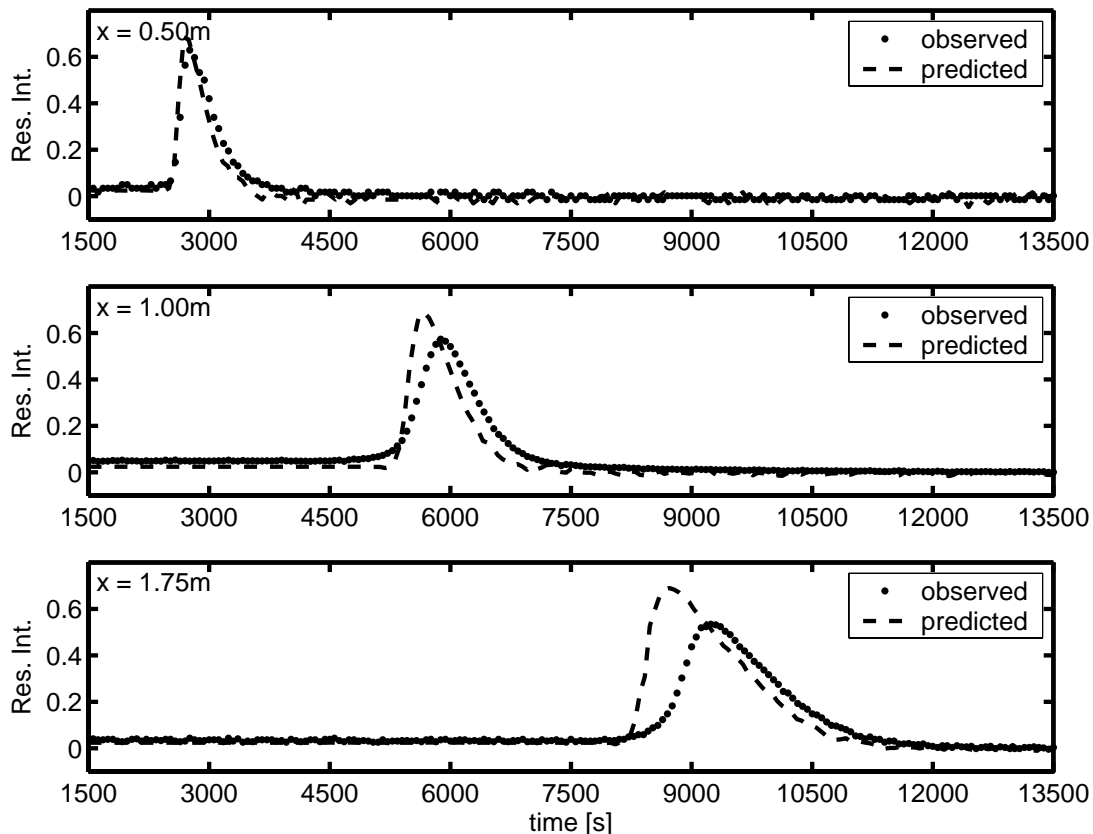


Fig 7.2 Resultant fluorescence intensity of the observed and the predicted (without considering tracer sorption) reactive breakthrough curves for three different measurement locations in the column.

From the batch tests conducted earlier (is discussed in chapter 5, section 5.1), it is known that the relative fluorescence intensity is only a function of tracer concentration for pH values over 8. The mixing ratio at which the pH becomes 8 is 0.32. In the reactive tracer test, the normalized concentration of tracer for an alkaline mixing ratio of 0.32 is 0.68. All the three predicted reactive breakthrough curves shown in Fig 7.2 have a normalized peak concentration of 0.68, while the observed breakthroughs have 0.63, 0.57 and 0.53 as their peak values at distances of 0.5m, 1m and 1.75m, respectively. From the figure, a clear trend of decreasing concentration peak with distance is observed. This would mean that the alkaline mixing ratio at which the medium pH becomes 8 is greater than 0.32 with increasing distance.

This implies that the increase in pH values with incoming alkaline solution volume is retarded at large travel distances. Therefore, from Fig 7.2, the alkaline mixing ratio at which the pH becomes 8 at a distance of 1.75m for the observed curve is calculated to be 0.47 (ie., 1-0.53) instead of 0.32.

If there had been no sorption of the tracer under acidic conditions, the declining part of the observed reactive breakthrough curve would perfectly match that of the predicted breakthrough curve since the tail of the peak depends not on pH. However, the observed tails are slightly shifted towards later times, indicating weak sorption of the tracer at low pH values. The retardation factor of the increasing and declining fronts is approximated by the ratio of the observed to the predicted breakthrough time t_{50} of half the peak concentration. For the breakthrough curve at 1.75 m shown in Fig 7.2, the resulting retardation factors are 1.08 and 1.02 for the injected and displaced front, respectively. The same analysis revealed no retardation for distances less than 0.5 m, neither for the injected nor the displaced front.

The model for the prediction of the reactive breakthrough curve is based on the assumption that the grain surface is totally inert with respect to the compounds considered in the multi-component reaction. Even though adding the surfactant reduced sorption of fluorescein to an extent that it could not be determined in batch tests, there might have been residual sorption, e.g., by an exchange between free floating micelles, containing fluorescein, and hemi-micelles attached to the grain surface. At the same time, acid-base reactions may have occurred on the quartz surface, so that both the tracer wash-out and the penetration of the alkalinity front were slightly retarded. As these mass-transfer processes include attachment and detachment of micelles, it is reasonable to assume slow kinetics. As a consequence, the early reactive breakthrough curve at $x = 0.5\text{m}$ would hardly be affected by kinetic mass-transfer, whereas the late breakthrough curves at $x = 1\text{m}$ and 1.75m showed some impact. To the best of my knowledge, no published results are available regarding the sorption of alkylpolyglucosides to silica surface, although transport and sorption of some other nonionic surfactants are reported (*Brinck et al., 1998; Danzer, 1999*).

Earlier, I attempted to quantify the sorption of fluorescein in the acidic surfactant solution onto quartz grains by independent batch tests, which are discussed in more detail in chapter 4, section 4.2.3. In these tests, I measured the concentration decrease in the surfactant solution after contact with the sand. The accuracy in the concentration measurement, however, was insufficient to quantify sorption leading to a retardation factor in the range of 1.1 or less in the column. Measuring the retardation of fluorescein in the surfactant solution

by conservative tracer tests under acidic conditions is not possible, because the fluorescence of the tracer is quenched under such conditions.

Since the results in the column indicate that the observed reactive breakthrough curves are sorbed, I have used AQUASIM, which is a computer program developed by Peter Reichert at EAWAG, Switzerland, for the identification and simulation of aquatic systems, to predict the observed reactive breakthrough curves from the conservative breakthroughs by taking sorption into consideration. For this purpose, it is important to identify the type of sorption and estimate reasonable sorption parameters. The saturated soil column compartment of AQUASIM can be used to describe advective-dispersive transport of dissolved substances in a saturated soil column, exchange processes with immobile regions consisting of serially connected mixed zones, and transformations of dissolved and sorbed substances. Within the soil column, fast or slow sorption processes using any linear or nonlinear sorption isotherm are possible.

Sorption for a compound i is described as a dynamic process with a process rate of

$$k_i (S_{eq,i}(c_i) - S_i) \quad (7.6)$$

and with stoichiometric coefficients of

$$c_i : -\rho_{solid} \frac{1 - n_e}{n_{e,z0}} \quad (7.7)$$

for the dissolved concentration c_i , and

$$S_i : 1 \quad (7.8)$$

for the sorbed concentration, S_i . In the above equations, ρ_{solid} is the density of the solid material in the soil column, $S_{eq,i}(c_i)$ is the equilibrium sorption isotherm. The rate expression describes the relaxation of the actually sorbed concentration to the equilibrium concentration with a rate constant k_i . If k_i is set to a sufficiently large value, this model is a good approximation to equilibrium sorption. (*For more details on AQUASIM, please refer to Reichert, 1998*). I have used 1525kg/m³ as the bulk density in my computations.

It is found from the simulations, that a linear sorption of the advancing and receding fronts, but with different retardation factors together with an identical increase of dispersion coefficient leads to much better fits of the observed breakthrough curves. The linear sorption isotherm model used in the study is of the following form:

$$c_{s,i} = K_{d,i} c_i \quad (7.9)$$

where $c_{s,i}$ – sorbed concentration of solute i [mg/kg]

$K_{d,i}$ – distribution coefficient for solute i [m³/kg], and

c_i – concentration of solute i [mg/m³].

The distribution coefficient for the advancing front and the receding front is found to be $2.79 \times 10^{-5} \text{ m}^3/\text{kg}$ and $8.51 \times 10^{-6} \text{ m}^3/\text{kg}$, respectively. As mentioned above, for a good fit of the predicted curves to the observed ones, an additional dispersion coefficient of $0.002 \text{ m}^2/\text{h}$ is added to the original dispersion coefficients. The retardation factor calculated for the advancing front from the the fitted sorption model is 1.07, and that for the receding front is 1.02. Since a value of 10000 [1/h] is used for the relaxation constants for sorption of both fronts, the sorption in both cases may be assumed to be a case of equilibrium sorption.

The breakthrough curves predicted using the AQUASIM model are shown in Fig 7.3. The probes used in Fig 7.3 are the same as those in Fig 7.2. As may be noticed, the concentration peaks and the spread of the observed breakthrough curves are better fitted with the new prediction.

The various moments are calculated for the prediction considering sorption to check for its performance. The cross-sectional average of the moments and their relative difference to the observed data are also given in Table 7.1. The relative difference in the zeroth moments remain around 9% on an average with a standard deviation of 5%. The development of the total product mass using the method considering sorption is also given in Fig 7.1. The total product mass do not show any clear pattern of overprediction with distance as that in the case without sorption. The first moments are estimated very accurately with the relative difference just being $2 \pm 2\%$ and the spread of the curves were predicted with an average accuracy of 20% compared to 50% in the case without considering sorption. The accuracy of the predicted breakthrough curves considering sorption implies that pore-scale dispersion coefficient could be applied to mixing-controlled reactive transport, provided all the relevant kinetics are accurately quantified.

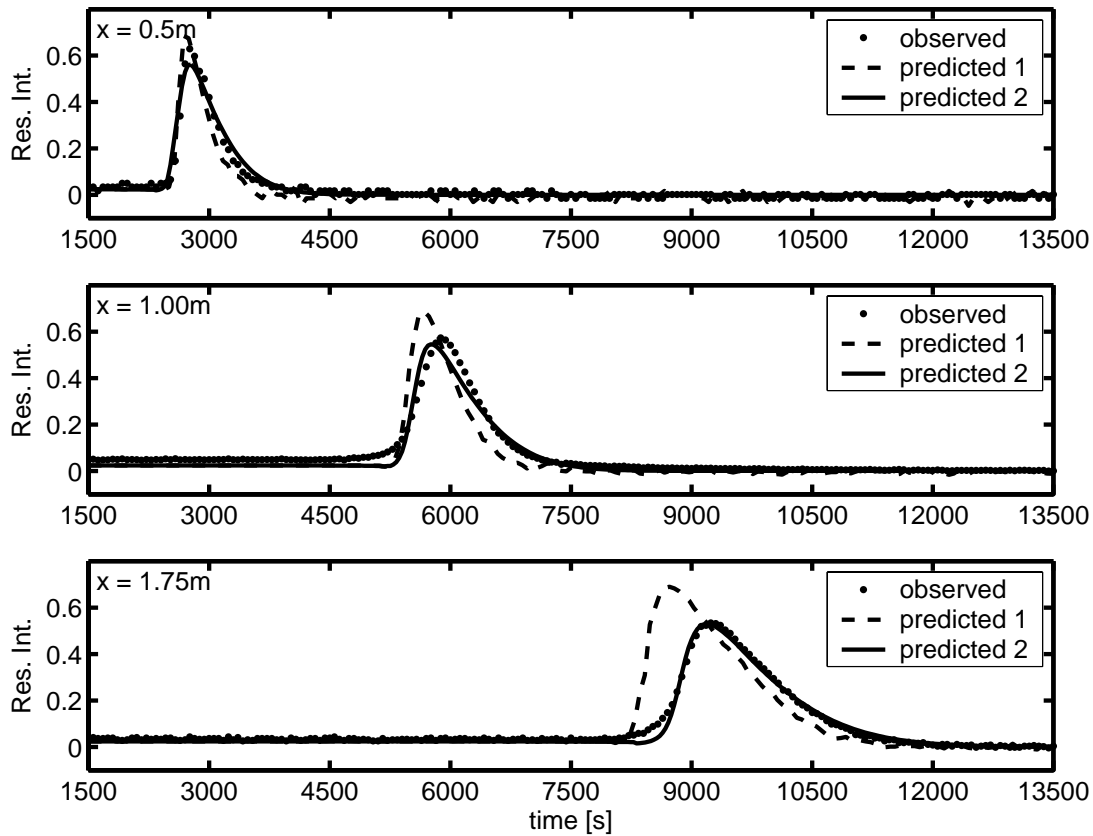


Fig 7.3 Resultant fluorescence intensity of the observed and the various predicted reactive breakthrough curves for three different measurement locations in the column. ‘predicted 1’ corresponds to the prediction without considering tracer sorption and ‘predicted 2’ corresponds to that considering linear tracer sorption.

Raje and Kapoor (2000) and Gramling et al., (2002) performed reactive mixing tests that may be comparable to the present study. The results from their studies indicate lack of pore-scale mixing in a column of 18cm (*Raje and Kapoor, 2000*) and a two-dimensional set-up of 36cm length (*Gramling et al., 2002*). In Table 7.2, a comparison of the characteristic times for the pore and column scales of their works to mine is provided. It has been explained earlier that the decisive factor for the application of typical pore scale dispersion coefficients to mixing-controlled reactive transport is the time-scale of pore-scale transverse dispersion to the time-scale of advective transport from the injection point to the point of observation. This quantity is denoted in this study as the mixed-scale Peclet number (Refer chapter 2, section 2.2 for discussion on characteristic time scales and the various Peclet numbers). A mixed-scale Peclet number greater than one denotes that the pore-scale dispersion coefficients cannot be used for estimating mixing-controlled reactive transport, and vice versa. From Table 7.2, it may be noticed that mixed-scale Peclet numbers in *Gramling et al., (2002)* are larger than one, but that in *Raje and Kapoor (2000)* is smaller than one. Still the results from *Raje and*

Kapoor (2000) cannot be used in mixing-controlled reactive transport applications because the measured breakthrough curve is at the outlet of the column, where the volume averaged concentration is measured. It is known that the dispersion coefficient calculated from the volume averaged concentration corresponds to macrodispersion, and in order to use this value for mixing-controlled transport, $time=2\times\tau_{Dt}$ has to be elapsed. However, this criterion is not met in the experiments of *Raje and Kapoor (2000)*. Therefore, incomplete mixing is observed in their experiments. But in my experiment, the concentrations are measured at time intervals considerably larger than the grain-scale diffusive time.

Comparing the predicted reactive mixing results with and without considering sorption, it becomes clear that even weak sorption is important for mixing at large travel distances. This experimental finding of the study is in full agreement with theoretical studies indicating that sorption differences, no matter how weak, become dominating in the large-time mixing of solutes (*Oya and Valocchi, 1998*). Nonetheless, the observed reactive breakthroughs could be accurately predicted by incorporating a linear sorption model in the prediction method. Since the retardation factor of the advancing alkaline front is found to be larger than the receding acidic front with tracer, no reactive breakthroughs are expected at large travel distances in the sandbox, if identical conditions are followed.

Table 7.2 Characteristic times for the pore and column scales in this study compared to other published works.

	My experiment	<i>Raje and Kapoor, (2000)</i>	<i>Gramling et al., (2002)</i>
Mean grain diameter, d_{50} (m)	1.5×10^{-3}	1.5×10^{-3}	1.3×10^{-3}
Length of the experimental setup, L (m)	2	0.18	0.36
Velocity ¹ , v (m/s)	1.75×10^{-4}	7×10^{-4}	1.21×10^{-4}
Molecular diffusion coefficient ² , D (m ² /s)	10^{-9}	10^{-9}	10^{-9}
Hydrodynamic dispersion coefficient, D^* (m ² /s)	5×10^{-7}	2.3×10^{-6}	1.75×10^{-7}
Grain-scale advective time, $\tau_{a,g} = d_{50}/v$ (s)	8.57	2.15	10.74
Grain-scale diffusive time, $\tau_{d,g} = d_{50}^2/D$ (s)	2250	2250	1690
Column-scale advective time, $\tau_{a,c} = L/v$ (s)	11429	257.14	2975
Column-scale dispersive time, $\tau_{a,c} = L^2/D^*$ (s)	8×10^6	1.4×10^4	7.4×10^5
Grain Peclet number $\tau_{d,g}/\tau_{a,g}$	262	1050	157
Mixed-scale Peclet number $\tau_{d,g}/\tau_{a,c}$	0.20	8.75	0.57
Column-scale Peclet number $\tau_{d,c}/\tau_{a,c}$	700	55	25

¹ only velocities that are comparable to my experiments are considered

² assumed

7.3 Reactive Tracer Test in the Heterogeneously-packed Sandbox

For the reactive tracer test in the heterogeneously packed sandbox, an alkaline surfactant solution with pH 10 is injected into the porous medium originally saturated with an acidic surfactant solution with fluorescein. The pH of the acidic surfactant solution used in the sandbox is 3 unlike that in the column. This is because of the better pH stability of the pH 3 surfactant solution compared to the pH 4 solution. The reactive tracer test in the sandbox durated approximately two weeks.

The experiment was carried out under constant flux conditions with a specific discharge rate of 2.58×10^{-5} m/s. The discharge measurements are taken at regular intervals and its relative standard deviation from the mean value is just 2%. It takes about 13 days to pass 1900 liters (one pore volume is 360liters) of alkaline solution through the porous. Once the alkaline solution is injected into the porous medium, fluorescence intensity measurements are taken at every minute and the values are averaged over ten measurements. Like the reactive test in the column, the purpose of this test is also to provide a standard for the comparison of the reactive mixing predicted from the conservative test.

The conservative tracer test was conducted just after the reactive test due to the reasons mentioned in 7.2. The specific discharge and other relevant information regarding the setup in the conservative test are almost identical to those in the reactive tracer test except that only 900liters of conservative tracer solution was passed through the sandbox. This is because, after passing the said amount of test solution, one of the fluorometers stopped functioning. This does not significantly affect the analysis of the experiment because complete breakthroughs have been observed in all measurement sections except at the outlet. The whole reactive tracer test is not repeated because of the significant sorption observed in the system, which is described in the succeeding paragraphs.

The fluorescence intensity breakthrough curves obtained at the various measurement locations in the sandbox during the reactive tracer test are normalized based on the maximum and minimum fluorescence intensities obtained for the respective locations during the conservative tracer test. The fluorescence intensities measured during the conservative tracer test are also normalized. The observed reactive breakthroughs are then predicted, without considering sorption, following the methodology mentioned in section 7.1.

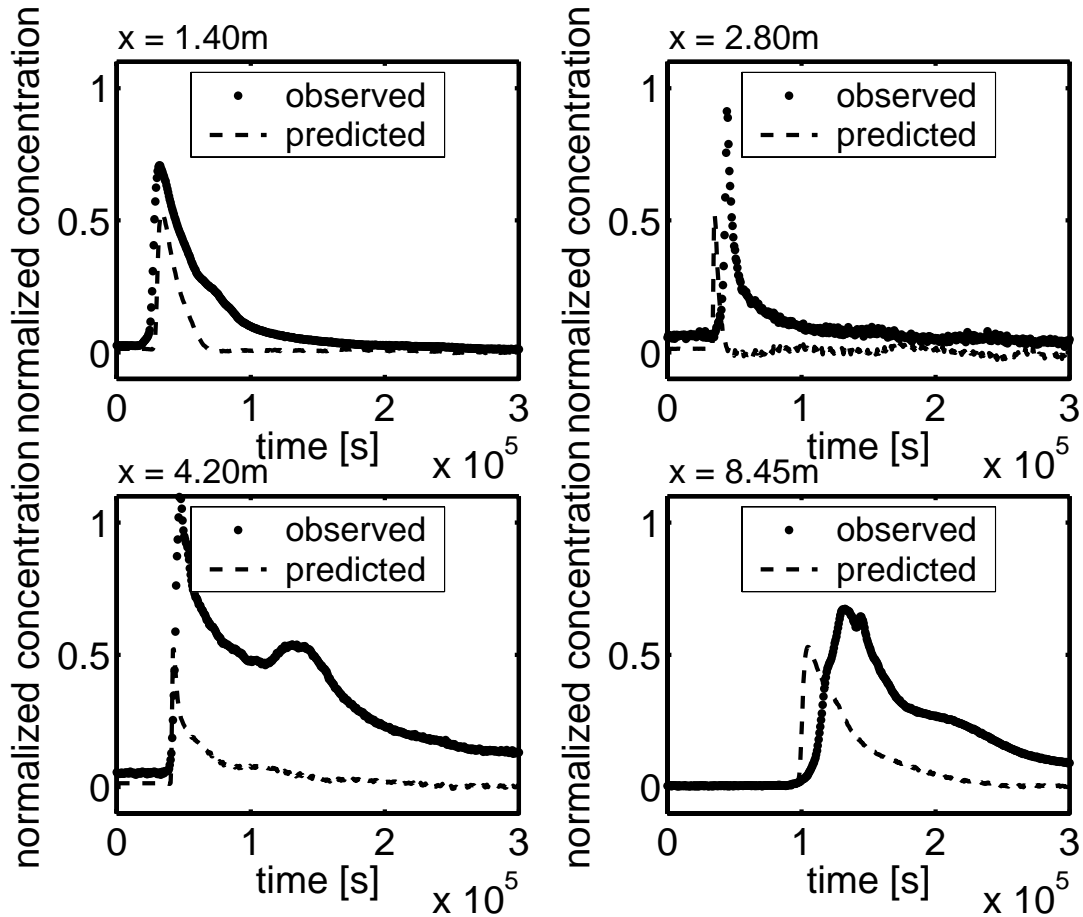


Fig 7.4 Observed and predicted reactive breakthrough curves at different measurement lengths in the sandbox.

The predicted reactive breakthrough curves for a few selected probes are plotted together with the observed breakthroughs at distances of 1.4m, 2.8m, 4.2m, and at 8.95m in Fig 7.4. Throughout the sandbox the observed breakthrough curves have either higher or comparable concentration peaks, and show larger spread. Since the normalized concentration peaks are larger than 0.68, which is the maximum possible concentration for a case with no sorption or kinetics, sorption of the fronts obviously occurs. A definite pattern in the difference between the observed and the predicted breakthroughs is difficult to conclude due to the complexity of the sediment structure and may also be affected by the unknown sorption kinetics involved in the reactive test. In general, the different plots in Fig 7.4 form a good representation for the type of breakthroughs obtained in the sandbox. Most of the measurement locations yielded breakthrough curves as given in the top-right and bottom-right plots in Fig 7.4, where the observed concentration peaks are higher and arrive later than the predicted ones.

If the results from the column tests would have been applicable for the sandbox studies, no breakthroughs would have been observed in the sandbox after travelling a few meters. This is because the injected front had a higher retardation than the displaced front. But here, the results are obviously different from that in the column test. They indicate significant sorption of the tracer to the sand grains.

I have tried to predict some of the observed reactive breakthrough curves using AQUASIM. In the simulations I assume that enhanced sorption of the tracer to silica sand occurs at acidic pH, and its subsequent desorption at alkaline pH. I have considered a linear sorption isotherm for the advancing front (acidic tracer solution) similar to eq.(7.9), and a modified form of the same equation for the receding front, considering the concentration of the advancing front, as follows

$$c_{s,B} = \frac{K_{d,B} \times c_B}{1 + fac \times c_A} \quad (7.10)$$

where A corresponds to the advancing front, and B corresponds to the receding front. The term fac is a coefficient to adjust for the concentration peaks of the observed breakthrough curves.

Basically, five parameters are used, two for the advancing front and three for the receding front, to predict the observed reactive breakthrough curves. A universal set of parameter values is not possible to obtain for the given setup within the prescribed time frame, due to the complexities of the flow field and the different sorption capacities of the different sand types. Nonetheless, I could individually fit the breakthrough curves by adjusting the above mentioned five parameters.

Some of the reactive breakthrough curves predicted considering sorption, are given in Fig 7.5. Out of the three breakthrough curves shown in Fig 7.5, two belong to adjacent measurement locations at identical distance from the inlet. The values of the fitted parameters for the three breakthrough curves are given in Table 7.3.

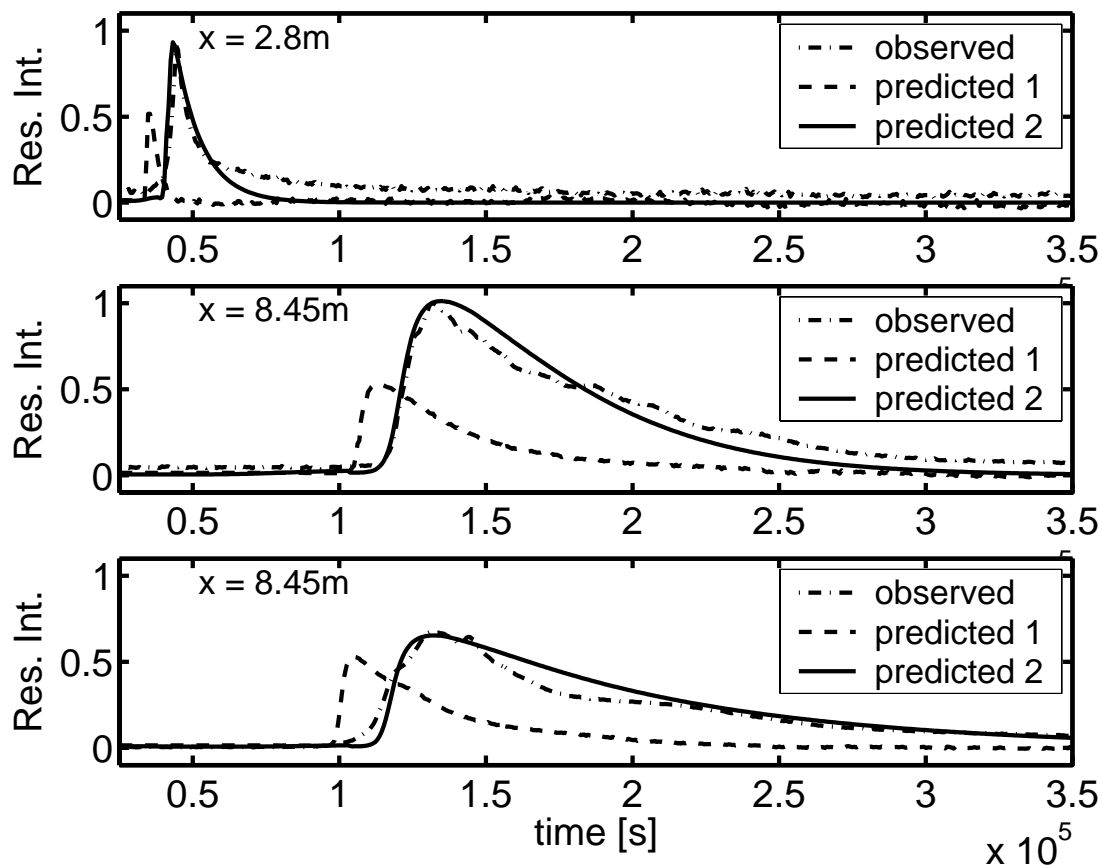


Fig 7.5 Resultant fluorescence intensity of the observed and the various predicted reactive breakthrough curves for three different measurement locations in the sandbox. ‘predicted 1’ corresponds to prediction without considering sorption, and ‘predicted 2’ corresponds to prediction using AQUASIM considering sorption.

Table 7.3 Values of fitted parameters for some reactive breakthroughs predicted using AQUASIM, considering sorption

Distance from inlet [m]	Fitted Parameters				
	Advancing front		Receding front		
	$K_{d,A}$ [m ³ /kg]	k_A [1/h]	$K_{d,B}$ [m ³ /kg]	k_B [1/h]	fac [-]
2.8	7×10^{-5}	10000	5×10^{-4}	0.400	1.0
8.45	3×10^{-5}	10000	1×10^{-3}	0.400	0.6
8.45	2.5×10^{-5}	10000	1×10^{-3}	0.045	0.3

As mentioned before, the values of the fitted parameters should not be considered as a range for the universal set of parameters. Nonetheless, some conclusions may be drawn from the values fitted for the three curves. For the advancing front, the sorption may be considered in equilibrium due to the very high values of the respective relaxation rate constant. Also the distribution coefficients for the advancing front are in the same range, implying that the advancing front may follow a definite pattern of retardation. But no uniformity in the values fitted for receding front can be drawn, which indicates that sorption of the tracer at acidic pH is the major issue in the reactive test in the sandbox. The complexities involved in the sorption of the tracer may be understood from the very different values obtained for the fitting parameters of the receding front, even for adjacent probes lying at same distance from the inlet.

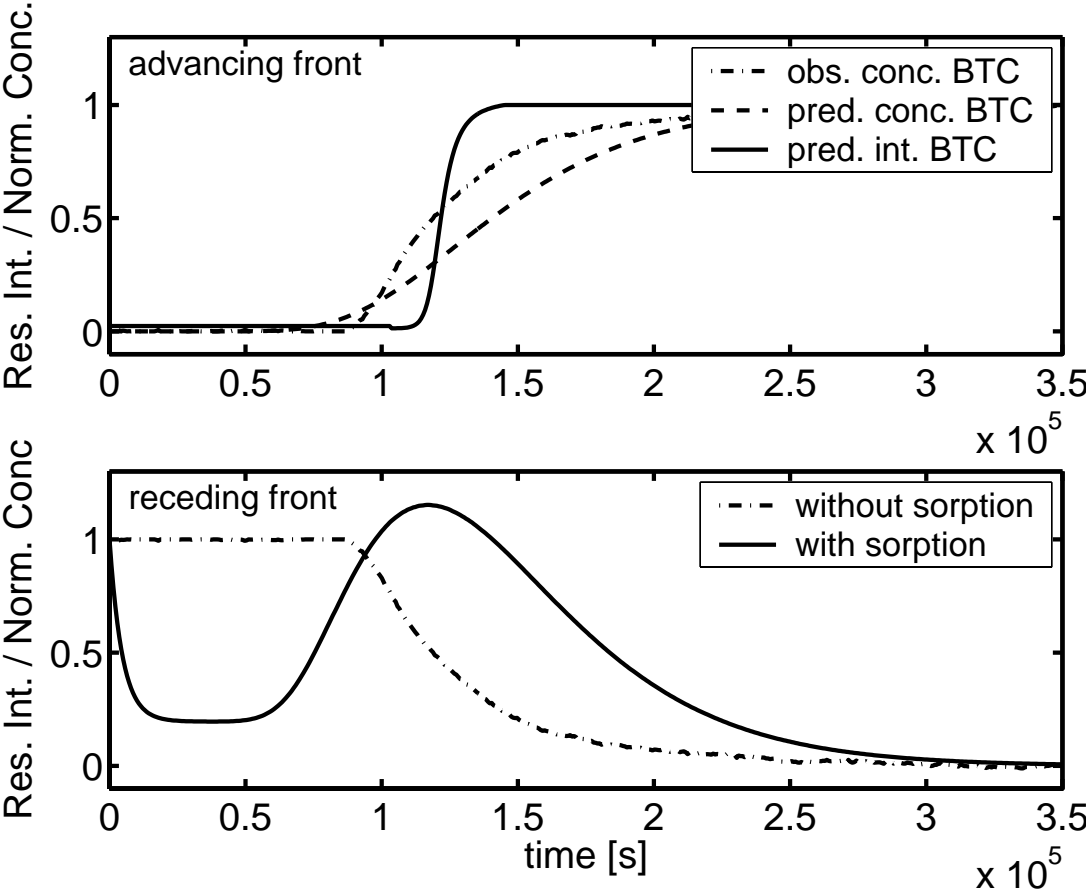


Fig 7.6 Changes that occur to the originally considered advancing and receding front as a consequence of using the sorption parameters mentioned in this study. The measurement location is at 8.45m (same as the centre plot in Fig 7.5).

The changes that happen to the advancing and receding fronts due to considering a sorption model as mentioned here is graphically represented in Fig 7.6. The retardation of the concentration breakthrough curve of the advancing front, when sorption is considered, is

given in the figure. The relative fluorescence intensity predicted from the retarded advancing front is represented by a solid line. In the second plot (bottom) of the same figure, the changes that happen to the receding front breakthrough curve, due to the selected sorption parameters are shown. Since the receding front concentration is modelled as a function of the advancing front, the concentration rises suddenly in response to the increasing pH from the incoming solution. Very low concentration values for the receding front at early times indicate strong sorption of the tracer at low pH values. The product of the line curves from the two plots (top and bottom) in Fig 7.6 yields the corresponding reactive breakthrough curve predicted for that measurement location.

It may be concluded from the above discussions that tracer sorbs heavily and in a complicated fashion to various sand types under acidic pH. It is difficult, if not impossible, to accurately quantify the processes behind the observed behaviour due to unknown chemical properties of the nonionic surfactant used in the study. The properties of the surfactants are not disclosed by its manufacturer, *BASF AG, Ludwigshafen*. Although a few studies have been conducted with regard to nonionic surfactant sorption and surface hydrophobicity (*Kiraly et al., 1997; Grant et al., 1998; Grant et al., 2000; Penfold et al., 2002*), no studies have been published specifically on the influence of the medium pH on the sorption mechanisms of alkylpolyglucosides.

Since dominant sorption is found in the reactive sandbox experiment, the efficiency of point measurements in giving reliable information on dilution and mixing cannot be drawn conclusively. Nonetheless, the complexities that may arise in real situations is clearly pictured in this experiment.

7.4 Concluding Remarks

The reactive mixing predicted without considering sorption in the homogeneous case showed a clear trend of overprediction of the total product mass with distance. But when reactive mixing was predicted considering linear sorption of both fronts, the predicted reactive breakthrough curves agreed well with the observed breakthrough curves. The estimated retardation factors for the advancing and receding fronts are 1.07 and 1.02, respectively. The accuracy of the predicted breakthrough curves considering sorption concludes that point-like measurements provide reliable information of dilution and mixing, and therefore are effective enough in predicting product formation provided sorption parameters are effectively quantified.

The observed reactive breakthrough curves in the sandbox have either higher or comparable concentration peaks, and larger spread than the reactive breakthrough curves predicted without considering sorption. The observed breakthrough curves are fitted using a linear sorption model for the advancing front and a modified version of linear sorption for the receding front. Nonetheless, no universal set of sorption parameters are attained as expected due to the complex nature of sorption that may arise in a heterogeneously packed system. It is difficult, if not impossible, to accurately quantify the processes behind the observed behaviour due to the unknown chemical properties of the nonionic surfactant used in the study.

From the prediction of the reactive mixing tests in both the homogeneous and heterogeneous porous media, it becomes clear that even weak sorption is important for mixing at large travel distances. This experimental finding of the study is in full agreement with theoretical studies indicating that sorption differences, no matter how weak, become dominating in the large-time mixing of solutes (*Oya and Valocchi, 1998*). The results bring into light the probable difficulties that may be encountered in real case situations regarding prediction of reactive transport. Therefore, more research needs to be done in order to systematically quantify all the dominating processes involved in various types of reactive mixing processes in field situations.

8 FINAL REMARKS

8.1 Summary and Conclusions

As mentioned in *chapter 1*, the objective of my thesis is to provide answers for the following questions:

1. Do point-like measurements of concentrations provide reliable information of dilution and mixing as suggested by *Cirpka and Kitanidis (2000a, b)*?
2. Are (semi)-analytical results for effective dispersion and mixing from stochastic theory (*Dentz et al., 2000a; Fiori and Dagan, 2000*) applicable to real data?

The major tasks involved in achieving the objectives have been:

- Development of a point measurement system,
- Selection of suitable conservative and reactive tracers,
- Conducting experiments in a homogeneously packed column,
- Conducting experiments in a heterogeneously packed sand-box,
- Interpretation of the results in accordance with the objectives.

Fiber optic fluorometry is used as the point measurement system. The major modification done to the available fiber optic fluorometry has been the reduction of the measurement tip diameter of the original fiber optic probes from 4.4mm to 2.5mm using heat shrinkable tubes. This modification has been done to measure fluorescence intensity measurements within small measurement volumes.

I used fluorescein, which is reported as a good conservative tracer for silica sands (*Smart and Laidlaw, 1977; Kasnavia et al., 1999*), as both the conservative and the reactive tracer. The fluorescence intensity of fluorescein is maximum at alkaline pHs and minimum at acidic pHs. This property of fluorescein has been exploited in using it as the reactive tracer. Although fluorescein has been used as a reactive tracer in open channel flow experiments (*Koochesfahani and Dimotakis, 1986*), the current study is the first in which it is used as a reactive tracer in porous media.

In order to prevent the sorption of fluorescein to silica grains at low pH (*Kasnavia et al., 1999; Sabatini, 2000; Sabatini and Austin, 1991; Smart and Laidlaw, 1977*), LUTENSOL GD 70, a nonionic surfactant is added to the test solutions. In order to allow comparison between conservative and reactive tracer tests, the surfactant was added to both test solutions in equal concentration.

In a conservative tracer test, an alkaline surfactant solution with tracer displaces an alkaline surfactant solution without tracer from the porous media, while in a reactive tracer test, an alkaline surfactant solution without tracer displaces an acidic surfactant solution with tracer from the porous media. In order to prevent bacterial growth in the porous media feeding on the surfactants, 0.1mmol of sodium azide (NaN_3) was added to the alkaline surfactant solution passed into the porous media.

Before conducting experiments in the two-dimensional heterogeneous porous medium, experiments are conducted in the one-dimensional homogeneous soil column to test the efficiency of the selected point measurement system and the tracer.

The soil column is 2m long, has an inner diameter of 10cm, and is filled with coarse sand (grain size: 1-2.5mm). The sandbox has dimensions of 14m×0.5m×0.13m and is filled heterogeneously with four types of sand with grain sizes ranging between 0-3mm, and hydraulic conductivity between 5.61×10^{-4} - 1.67×10^{-2} m/s (*Rahman, in preparation*). The heterogeneous packing in the sandbox resembles natural sedimentation patterns unlike the well defined heterogeneous blocks usually seen in the comparable experiments. A conservative and a reactive tracer test each, both under constant flux conditions, were conducted in both systems. To the best of my knowledge, this is the first time that reactive mixing tests are carried out on such a scale and with sand as the porous medium. The published reactive tests have lengths less than 40cm, and used glass beads instead of sand grains (*Raje and Kapoor, 2000; Gramling et al., 2002*).

From the conservative tracer test data, the dilution and mixing of the tracer is characterized. The dilution coefficients calculated from the conservative tracer tests are used to predict mixing-controlled reactive transport in the same porous media. The reactive mixing predicted from conservative tests are then compared with actual reactive mixing data obtained from the reactive tests. The analytical solutions from linear stochastic theory are compared with the conservative test data obtained in the heterogeneous domain to check their applicability.

As expected, macrodispersion and effective dispersion coefficients calculated from the conservative tracer test in the homogeneous porous medium have values in the same range. Apparent local dispersivities in the column experiment range between 2mm and 13mm, and apparent effective dispersivities are in the range of 3mm, which is in the range of the maximum grain size. The tests in the column confirmed the efficiency of the point measurement technique and the selected tracer, fluorescein.

The results from the conservative tests in the heterogeneous medium showed qualitative agreement with the numerical studies by *Cirpka and Kitanidis (2000a)*. A strong increase of macrodispersion coefficients, well known from previous studies, is observed in the conservative test in the heterogeneous porous medium. The difference between macrodispersion coefficient D^* and effective dispersion coefficient D^e , is only a factor of about 1.5, which is not that pronounced when compared to some theoretical studies (*Kitanidis, 1994; Dentz et al., 2000a*). This is because of the thin vertical extension of the sediment lenses in the sandbox. Since transverse pore-scale dispersion is the process that makes effective dispersion catch up with macrodispersion, effective dispersion reaches macrodispersion values faster for smaller transverse diffusion lengths. The heterogeneities in the sandbox mimic rather typical sedimentary patterns. For lenses of comparable thickness, it can thus be concluded that incomplete dispersive mixing is significant but by far not as pronounced as predicted for virtual aquifers with isotropic heterogeneities. This is important for the scale-up of mixing-controlled reactive transport (*Cirpka, 2002*).

The local dispersion coefficients determined at single probes in the sandbox range between 5.5mm and 860mm. It is observed that regions with large contrast in hydraulic conductivity gave opportunity to enhanced mixing.

A modified version of the first-order solution for effective dispersion and mixing from linear stochastic theory (*Dentz et al., 2000a; Fiori and Dagan, 2000*) was fitted to the conservative experimental data from the sandbox by substituting relevant coefficients. Although the fit itself is not perfect due to lacking ergodicity, it leads to reasonable values. In particular, the fitted transverse pore-scale dispersivity of 0.23mm, which is one of the fitted parameters, is in the range of values reported for the types of sands used in the study (*Cirpka et al., 2004*). *Based on the above observations, it may be concluded that linear stochastic theory is applicable to real data.* The conservative test data from the sandbox are used to infer the hydraulic conductivity field of the experimental domain by geostatistical inverse modeling (*Nowak, 2004*).

The dilution coefficients calculated at different measurement locations in the conservative tracer tests in both setups were used to predict reactive mixing at the same locations in the respective domains. The predicted reactive breakthrough curves are compared with the observed reactive breakthrough curves.

The reactive mixing predicted without considering sorption in the homogeneous case shows a clear trend of overprediction of the total product mass with distance. But when

reactive mixing is predicted considering linear sorption of both fronts, the predicted reactive breakthrough curves agree well with the observed breakthrough curves. The estimated retardation factors for the advancing and receding fronts are 1.07 and 1.02, respectively. The accuracy of the predicted breakthrough curves considering sorption concludes that *point-like measurements provide reliable information of dilution and mixing, and therefore are effective enough in predicting product formation provided sorption parameters are effectively quantified.*

The observed reactive breakthrough curves in the sandbox have either higher or comparable concentration peaks, and larger spread than the predicted reactive breakthrough curves. This implies sorption of both fronts, advancing and the receding, in the sandbox reactive test. A definite pattern or trend in the difference between the observed and the predicted breakthroughs are difficult to notice due to the complexity of the sedimentation pattern, and also due to the unknown sorption kinetics involved in the reactive tracer test. Probable reasons for the observed behaviour could be an enhanced sorption of tracer molecules to sand grains at pH 3, which had not been the case for the test in the column. It is difficult, if not impossible, to accurately quantify the processes behind the observed behaviour due to unknown chemical properties of the nonionic surfactant used in the study.

Nonetheless, I simulated the observed reactive breakthrough curves in the sandbox by considering sorption. Although, an universal set of sorption parameters could not be drawn due to the complex nature of the sorption in the heterogeneous domain, the observed curves could be individually fitted. It has been found from the results that the largest uncertainty in predicting mixing, even when sorption is considered, lies with the receding front in a reactive test, which is the tracer in acidic surfactant solution. The experiment clearly gives an idea on the magnitude of complex problems that need to be solved in real case situations.

8.2 Future Prospects

From the prediction of reactive mixing tests in both the homogeneous and heterogeneous porous media, it becomes clear that even weak sorption is important for mixing at large travel distances. This experimental finding of the study is in full agreement with theoretical studies indicating that sorption differences, no matter how weak, become dominating in the large-time mixing of solutes (*Oya and Valocchi, 1998*). The results bring into light the probable difficulties that may be encountered in real case situations regarding prediction of reactive transport. Therefore, more research needs to be done in order to systematically quantify all the

dominating processes involved in various types of reactive mixing processes in field situations.

Also the existing experimental setups and methods may be improved upon to complete elimination of tracer sorption, thereby contributing additional information to the results mentioned in this study. As mentioned in previous chapters, only a few theoretical and numerical studies related to mixing and reaction have been verified experimentally, or their applicability to real data have been checked. So there is a huge potential for experimentalists to explore those theoretical developments so that improvements to the existing concepts or new concepts may be developed. A systematic approach in handling these issues may lead to the development of improved remediation strategies.

REFERENCES

- Andricevic, R., and V. Cvetkovic, Relative dispersion for solute flux in aquifers, *J Fluid Mech.*, 361, 145-174, 1998.
- Attinger, S., M. Dentz, H. Kinzelbach, and W. Kinzelbach, Temporal behaviour of a solute cloud in a chemically heterogeneous porous medium, *J. Fluid Mech.* 386, 77-104, 1999.
- Bajracharya, K., and D.A. Barry, Nonequilibrium solute transport parameters and their physical significance: numerical and experimental results, *J. Contam. Hydrol.*, 24, 185-204, 1997.
- Barth, G.R., T. H. Illangasekare, M.C. Hill, and H. Rajaram, A new tracer density criterion for heterogeneous porous media, *Water Resour. Res.*, 37(1), 21-31, 2001.
- Barth, G.R., T.H. Illangasekare, and H. Rajaram, The effect of entrapped nonaqueous phase liquids on tracer transport in heterogeneous porous media: laboratory experiments at the intermediate scale, *J. Contam. Hydrol.*, 67, 247-268, 2003.
- Bear, J., *Dynamics of fluids in porous media*, New York: American Elsevier Publishing Company, pp.764, 1972.
- Bear, J., *Hydrodynamic dispersion in flow through porous media*, De Wiest RJM (ed) Academic Press, New York, 109-200, 1969.
- Bear, J., Some experiments in dispersion, *J Geophys. Res.*, 66, 2455-2467, 1961.
- Behrens, H., Quantitative Bestimmung von Uranin, Eosin und Pyranin in Gemischen mittels Fluoreszenzmessung bei definierten pH-Werten, *Steir. Beitr. z. Hydrogeologie*, 39, 117-129, Graz, 1988.
- Blackwell, R.J., Laboratory studies of microscopic dispersion phenomena, *J Petrol. Technol.*, Society of Petrol. Eng., March 1962, 1-8, 1962.
- Brinck, J., B. Jönsson, and F. Tiberg, Kinetics of non-ionic surfactant adsorption and desorption at the silica-water interface: One component, *Langmuir*, 14, 1058-1071, 1998.
- Bruch, J.C., and R.L. Street, Two-dimensional dispersion, *J. Sanit. Eng. Div., Amer. Soc. Civil Eng.*, SA6, 17-39, 1967.
- Bruch, J.C., Two-dimensional dispersion experiments in a porous medium, *Water Resour. Res.*, 6(3), 791-800, 1970.

- Chao, H., H. Rajaram, and T. Illangasekare, Intermediate-scale experiments and numerical simulations of transport under radial flow in a two-dimensional heterogeneous porous medium, *Water Resour. Res.*, 36(10), 2869-2884, 2000.
- Cirpka, O.A., Å. Olsson, Q. Ju, M.A. Rahman, and P. Grathwohl, Length of reactive plumes controlled by transverse dispersion, *Environ. Sci. Technol.*, (submitted, 2004).
- Cirpka, O.A., and P.K. Kitanidis, An advective-dispersive stream tube approach for the transfer of conservative-tracer data to reactive transport, *Water Resour. Res.*, 36(5), 1209-1220, 2000b.
- Cirpka, O.A., and P.K. Kitanidis, Characterization of mixing and dilution in heterogeneous aquifers by means of local temporal moments, *Water Resour. Res.*, 36(5), 1221-1236, 2000a.
- Cirpka, O.A., and P.K. Kitanidis, Theoretical basis for the measurement of local transverse dispersion in isotropic porous media, *Water Resour. Res.*, 37(2), 243-252, 2001a.
- Cirpka, O.A., C. Windfuhr, G. Bisch, S. Granzow, H. Scholz-Muramatsu, and H. Kobus, Microbial reductive dechlorination in large-scale sandbox models, *J. Environ. Eng.*, 125(9), 861-870, 1999b.
- Cirpka, O.A., Choice of dispersion coefficients in reactive transport calculations on smoothed fields, *Journal of Contaminant Hydrology*, 58, 261-282, 2002.
- Cirpka, O.A., Dilution and mixing of solutes in soils and aquifers, Habilitation thesis, Faculty of Civil and Environmental engineering, University of Stuttgart, 2001b.
- Corapcioglu, M.Y., and P. Fedirchuk, Glass bead micromodel study of solute transport, *J. Contam. Hydrol.*, 36, 209-230, 1999.
- Dagan, G., Solute transport in heterogeneous porous formations, *J. Fluid Mechanics*, 145, 151-177, 1984.
- Dagan, G., Theory of solute transport by groundwater, *Ann. Rev. Fluid Mech.*, 19, 183-215, 1987.
- Dagan, G., Time-dependent macrodispersion for solute transport in anisotropic heterogeneous aquifers, *Water Resour. Res.*, 24(9), 1491-1500, 1988.
- Danzer, J., Surfactant transport and coupled transport of polycyclic aromatic hydrocarbons (PAHs) in natural aquifer material – laboratory experiments, *Tübinger Geowissenschaftliche Arbeiten*, University of Tübingen, 1999.

- Darcy, H., *Les fontaines publiques de la ville de Dijon*, Paris: Victor Dalmond, 1856.
- Delay, F., G. Porel, and G. de Marsily, Predicting solute transport in heterogeneous media from results obtained in homogeneous ones: an experimental approach, *J. Contam. Hydrol.*, 25, 63-84, 1997.
- Dentz, M., H. Kinzelbach, S. Attinger, and W. Kinzelbach, Temporal behavior of a solute cloud in a heterogeneous porous medium I: Point-like injection, *Water Resour. Res.*, 36, 3605-3624, 2000a.
- Dentz, M., H. Kinzelbach, S. Attinger, and W. Kinzelbach, Temporal behavior of a solute cloud in a heterogeneous porous medium II: Spatially extended injection, *Water Resour. Res.*, 36, 3591-3604, 2000b.
- Dybbs, A., and R.W. Edwards, A new look at porous media fluid mechanics – Darcy to turbulent, in *Laser Anemometry in Fluid Mechanics*, vol.2, Selected papers from the international symposium on applications of laser anemometry to fluid mechanics, 201-256, 1985.
- Fetter, C.W., *Contaminant hydrogeology*, Prentice-Hall, Inc., 1999.
- Fiori, A., and G. Dagan, Concentration fluctuations in aquifer transport: a rigorous first-order solution and applications, *J. Contam. Hydrol.*, 45(1-2), 139-163, 2000.
- Fiori, A., Finite Peclet extensions of Dagan's solutions to transport in anisotropic heterogeneous formations, *Water Resour. Res.*, 32(1), 193-198, 1996.
- Freeze, R.A., A stochastic conceptual analysis of one-dimensional groundwater flow in a non-uniform homogeneous media, *Water Resour. Res.*, 11(5), 725-741, 1975.
- Gaigalas, A.K., A.C. van Orden, T.H. Mareci, and L.A. Lewis, Application of magnetic resonance imaging to visualization of flow in porous media, *Nucl. Technol.*, 84, 113-118, 1989.
- Gaspar, E., In *Modern Trends in Tracer Hydrology*, *Hydrological Tracers*, 1, 2-43, 1987.
- Gelhar, L.W., and C.L. Axness, Three dimensional stochastic analysis of macrodispersion in aquifers, *Water Resour. Res.*, 19(1), 161-180, 1983.
- Gelhar, L.W., C. Welty, and K.T. Rehfeldt, A critical review of data on field scale dispersion in aquifers, *Water Resour. Res.*, 28, 1955-1974, 1992.
- Gelhar, L.W., *Stochastic Subsurface Hydrology*, Prentice-Hall, Inc., New Jersey, 1993.
- Gheith, H.M., and F.W. Schwartz, Electrical and visual monitoring of small scale three-dimensional experiments, *J. Contam. Hydrol.*, 34, 191-205, 1998.

- Ghodrati, M., Point measurement of solute transport processes in soil using fiber optic sensors, *Soil Sci. Soc. Am. J.*, 63, 471-479, 1999.
- Ginn, T.R., C.S. Simmons, and B.D. Wood, Stochastic-convective transport with nonlinear reaction: Biodegradation with microbial growth, *Water Resour. Res.*, 31(11), 2869-2700, 1995.
- Gramling, C.M., C.F. Harvey, and L.C. Meigs, Reactive transport in porous media: a comparison of model prediction with laboratory visualization, *Env. Sci. Technol.*, 36, 2508-2514, 2002.
- Grant, L.M., F. Tiberg, and W.A. Drucker, Nanometer-scale reorganization of ethylene oxide surfactants on graphite, hydrophilic silica and hydrophobic silica, *Journal of Physical Chemistry*, 102, 4288-4294, 1998.
- Grant, L.M., T. Ederth, and F. Tiberg, Influence of surface hydrophobicity on the layer properties of adsorbed non-ionic surfactants, *Langmuir*, 16, 2285-2291, 2000.
- Grathwohl, P., C. Eberhardt, I. Klenk, and U. Maier, Transverse vertical dispersivity in aquifer materials: implications on mass transfer across the capillary fringe and the length of steady state plumes, *Groundwater Research*, Rotterdam, Rosbjerg et al. (eds) © 2000.
- Greiner, A., W. Schreiber, G. Brix and W. Kinzelbach, Magnetic resonance imaging of paramagnetic tracers in porous media: quantification of flow and transport parameters, *Water Resour. Res.*, 33, 1461-1473, 1997.
- Guilbault, G.G, *Practical Fluorescence*, second edition, Marcel Dekker Inc., New York, pp.63, 1990.
- Guillot, G., G. Kassab, J.P. Hulin, and P. Rigord, Monitoring of tracer dispersion in porous media by NMR imaging, *J. Phys. D Appl. Phys.*, 24, 763-773, 1991.
- Haselow, J.S., and R.A. Greenkorn, An experimental investigation of the effect of idealized heterogeneity on the dispersion of miscible fluids, *Water Resour. Res.*, 27(9), 2473-2482, 1991.
- Hassinger, R.C., and D.U. von Rosenberg, A mathematical and experimental examination of transverse dispersion coefficients, *Society of Petroleum Engineers Journal*, 243, 195-204, 1968.
- Huang, W.E., C.C. Smith, D.N. Lerner, S.F. Thornton, and A. Oram, Physical modelling of solute transport in porous media: evaluation of an imaging technique using UV excited fluorescent dye, *Water Research*, 36, 1843-1853, 2002.

- Huang, W.E., S.E. Oswald, D.N. Lerner, C.C. Smith, and C. Zheng, Dissolved oxygen imaging in a porous medium to investigate biodegradation in a plume with limited electron acceptor supply, *Environ. Sci. Technol.*, 37, 1905-1911, 2003.
- Jafvert, C.T., Surfactants/Cosolvents, Technology Evaluation Report, GWRTAC, 1996.
- Jia, C., K. Shing, and Y.C. Yortsos, Visualization and simulation of non-aqueous phase liquids solubilization in pore networks, *J. Contam. Hydrol.*, 35, 363-387, 1999.
- Kapoor, V., and L.W. Gelhar, Transport in three-dimensionally heterogeneous aquifers:
1. Dynamics of concentration fluctuations, *Water Resour. Res.*, 30(6), 1775-1788, 1994a.
- Kapoor, V., and L.W. Gelhar, Transport in three-dimensionally heterogeneous aquifers:
2. Predictions and observations of concentration fluctuations, *Water Resour. Res.*, 30(6), 1789-1801, 1994b.
- Kapoor, V., and P.K. Kitanidis, Concentration fluctuations and dilution in aquifers, *Water Resour. Res.*, 34(5), 1181-1193, 1998.
- Kapoor, V., and P.K. Kitanidis, Concentration fluctuations and dilution in two-dimensionally periodic heterogeneous porous media, *Transp. in Porous Media*, 22, 91-119, 1996.
- Kapoor, V., L.W. Gelhar and F. Miralles-Wilhem, Bimolecular second-order reactions in spatially varying flows: segregation induced scale-dependent transformation rates, *Water Resour. Res.*, 33(4), 527-536, 1997.
- Kasnavia, T., D. Vu, and D.A. Sabatini, Fluorescent Dye and Media Properties Affecting Sorption and Tracer Selection, *Ground water*, 37(3), 376-381, 1999.
- Kasnavia, T.N., Influence of molecular structure and functional groups on fluorescent dye sorption, M.S. Thesis, Department of Civil Engineering and Environmental Science, University of Oklahoma, 1997.
- Keller, A.A., V.R. Paul, and P.K. Kitanidis, Prediction of single phase transport parameters in a variable aperture fracture, *Geophys. Res. Lett.*, 22, 1425-1428, 1995.
- Kemblowski, M.W., C.M. Chang, and I. Kamil, A mean behavior model of aerobic biodegradation in heterogeneous formation, *Stochastic Hydrol. Hydraul.*, 11, 255-266, 1997.
- Khalili, A., A.J. Basu, and U. Pietrzyk, Flow visualization in porous media via positron emission tomography, *Phys. Fluid*, 10, 1031-1033, 1998.

- Kitanidis, P.K., Prediction by the method of moments of transport in heterogeneous formations, *J. Hydrol.*, 102(1-4), 453-473, 1988.
- Kitanidis, P.K., The concept of the dilution index, *Water Resour. Res.*, 30(7), 2011-2026, 1994.
- Klenk, I.D., and P. Grathwohl, Transverse vertical dispersion in groundwater and the capillary fringe, *J. Contam. Hydrol.*, 58, 111-128, 2002.
- Koochesfahani, M.M., and P.E. Dimotakis, Mixing and chemical reactions in a turbulent liquid mixing layer, *J. Fluid Mech.*, 170, 83-112, 1986.
- Kreft, A, and A. Zuber, On the physical meaning of the dispersion equation and its solutions for different initial and boundary conditions, *Chem. Eng. Sci.*, 33 (11), 1471-1480, 1978.
- Lajeunesse, E., J.Martin, N. Rakotomalala, D. Salin, and Y.C. Yortsos, Miscible displacement in a Hele-Shaw cell at high rates, *J. Fluid Mech.*, 398, 299-319, 1999.
- Levy, M., and B. Berkowitz, Measurement and analysis of non-fickian dispersion in heterogeneous porous media, *J. Contam. Hydrol.*, 64, 203-226, 2003.
- Lichtner, P.C., C.I. Steefel, and E.H. Oelkers, Reactive transport in porous media, *Reviews in Mineralogy*, 34, 1996.
- Liu, S., T.C.J. Yeh, and R. Gardiner, Effectiveness of hydraulic tomography: sandbox experiments, *Water Resour. Res.*, 38(4), 1034-1042, 2002.
- Loveland, J.P., S. Bhattacharjee, J.N. Ryan, and M. Elimelech, Colloid transport in a geochemically heterogeneous porous medium: aquifer tank experiment and modeling, *J. Contam. Hydrol.*, 65, 161-182, 2003.
- Lyczkowski, R.W., Modeling of flow nonuniformities in fissured porous media, *Can. J. Chem. Eng.*, 60, 61-75, 1982.
- MacQuarie, K.T.B., and E.A. Sudicky, Simulation of biodegradable organic contaminants in groundwater, 2, Plume behavior in uniform and random flow fields, *Water Resour. Res.*, 26(2), 223-239, 1990.
- Miralles-Wilhelm, F., L.W. Gelhar, and V. Kapoor, Stochastic analysis of oxygen-limited biodegradation in three-dimensionally heterogeneous aquifers, *Water Resources Research*, 33(6), 1251-1263, 1997.
- Molz, F.J and M.A. Widdowson, Internal inconsistencies in dispersion-dominated models that incorporate chemical and microbial kinetics, *Water Resour. Res.*, 24(4), 615-619, 1988.

- Montemagno, C.D., and W.G. Gray, Photoluminescent volumetric imaging – a technique for the exploration of multiphase flow and transport in porous media, *Geophys. Res. Lett.*, 22, 425-428, 1995.
- Montgomery, J.M., *Water Treatment Principles and Design*, New York: John Wiley and Sons, 1985.
- Murphy, E.M. , T.R. Ginn, A. Chilakapati, C.T. Resch, J.L. Phillips, T.W. Wietsma, and C.M. Spadoni, The influence of physical heterogeneity on microbial degradation and distribution in porous media, *Water Resour. Res.*, 33(5), 1087-1103, 1997.
- Nakashima, Y., and Y. Watanabe, Estimate of transport properties of porous media by microfocus X-ray computed tomography and random walk simulation, *Water Resour. Res.*, 38(12), 1272-1284, 2002.
- Nielsen, M.J., G.F. Pinder, T.J. Kulp and S.M. Angel, Investigation of dispersion in porous media using fiber-optic technology, *Water Resour. Res.*, 27(10), 2743-2749, 1991.
- Nowak, W., Geostatistical methods for the identification of flow and transport parameters in subsurface flow, Doctoral Thesis, Faculty of Civil and Environmental Engineering, University of Stuttgart, Germany, 2004 (submitted).
- Oelkers, E.H., Physical and chemical properties of rocks and fluids for chemical mass transport calculations, *Reviews in Mineralogy (Ed.) Lichtner et al.*, 34, 1996.
- Oliviera, B.I., A.H. Demond, and A. Salehzadeh, Packing of Sands for the Production of Homogeneous Porous Media, *Soil Science of America Journal*, 60, 49-53, 1996.
- Oya, S., and A.J. Vallochi, Transport and biodegradation of solutes in stratified aquifers under enhanced in-situ bioremediation conditions, *Water Resour. Res.*, 34(12), 3323-3334, 1998.
- Pearl, Z., M. Magaritz, and P. Bendel, Measuring diffusion coefficients of solutes in porous media by NMR imaging, *J. Magn. Reson.*, 95, 597-602, 1991.
- Penfold, J., E. Staples, and I. Tucker, On the consequences of surfactant treatment on the adsorption of non-ionic surfactants at the hydrophilic silica-solution interface, *Langmuir*, 18, 2967-2970, 2002.
- Rahman, M.A., Experimental investigations on transverse dispersive mixing in heterogeneous model aquifer, Doctoral Thesis, Faculty of Civil and Environmental Engineering, University of Stuttgart, Germany, 2004 (submitted).

- Rajaram, H., and L.W. Gelhar, Plume-scale dependent dispersion in aquifers with the wide range of scale of heterogeneity, *Water Resour. Res.*, 31(10), 2469-2482, 1995.
- Raje, D.S., and V. Kapoor, Experimental study of bimolecular reaction kinetics in porous media, *Env. Sci. Technol.*, 34, 1234-1239, 2000.
- Rashidi, M., L. Peurrung, A.F.B. Tompson, and T.J. Kulp, Experimental analysis of pore-scale flow and transport in porous media, *Adv. Water Resour.*, 19(3), 163-180, 1996.
- Reichert, P., *Aquasim 2.0 – user manual*, ISBN: 3-906484-16-5, 1998.
- Ripple, C.D., R.V. James, and J. Rubin, Packing-Induced Radial Particle-Size Segregation: Influence on Hydrodynamic Dispersion and Water Transfer Measurements, *Soil Science of America Journal*, 38, 219-222, 1974.
- Ripple, C.D., R.V. James, and J. Rubin, Radial particle-size segregation during packing of particulates into cylindrical containers, *Powder Technology*, 8, 165-175, 1973.
- Robbins, G.A., Methods for determining transverse dispersion coefficients of porous-media in laboratory column experiments, *Water Resour. Res.*, 25, 1249-1258, 1989.
- Rubin, J., Transport of reacting solutes in porous media: Relationship between mathematical nature of problem formulation and chemical nature of reactions, *Water Resour. Res.*, 19(5), 123-1252, 1983.
- Rubin, Y., *Applied Stochastic Hydrogeology*, Oxford Univ. Press, New York, 2003.
- Sabatini, D.A., and T.A. Austin, Characteristics of Rhodamine WT and Fluorescein as Adsorbing Ground-water Tracers, *Groundwater*, 29(3), 341-349, 1991.
- Sabatini, D.A., Sorption and Intraparticle Diffusion of Fluorescent Dyes with Consolidated Aquifer Media, *groundwater*, 38(5), 651-656, 2000.
- Schäfer, G., Einfluss von Schichtenstrukturen und lokalen Einlagerungen auf die Längsdispersion in Porengrundwasserleitern, Dissertation thesis, University of Stuttgart, Germany, 1990.
- Scheidegger, A.E., Statistical hydrodynamics in porous media, *J. Appl. Phys.*, 25(8), 994-1001, 1954.
- Schmid, G and B. Barcewski, Tracer Technologies for Hydrological systems, IAHS Publication No. 229, pp 13-22, 1995.
- Schwartz, C.E., and J.M. Smith, Dynamic studies of dispersion and channeling in fixed beds, *AIChE J.*, 28(5), 751-759, 1982.

- Silliman, S.E., and L. Zheng, Comparison of Observations from a Laboratory Model with Stochastic Theory: Initial Analysis of hydraulic and Tracer Experiments, *Transp. Porous Media*, 42, 85-107, 2001a.
- Silliman, S.E., L. Zheng, and P. Conwell, The use of laboratory experiments for the study of conservative solute transport in heterogeneous porous media, *Hydrogeol. J.*, 6(1), 166-177. 1998.
- Silliman, S.E., R. Dunlap, M. Fletcher, M.A. Schneegurt, Bacterial transport in heterogeneous porous media: observations from laboratory experiments, *Water Resour. Res.*, 37(11), 2699-2707, 2001b.
- Silliman, S.E., and E.S. Simpson, Laboratory evidence of the scale effect in dispersion of solutes in Porous Media, *Water Resour. Res.* 23(8), 1667-1673, 1987.
- Smart, P.L., A Review of the Toxicity of Twelve Fluorescent Dyes Used for Water Tracing, *NSS Bulletin*, 46, 21-33, 1984.
- Smart, P.L., and I.M.S. Laidlaw, An evaluation of some fluorescent dyes used for water tracing. *Water Resour. Res.*, 13(1), 15-33, 1977.
- Tidwell, V.C., and J.G. Robert, Laboratory investigation of matrix imbibition from a flow fracture, *Geophys. Res. Lett.*, 22, 1405-1408, 1995.
- Ursino, N., T. Gimmi, and H. Flühler, Combined effects of heterogeneity, anisotropy, and saturation on steady state flow and transport: a laboratory sand tank experiment, *Water Resour. Res.*, 37(2), 201-208, 2001b.
- Ursino, N., T. Gimmi, and H. Flühler, Dilution of non-reactive tracers in variably saturated sandy structures, *Adv. Water Resour.*, 24, 877-885, 2001a.
- Walker, R.C., C. Hofstee, J.H. Dane, and W.E. Hill, Surfactant enhanced removal of PCE in a partially saturated, stratified porous medium, *Journal of Contaminant Hydrology*, 34, 31-46, 1998.
- Wang, L., A. Roitberg, C. Meuse, and A.K. Gaigalas, Raman and FTIR spectroscopies of Fluorescein in Solutions, *Spectrochimica Acta Part A*, 57, 1781-1791, 2001.

Listed Firms/Institutes

BASF, Ludwigshafen, Germany. www.basf.de

DIS, Netherlands. www.dis-sensors.nl

EAWAG, Dübendorf, Switzerland. www.eawag.ch

Hermes Messtechnik, Germany. www.hermess.de

Merck GmbH, Germany. www.merck.de

Molecular probes. www.probes.com

RS Components, Germany. www.rsonline.de